

accepted by ApJS

# Solar Carbon Monoxide, Thermal Profiling, and the Abundances of C, O, and Their Isotopes

Thomas R. Ayres<sup>1</sup>

*Center for Astrophysics and Space Astronomy,  
University of Colorado, 389 UCB [CASA],  
Boulder, CO 80309-0389; ayres@casa.colorado.edu*

Claude Plymate and Christoph U. Keller

*National Solar Observatory, PO Box 26732,  
Tucson, AZ 85726-6732; plymate@noao.edu, ckeller@noao.edu*

received: 22 August 2005; accepted: 27 March 2006

## ABSTRACT

A solar photospheric “thermal profiling” analysis is presented, exploiting the infrared (2.3–4.6  $\mu\text{m}$ ) rovibrational bands of carbon monoxide (CO) as observed with the McMath-Pierce Fourier transform spectrometer (FTS) at Kitt Peak, and from above the Earth’s atmosphere by the Shuttle-borne ATMOS experiment. Visible continuum intensities and center-limb behavior constrained the temperature profile of the deep photosphere, while CO center-limb behavior defined the thermal structure at higher altitudes. The oxygen abundance was self consistently determined from weak CO absorptions (for C/O  $\equiv$  0.5). Our analysis was meant to complement recent studies based on 3-D convection models which, among other things, have revised the historical solar oxygen (and carbon) abundance downward by a factor of nearly two; although in fact our conclusions do not support such a revision. Based on various considerations, an  $\epsilon_{\text{O}} = 700 \pm 100$  ppm (parts per million relative to hydrogen) is recommended; the large uncertainty reflects the model sensitivity of CO. New solar isotopic ratios also are reported:  $^{12}\text{C}/^{13}\text{C} = 80 \pm 1$ ,  $^{16}\text{O}/^{17}\text{O} = 1700 \pm 220$ , and  $^{16}\text{O}/^{18}\text{O} = 440 \pm 6$ ; all significantly lower than terrestrial. CO synthesis experiments utilizing a stripped down version of the 3-D model—which has large temperature fluctuations in the middle photosphere, possibly inconsistent with CO “movies” from the Infrared

Imaging Spectrometer (IRIS), and a steeper mean temperature gradient than matches visible continuum center-limb measurements—point to a lower oxygen abundance ( $\sim 500$  ppm) and isotopic ratios closer to terrestrial. A low oxygen abundance from CO—and other molecules like OH—thus hinges on the reality of the theoretically predicted mid-photospheric convective properties.

*Subject headings:* Sun: photosphere — Sun: infrared — Sun: abundances

## 1. Introduction

For nearly three decades, the “solar neutrino problem” haunted Solar Physics. The apparent dearth of the elusive subnuclear byproducts of proton–proton cycle fusion presented severe challenges for theoretical descriptions of interior conditions in the Sun; models that heretofore had been regarded as ironclad and unassailable (Bahcall, Basu, & Pinsonneault 2003, and references to previous work therein). The neutrino problem thankfully was resolved in recent years, ironically from the particle-physics rather than astrophysics side (e.g., Bahcall, Krastev, & Smirnov 1999), and solar (and stellar) interior models once again seemed secure.

A new challenge, however, has confronted the even more refined contemporary generation of solar interior models crafted for—and to a large extent by—helioseismology; what one might call the “solar oxygen crisis.” Sophisticated analyses, employing time dependent 3-D simulations of convection driven solar surface velocity fields and thermal inhomogeneities, have pointed to a surprisingly low oxygen abundance, based on an impressive collection of tracers including forbidden and weak permitted O I lines in the visible spectrum, and hydroxyl (OH) rovibrational and pure rotational bands in the 3–10  $\mu\text{m}$  thermal infrared (Asplund et al. 2004, and references to previous work therein).

The new low O abundance ( $\epsilon_{\text{O}} = 460 \pm 50$  parts per million [ppm] relative to hydrogen versus the most recent previously recommended value  $650 \pm 100$  ppm [Grevesse & Sauval 1998, hereafter GS98]: see Figure 1) plays an important role in interior models of the Sun because oxygen ranks third after hydrogen and helium by number in a solar chemical mixture, and contributes very substantially to the interior radiative opacity. Furthermore, the next most abundant species—C, N, and Ne—are very difficult to measure (as is O itself) in the

---

<sup>1</sup>Visiting Astronomer, National Solar Observatory, operated by the Association of Universities for Research in Astronomy, Inc. (AURA), under cooperative agreement with the National Science Foundation.

visible spectrum owing to lack of suitable absorption lines, and changes in their abundances often follow closely any alterations to  $\epsilon_O$ . In other words, abundance ratios such as C/O ( $\sim 0.5$  [Allende Prieto, Lambert, & Asplund 2002]) or Ne/O (derived from solar energetic particles [e.g., Meyer 1985] or high resolution spectra of Ne and O ions in the solar transition zone [Warren 2005]) often are regarded as better determined than the absolute abundances themselves. Thus, a revision in  $\epsilon_O$  could have a domino-like effect on the overall solar chemical composition and heavy element mass fraction  $Z$ , one of the crucial parameters governing the interior structure of a star and its evolution.

The revised low oxygen abundance is said to resolve outstanding issues in interstellar medium and young stellar population studies (Asplund et al. 2004), which previously had pegged the Sun as an “oxygen-rich” dwarf; at odds with its middle-aged status in a galaxy undergoing steady metal enrichment owing to successive generations of stellar birth and death (Timmes, Woosley, & Weaver 1995). At the same time, the solar oxygen crisis has provoked the helioseismology community by casting doubt on the previous spectacularly good agreement between simulated interior sound speed profiles, and the depth of the convection zone, with values deduced from detailed, high precision measurements of surface  $p$ –mode oscillations from the ground and space (Bahcall et al. 2005). Ironically enough, the new oxygen crisis also is having an impact on understanding solar neutrino fluxes (Bahcall & Serenelli 2005).

There appears to be no easy way out of the dilemma from the helioseismology side: the upward revisions in interior opacities needed to accommodate the new low  $\epsilon_O$  are larger than permitted by uncertainties in the best contemporary theoretical and laboratory atomic physics data (Antia & Basu 2005). On the low O side, the latest generation of time dependent 3-D solar convection models have become quite sophisticated, and are said to allow the precise matching of intensity profiles of weak velocity-sensitive photospheric lines without the *ad hoc* specification of extraneous dynamical parameters (such as the micro- or macro-turbulent velocity fields familiar from classical 1-D abundance modeling [e.g., Gray 1976]). This is an extremely important advance in the *ab initio* modeling—and understanding—of the structure of the solar photosphere, and by extension of all late-type stars dominated by strong convective heat fluxes in their surface layers.

Furthermore, the analyses by Asplund and collaborators of the fundamental atomic physics of the various oxygen abundance diagnostics, of blending issues, and of departures from Local Thermodynamic Equilibrium (LTE) in the permitted O I lines are persuasive. In fact, the three major facets of the low O problem—3-D model, atomic physics (including non-LTE effects), and blending—play roughly equal, positively reinforcing roles in explaining the nearly 0.3 dex (factor of  $\sim 2$ ) decrease of the revised oxygen abundance relative to the

value recommended little more than a decade ago (e.g.,  $850 \pm 70$  ppm [Grevesse & Anders 1991, hereafter GA91]). Thus the solar low O problem truly is vexing.

The purpose of the present paper is to add, in our opinion, two key perspectives: (1) the importance of accurately “calibrating” the reference photospheric model, be it 3-D or 1-D, against, say, absolute visible continuum intensities and center-limb behavior; and (2) a complementary oxygen abundance (and thermal profile) diagnostic overlooked in the recent work, namely the rovibrational bands of solar carbon monoxide with its fundamental ( $\Delta v = 1$ ) near  $4.6 \mu\text{m}$  and first overtone ( $\Delta v = 2$ ) near  $2.3 \mu\text{m}$ . The former issue—properly scaling the reference model in temperature—was discussed specifically in a pioneering comprehensive study of the solar carbon, nitrogen, and oxygen abundances by Lambert (1978, hereafter L78), and more generally by Ayres (1977, hereafter A77; 1978a). The solar CO first overtone spectrum, and its significance for the carbon abundance (and thus for  $\epsilon_{\text{O}}$  if C/O is known) was described by Tsuji (1977) and Ayres (1978b), and an extension to the fundamental bands by Ayres & Testerman (1981, hereafter AT81).

To preview our conclusions, the solar CO analysis does not support the recently proposed substantial lowering of the oxygen (and carbon) abundances, but instead favors a higher value for oxygen (and carbon), closer to the recent recommendations of GS98, and the earlier work of L78 and GA91. In addition, we derive new accurate abundance ratios for  $^{13}\text{C}$ ,  $^{17}\text{O}$ , and  $^{18}\text{O}$ . The stable isotopes of C and O are signatures of galactic chemical evolution, and should increase over time as the galaxy becomes progressively enriched in the nuclear detritus of successive generations of star formation. The oxygen isotopes, in particular, can trace fractionation processes in the solar nebula associated with the establishment (or not) of dust-gas equilibrium. It is commonly lamented in the solar system literature, however, that solar astronomy has failed to provide definitive ratios for either  $^{16}\text{O}/^{17}\text{O}$  or  $^{16}\text{O}/^{18}\text{O}$  (Wiens et al. 2004). This was one of the major goals, in fact, of NASA’s ill-fated *Genesis* Discovery mission (Burnett et al. 2003). Nevertheless, we demonstrate that it is straightforward to derive accurate oxygen (and carbon) isotopic abundance ratios from CO lines, and further that the per mil (parts per thousand) differences—e.g.,  $\delta^{18}\text{O}$ —are an order of magnitude, or more, larger than anticipated by theoretical models of the gas-dust chemistry in primitive solar system material.

## 2. Observations

The CO rovibrational spectrum is a valuable tracer for the mid-photospheric thermal profile, and the oxygen abundance, for several reasons. First, the weak lines of the  $\Delta v = 1, 2$  bands form deep in the warmer layers of the photosphere where the CO concentration is

unsaturated, in the sense that  $n_{\text{CO}} \sim \epsilon_{\text{C}} \epsilon_{\text{O}}$ . If one knows the C/O ratio to better accuracy than  $\epsilon_{\text{C}}$  itself, then the CO column density becomes *quadratically sensitive* to  $\epsilon_{\text{O}}$ .

Second, the CO-rich zone nevertheless is shallow enough to lie above the layers where the strongest convective overshooting occurs, in fact where the thermal fluctuation pattern is thought to experience a reversal (e.g., Uitenbroek 2000a), and measured temperature inhomogeneities are mild ( $\Delta T_{\text{rms}} \sim 40$  K: e.g., Ayres & Brault 1990, hereafter AB90).

Third, the  $\Delta v = 1, 2$  bands contain literally thousands of individual transitions covering a wide range of  $gf$ -values and lower level excitation energies, compared with the mere handful of useful O I lines in the visible (L78). Also, potential blends with atomic absorption features are rare in the infrared, particularly in the  $4.6 \mu\text{m}$  interval, contrasted to the heavy atomic line blanketing in the visible. (A key issue in the current low O debate is the strength of a weak Ni I blend in the important [O I]  $0.630 \mu\text{m}$  feature.)

Fourth, the CO  $\Delta v = 1$  bands closely trace the photospheric thermal profile: the strongest lines respond preferentially to the conditions in the higher layers where they become optically thick, whereas the weaker lines reflect conditions at lower altitudes, closer to the infrared continuum formation horizon. Observations of the center-limb behavior of representative CO lines can serve the same “thermal profiling” purpose, in fact redundantly. A subsidiary issue involves the thermal structure of the very high layers, above the nominal base of the warm chromosphere, where the anomalous limb darkening of the strongest CO fundamental lines (Noyes & Hall 1972a, AT81) and their off-limb emissions (Solanki, Livingston, & Ayres 1994) reveal cold gas at altitudes where—in traditional 1-D models like the FAL C of Fontenla, Avrett, & Loeser (1993, hereafter FAL93)—temperatures should be too hot ( $T \sim 7000$  K) for molecules to survive. The origin and spatial scope of this counterintuitive “COmosphere” is controversial (Ayres 2002, and references to previous work therein; hereafter A02), but—as we describe below (§3.3.4)—any high altitude cool material has only a minor influence on deriving an oxygen abundance from the weak  $\Delta v = 1, 2$  lines.

Fifth, the CO rovibrational bands form very close to Local Thermodynamic Equilibrium (LTE), owing to the large atomic hydrogen inelastic collision rates that quench the pure rotation and rotation-vibration transitions compared with their slow radiative decays (see Ayres & Wiedemann 1989, and references to previous work therein, hereafter AW89). LTE formation applies, as well, to the background continuum in the infrared longward of  $1.64 \mu\text{m}$ , where the opacity sources thankfully are simple and well understood: mainly free-free (f–f) transitions of the negative hydrogen ion,  $\text{H}^-$ , with a very small contribution from hydrogen bound-free (b–f) and f–f (Vernazza, Avrett, & Loeser 1976). The CO gas-phase chemistry also is very close to “instantaneous chemical equilibrium” (ICE) in the middle photosphere, even in the face of time dependent molecular formation and destruction, and

advection processes, as demonstrated in recent detailed 2-D hydrodynamical simulations by Wedemeyer-Böhm et al. (2005), and earlier in 1-D time dependent models by Asensio Ramos et al. (2003).

Sixth, the CO molecular parameters including the all important dissociation energy ( $D_0 = 11.108$  eV: Morton & Noreau 1994, hereafter MN94), line positions and transition strengths (Goorvitch 1994, hereafter G94) are thought to be accurately known. Owing to the importance of CO as a terrestrial pollutant, these values have been vetted thoroughly, at least for the lowest  $vJ$  transitions that are prevalent in a cold planetary atmosphere like Earth's.

The final practical advantage of the CO IR bands is the availability of very high quality measurements from the ground and space. The large Fourier transform spectrometer (FTS) on the National Solar Observatory's McMath-Pierce telescope at Kitt Peak (Brault 1978), for example, can record the fundamental region at resolutions of  $R \equiv \omega/\Delta\omega \sim 2 \times 10^5$ , or more, ( $\omega$  is the frequency measured in wavenumbers [ $\text{cm}^{-1}$ ]), fully resolving the narrow solar CO lines, and with signal-to-noise (S/N) in excess of several thousand. The McMath-Pierce also is home to the Infrared Imaging Spectrometer (IRIS), a grating-based instrument with lower resolving power ( $\sim 6 \times 10^4$ ), but a long slit stigmatic imaging capability, and ten times higher time resolution than the FTS can muster (Uitenbroek, Noyes, & Rabin 1994, hereafter UNR94; Ayres & Rabin 1996, hereafter AR96). Furthermore, the Shuttle-borne ATMOS experiment (also an FTS) obtained excellent solar disk center reference spectra in the thermal infrared during its several flights (Farmer 1994), achieving  $2 \times 10^5$  resolution and S/N > 1000 in the best quality scans provided to the community.

Despite the many positive attributes of CO as an abundance diagnostic, a specific downside—shared by molecules in general—is the strong sensitivity of the dissociative equilibrium to temperature. For this reason it is imperative to accurately characterize the thermal conditions in the mid-photosphere where the abundance sensitive weak CO lines arise.

The following sections summarize the several types of observational material used in the subsequent thermal profiling—and oxygen abundance—analysis; including besides 2–6  $\mu\text{m}$  CO, calibrated intensity highpoints in the 0.4–0.7  $\mu\text{m}$  visible continuum region, and continuum center-limb behavior at visible and infrared wavelengths.

## 2.1. ATMOS/ATLAS-3

The Shuttle-borne ATMOS instrument was designed to study trace molecular species in the Earth's atmosphere backlit by the rising or setting Sun as viewed from low-Earth

orbit. The baseline solar reference spectra, obtained from zenith pointings, were mainly free of terrestrial contamination, and consequently are extremely valuable for a study like the present one. The best results were obtained from the final ATMOS flight in 1994 November as part of the ATLAS-3 payload (Abrams et al. 1999). For the particular scan ranges used here, isolated by one of three passband filters, the instrument accepted a 1 mrad-diameter ( $200''$ ) circular region at disk center, which corresponds to  $\mu = 1$  for all intents and purposes ( $\mu \equiv \cos \theta$ , where  $\theta$  is the heliocentric angle:  $0^\circ$  at disk center,  $90^\circ$  at the extreme limb).

Scans were downloaded from the ATMOS public archive and calibrated according to the specifications in the associated documentation. For the CO first overtone interval,  $3200$ – $4800$  cm $^{-1}$ , only scan #4 had suitable coverage. For the CO fundamental region,  $1600$ – $2400$  cm $^{-1}$ , scans #3 and #9 provided overlapping coverage. Each was independently normalized to a continuum level by sequentially fitting low order polynomials to intensity high-points in partially overlapping 5 cm $^{-1}$  intervals: the ATMOS scans are dominated by the ubiquitous—but mainly isolated—absorption features of the CO bands, and generally there are smooth intervals between the lines where the pristine continuum—free of solar or telluric absorptions—shines through. The two separate continuum-normalized scans then were cross-correlated to determine any global frequency offsets. The derived  $\sim 0.5$  pixel shift was applied to scan #9; then the two datasets were combined by *interleaving* the intensity points, rather than interpolating and coadding which would have involved a smoothing of at least one of the scans, perhaps compromising the intrinsic high resolution of the ATMOS spectra. Thus, the tracings presented here for the CO fundamental region consist of two entirely independent datasets: any deviations represent mainly differences in the assigned local continuum levels or scan-specific distortions, and therefore are a fair measure of systematic intensity uncertainties beyond the purely photometric noise component.

Figure 2 illustrates selected intervals of the fundamental and first overtone CO bands from the ATMOS spectra. Figure 3 illustrates selected transitions from the 1–0 R-branch ( $\Delta v \equiv v_{\text{upper}} - v_{\text{lower}} = +1$ ,  $\Delta J \equiv J_{\text{upper}} - J_{\text{lower}} = +1$ ; P-branch transitions have  $\Delta J = -1$ ) of the CO fundamental from ATMOS, together with line profiles calculated with an “optimum” 1-D thermal profile described later (§3.3).

## 2.2. McMath-Pierce FTS

The large (1 m path difference) FTS on the McMath-Pierce telescope achieves superb spectral resolution and excellent signal-to-noise in the thermal infrared, with broad frequency coverage and negligible scattered light. The McMath-Pierce telescope itself, with its 1.58 m primary mirror and all reflecting unobscured design, not only can observe beyond

the  $\sim 2.5 \mu\text{m}$  cutoff of typical window materials used in evacuated solar telescopes, but also delivers sub-arcsecond diffraction limited performance ( $\sim 0''.8$  at  $5 \mu\text{m}$ ) during periods of good seeing.

These capabilities are crucial for center-limb work in the CO bands, where core depths of a wide range of narrow  $\Delta v = 1$  lines must be measured accurately at each  $\mu$  value, and one wants to record as close as a few arcseconds from the limb in order to obtain the best slant-angle advantage for observing the highest atmospheric layers. Errors of only a few percent in line depths, due to under resolving line profiles or the presence of scattered light, can translate to an overestimate of hundreds of degrees in core brightness temperatures (an indirect diagnostic of kinetic temperatures near  $\tau \sim 1$ : AT81).

The main disadvantages of the FTS are that it can record only a single spatial point at a time (defined by an entrance aperture which can have an arbitrary shape and size within certain limits), and it requires several minutes to accumulate a full interferogram at highest resolution and S/N. By its nature, the FTS also benefits from a highly stable source region; a particular concern, for example, in observations very close to the edge of the disk, where seeing fluctuations or wind shake could transiently alter the intensity field. For that reason, the highest quality previous FTS work on the anomalous limb darkening of the CO bands had been done at  $\mu \gtrsim 0.2$  (AT81, AB90), corresponding to  $8.1 \text{ mm}$  or  $19''$  inside the IR limb. (The plate scale of the McMath-Pierce is  $2.37'' \text{ mm}^{-1}$ .)

### 2.2.1. *Fast Tip/Tilt Image Stabilizer*

Recently the FTS was outfitted with a novel fast tip/tilt image stabilization system, developed by C. Keller and C. Plymate of NSO; a major improvement for limb observations. The system mounts on the front plate of the FTS, and delivers a stabilized image to the entrance port of the interferometer. The transfer optics of the stabilizer pick off a portion of the solar image, collimate it onto a piezoelectrically actuated tip/tilt mirror, and refocus the corrected image onto a beamsplitter. The 98% reflected light is directed to the FTS entrance aperture, while the 2% transmitted image is sensed by a CCD camera, which can operate in a variety of tracking modes—limb, quad cell, or granular correlation—to complete the feedback loop. The CCD accepts a  $\sim 100 \text{ \AA}$  passband centered in the red at  $\sim 7000 \text{ \AA}$ . The system operates at 500 Hz, fast enough to compensate for seeing fluctuations and image shake.

### 2.2.2. 2002 April Observing Run

The observations described here were acquired during a 5-day run in 2002 April (13–17), mainly on the 14th. A 98 cm full path difference of the FTS was utilized, and the interferograms were accumulated in double-sided mode. The theoretical resolving power was  $R \sim 2 \times 10^5$  in the  $2145 \text{ cm}^{-1}$  ( $4.66 \mu\text{m}$ ) atmospheric “window” where most CO  $\Delta v = 1$  measurements are made. Each interferogram required nearly four minutes to record, including fly-back. Twin L–N<sub>2</sub>-cooled InSb detectors (“A” and “B”) were sampled at 2500 Hz. (The two outputs view opposite sides of the FTS recombining optic and thus are out of phase with one another. The interferogram signal is the difference of the two, which has the advantage of canceling noise [such as 60 Hz] common to both detectors.) A broad-band filter limited the spectral coverage to  $1800\text{--}2900 \text{ cm}^{-1}$  ( $3.4\text{--}5.6 \mu\text{m}$ ), to suppress out-of-band photometric noise.

On the 14th, we took advantage of superb image quality and lack of (wind-induced) image shake to work close to the limb, exploiting the new image stabilizer. We chose a  $10 \text{ mm} \times 0.25 \text{ mm}$  rectangular entrance aperture ( $24'' \times 0''.6$ ; the radius of the solar image was  $957''$ ). The width of the slit was comparable to the diffraction limit of the telescope, and small enough to impose a negligible  $\delta\mu/\mu$  on observations very close to the limb. The slit was as long as could be accommodated in good focus with the FTS, but short enough that  $\delta\mu/\mu$  due to curvature of the limb was negligible.

We zeroed the coordinate frame of the image stabilizer, in limb tracking mode, at the half power point of the A+B central fringe signal (representing source intensity) as it rolled off across the edge of the disk. Owing to the passband limiting filter, we were measuring the true infrared limb, which can be displaced a few arcseconds from the visible limb by atmospheric refraction. We then backed the limb away from the aperture a set number of steps on the image stabilization system (the plate scale at the CCD was  $0''.14 \text{ pix}^{-1}$ ), to position a specific  $\mu$ -value over the entrance slot. We frequently checked the null position at the IR limb to ensure that no drifts had occurred. During that morning, we obtained 21 separate useful observations at a range of  $\mu$ -values: from  $\mu = 0.169$  (5.83 mm inside the limb) down to as close as  $\mu = 0.076$  (1.17 mm inside the limb). We concluded with a pair of measurements at disk center ( $\mu = 1$ ).

Since the image stabilizer had to be mounted in a fixed orientation on the vertical circular “table” of the FTS, we were not able to actively compensate for the diurnal rotation of the solar image. Accordingly, our observations effectively covered an arc at the limb as the solar disk rotated over the fixed slit position; providing, in fact, a broad, unbiased spatial average at the limb.

A full account of the FTS program will be provided in a future paper, including details of the data reduction, scan averaging, and compensation for atmospheric absorption. Figure 4 compares a disk center tracing from the McMath-Pierce FTS with the ATMOS/ATLAS-3 spectrum described previously. Center-limb lineshapes of selected  $2145\text{ cm}^{-1}$  CO transitions will be presented later (§3.3.3).

### 2.3. McMath-Pierce IRIS

The Infrared Imaging Spectrograph (IRIS), commissioned in 1993, utilizes the Main (“vertical”) spectrograph of the McMath-Pierce, a  $256 \times 256$  Amber Engineering InSb camera cooled by solid nitrogen, and the control system of the Near Infrared Magnetograph (NIM: Rabin 1994). We made use of two general types of IRIS observations in the present study: (1) short exposure single slit measurements of the CO translimb (emission) spectrum; and (2) rapid cadence sequences of raster scans to record 2-D time dependent behavior of the CO bands at disk center.

#### 2.3.1. *Translimb CO Measurements*

Translimb CO measurements are a diagnostic for the coolest parts of the high altitude “COmosphere,” especially the height of the temperature minimum (“ $T_{\min}$ ”). The strong saturated low excitation CO features, in particular, can have significant contributions from this cold ( $T < 4000$  K) region, thereby affecting the determination of the temperature stratification and potentially also the oxygen abundance.

The present study utilized sequences of translimb image bursts obtained 1996 May 9, representative of the quiet Sun near sunspot minimum, as described fully by A02. Although not stated explicitly in that study in these terms, the single component thermal profile that best matches the off-limb CO emissions has a  $T_{\min}$  at a column mass density  $m \sim 2.5 \times 10^{-3}$  gr  $\text{cm}^{-2}$ , compared with the  $m \sim 5 \times 10^{-2}$  of the FALC reference model (FAL93). Unfortunately, the off-limb CO emissions—as recorded by the relatively low dispersion IRIS instrument—are not useful for quantifying  $T_{\min}$  itself. However, the new FTS extreme limb scans can be used for that purpose, as described later (§3.3.4). (To preview our results, we obtain  $T_{\min} \sim 3500$  K, as compared with the 4400 K of the FALC model.)

### 2.3.2. Disk-Center CO Timeseries

The second set of IRIS data comprised high spatial resolution, rapid cadence surface temperature maps recorded during a coordinated multiwavelength campaign in 1999 May. The program, which included simultaneous UV imaging spectroscopy from *SoHO* SUMER and narrow band UV imaging from *TRACE*, has been described previously in a qualitative way by Ayres (2000). Here, we provide additional details concerning the IRIS part of the program.

The objective on the IRIS side was to measure, with high time resolution, temperature and velocity fluctuations at several levels of the outer photosphere, ultimately to compare with the response of the overlying chromosphere imaged by SUMER and *TRACE*. In the present work, however, the amplitude of thermal fluctuations in the mid- and high photosphere play a direct and crucial role in backing out realistic abundances from temporally and spatially averaged solar CO measurements.

The IRIS spectra described here were obtained on the morning of 1999 May 14. The visible seeing was good at the start of observations (08:30 MST), but deteriorated later in the morning. The infrared seeing usually is much better than in the visible, and the effective resolution often is limited by telescope diffraction rather than the atmosphere.

We operated the vertical spectrograph in single pass, recording a free spectral range of  $2.3 \text{ cm}^{-1}$  centered at  $2143 \text{ cm}^{-1}$ ; with a “minifying” lens in the transfer optics to achieve a spatial coverage of  $97''$  along the slit. The slit was oriented N/S heliocentric, with a width of  $160 \mu\text{m}$  ( $0''.4$ ). In mapping mode, the slit was stepped sequentially in the E/W direction, 8 steps per raster with a step spacing of  $1''.9$ ; thus covering a swath  $13'' \times 97''$  at Sun center. The exposure time at each slit position was 300 ms, and with stepping and data writing overheads, a full area scan required 45 s to complete (well sampling the photospheric *p*-mode oscillations timescale [5 minutes] and that associated with higher frequency chromospheric modes [3 minutes]). We accumulated 40 rasters per observation: 320 spectral frames in 30 minutes.

In each individual spectrogram, the main parameters of interest were central depths and frequency shifts of the CO lines, and the relative variation of continuum intensity, as recorded along the 1-D slit direction. (Reduction and measurement techniques are described by AR96). The depth of a strong saturated CO line is tied closely to the kinetic temperature of the atmospheric layer in which the line core becomes optically thick. Similarly, the Doppler shift records the line-of-sight component of the velocity field where the feature forms. Finally, the relative continuum intensity responds to temperature contrasts in the layers where the IR background continuum becomes optically thick. In general, the line FWHM also would be a

parameter of interest, reflecting possible changes in the unresolved velocity field. Empirically, however, we found very little spatial variation in the fitted FWHMs.

Assembling the 1-D measurements for the 8 pointings in each area scan yielded a 2-D spatial map for that 45 s time interval: velocity and intensity fluctuations for the CO lines (which were coadded into two sets: “strong” [2–0 R6, 3–2 R14, 4–3 R23] and “weak” [7–6 R67, 7–6 R68]), and intensity for the background continuum. The  $\Delta I$  fluctuations were translated to equivalent  $\Delta T$  according to a disk center absolute continuum intensity obtained from a model calculation. An example of a 10 frame sequence is shown in Figure 5. Figure 6 illustrates cross-correlations of several combinations of line and continuum parameters, imposing discrete temporal lags out to  $\pm 5$  steps, in multiples of the fundamental 45 s cadence, over one of the 40 frame sequences. In the full interval (450 s), solar rotation would carry the scene about 1" under the fixed area scan, comparable to the diffraction-limited spatial resolution.

In the bottom row, one sees that the continuum thermal fluctuations maintain a noticeable self correlation (tilted contours) over the full range of lags displayed ( $\sim \pm 4$  minutes). This likely is a signature of photospheric convective granulation, which has a coherence time of order 10 minutes. Notice, also, that the temperature fluctuations are relatively mild: the rms value is only about 22 K. In contrast, while the weak CO lines show a modest positive correlation with the continuum at zero lag, the correlation rapidly dissipates for lags on either side of zero. At zero (or any other) lag, the weak CO lines (with a larger  $\Delta T_{\text{rms}} \sim 42$  K) show no evidence for a *negative* branch of the continuum correlation, as might have been anticipated as a signature of “reversed granulation” reported previously in the strong CO 3–2 R14 line from an IRIS CO time series utilizing a fixed slit (Uitenbroek 2000a), and in simulations of weak 7–6 R68 with a 3-D model in the same work.

Here, the strong CO lines also show hardly any correlation with the continuum, even at zero lag; and a larger range of  $\Delta T$ , although the rms still is a relatively modest 83 K. Thus, the thermal variations at high altitudes probed by the strong CO lines appear to be unconnected to the inhomogeneities of the middle photosphere recorded in the IR continuum. This point is emphasized in Fig. 5 where the patches of highest and lowest  $\Delta T$  are highlighted by contours in the strong-line and continuum maps, and repeated in the other panels. Few of the peak temperature excursions in the continuum print through to the outer photosphere. In fact, the granular contrast in the thermal IR continuum is very low, probably as a consequence of formation in the higher altitude zone where the granulation pattern is reversing and is more chaotic than in deeper layers. That would account for the apparent lack of anti-correlation with the strong CO lines, but also suggests that the convective penetration in these layers is more muted than predicted by the 3-D simulations.

The important role of  $p$ -mode oscillations in driving temperature fluctuations in the strong CO  $\Delta v = 1$  lines was recognized at the time these features first were observed with high resolution and sensitivity at the McMath-Pierce in the early 1970’s (Noyes & Hall 1972b). Independently of how temperature (and velocity) perturbations in the CO and continuum layers might be connected (or not), the high spatial resolution IRIS maps provide a direct probe of these excursions in the altitude range most relevant to the CO absorptions. This information can be exploited to test the response of simulated spectra to the fluctuating environment of the middle and upper photosphere.

## 2.4. Absolute Continuum Intensities and Center-Limb Behavior

The final piece of the observational puzzle, to set the stage for the thermal profile (and abundance) analysis, are measurements of continuum highpoints in the visible spectrum, and continuum center-limb behavior from the visible out to the 5  $\mu\text{m}$  CO  $\Delta v = 1$  region. Continuum highpoints provide a fundamental calibration of the temperature scale of a solar model in its deepest layers, while the center-limb behavior responds primarily to temperature *gradients* over the emission formation zone,  $\tau_C \sim 0.1\text{--}1$ . Since the IR continua beyond 3  $\mu\text{m}$  form *above* the visible continuum, their center-limb behavior can be exploited to transfer the visible-based temperature calibration to the even higher layers where the CO lines arise.

### 2.4.1. Visible and Infrared Center-limb Behavior

We used two sources for continuum center-limb behavior: Neckel & Labs (1994, hereafter NL94) for  $\lambda < 1.1 \mu\text{m}$ , and Spickler, Benner, & Russell (1996, hereafter SBR96) for  $\lambda > 2.4 \mu\text{m}$ . The NL94 measurements were based on monochromatic ( $\sim 2 \times 10^5$  resolution) drift scans obtained with the McMath-Pierce telescope and vertical spectrograph, regularly during the period between solar minimum in 1986 and maximum in 1990. These data agree well with previously published work by Pierce and colleagues (Pierce & Slaughter 1977; Pierce, Slaughter, & Weinberger 1977), typically better than  $\pm 0.5\%$  according to our own comparisons. In the thermal infrared, SBR96 reported center-limb curves recorded by the HALOE occultation experiment on the Upper Atmosphere Research Satellite, at eight wavelengths between 2.45  $\mu\text{m}$  and 9.85  $\mu\text{m}$ , with bandwidths corresponding to a resolution of  $\sim 50$ . We considered only the six measurements  $\leq 6.25 \mu\text{m}$ , approximately the upper wavelength limit of the CO  $\Delta v = 1$  bands. The visible and IR center-limb curves will appear later (§3.3.1), when we compare the empirical behavior with predictions of different thermal models.

#### 2.4.2. Absolute Continuum Intensities

We adopted the Thuillier et al. (2004, hereafter T04) solar irradiance reference spectra as a basis for calibrating absolute disk center intensity highpoints. These spectra cover the wavelength range from kilovolt soft X-rays to the 2.4  $\mu\text{m}$  mid-IR, although we made use only of the visible portion, 0.4–0.7  $\mu\text{m}$ . The reference spectra were derived from a variety of sources, for two levels of solar activity. (The irradiance differences between sunspot minimum and maximum are entirely negligible in the visible, however). The mid-UV/visible portion (0.20–0.87  $\mu\text{m}$ ) was recorded at a resolution of  $\sim 10 \text{ \AA}$  by the SOLSPEC instrument on the three flights of the Shuttle ATLAS platform, mentioned previously in the context of the ATMOS experiment. Integrations of the reference spectra yielded a total solar irradiance (TSI) within 1% of TSI values measured independently by active cavity radiometer (“ACRIM”) instruments in the same epoch. A detailed error estimate (see Thuillier et al. [2003], their Table IIIa–d) indicated a  $1\sigma$  uncertainty of  $\pm 1\%$  for the 0.45–0.70  $\mu\text{m}$  range of interest here. T04 further normalized their reference spectrum to the estimated TSI of 1367  $\text{W m}^{-2}$  at 1 AU during that epoch, to improve the absolute accuracy to approximately that of the TSI measurements ( $\lesssim 1\%$ ).

The reference spectra are disk average irradiances  $f_\lambda$  at 1 AU, at the coarse resolution of 10  $\text{\AA}$ . For modeling purposes, it is desirable to extract specific intensity  $I_\lambda$  highpoints in the visible that are as close as possible to the pristine continuum level at disk center. We accomplished this as follows.

R. L. Kurucz kindly provided a high resolution irradiance atlas of the solar spectrum based on groundbased FTS scans corrected very carefully for telluric absorptions, instrumental filter response, and so forth. These spectra had been normalized to a continuum level determined by identifying narrow windows where detailed spectral simulations indicated minimal solar (and telluric) line absorption, and adjusting for such structure if necessary. We smoothed these high resolution continuum normalized tracings to the  $\sim 10 \text{ \AA}$  bins of the T04 reference spectrum. We next multiplied the reference irradiance spectrum by  $(d_\odot/R_\odot)^2$  to scale it to surface flux, then divided by the smoothed continuum normalized trace. We identified regions of the ratio that corresponded to  $> 98\%$  highpoints in the smoothed high resolution spectrum (in the interval 0.40–0.69  $\mu\text{m}$ ) and fitted a fifth-order polynomial to those points, with one pass of a  $2\sigma$  filter to suppress outliers. Because information concerning the high resolution continuum level was encoded in the original residual flux spectrum “100% level,” the resulting polynomial curve should correspond very well to the hypothetical pristine continuum (in flux). The final step was to divide the highpoint surface flux curve by the wavelength-dependent  $\mathcal{F}_\lambda/I_\lambda$  (as taken from NL94 and fitted by a fourth-order polynomial). These steps are illustrated in Figure 7.

Although the slight  $\sim 1\%$  downward adjustment by T04 of their reference spectrum to match TSI values should yield an improved absolute accuracy, a more recent TSI experiment, SORCE/TIM (Kopp et al. 2005), which utilizes a somewhat different sensor technology than the earlier ACRIM-style devices, shows a systematic  $5 \text{ W m}^{-2}$  ( $0.4\%$ ) lower TSI than contemporary ACRIM measurements over the same time period. The origin of the difference is unknown, but it is comparable to systematic offsets seen in comparisons of individual ACRIM instruments (Willson 2005). The cited absolute accuracy of the SORCE/TIM instrument is  $0.01\%$ . We therefore further adjusted the derived continuum highpoints downward by  $0.4\%$  to the SORCE/TIM scale. Table 1 lists representative line-free continuum central intensity highpoints for the range  $0.45\text{--}0.70 \mu\text{m}$  from the polynomial model.

Incidentally, the solar luminosity that results from this exercise is  $L_\odot = 3.830 \times 10^{33} \text{ ergs s}^{-1}$ , and the effective temperature is  $(T_{\text{eff}})_\odot = 5772 \text{ K}$ . Asplund et al. (2000b) adopted  $(T_{\text{eff}})_\odot = 5767 \text{ K}$  for their convective heat flux calculations, which corresponds to a (entirely negligible) third of a percent lower surface flux.

We compared the new calibrated continuum intensity highpoints to those derived two decades ago by Neckel & Labs (1984, hereafter NL84), who applied an analogous approach with the best available measurements of the time. Over the  $0.46\text{--}0.65 \mu\text{m}$  range that we adopted to define the visible continuum, our results for the 7 wavelengths in that interval reported by NL84 (their Table VII) are on average  $+0.9\pm1.7\%$  higher; while for the interval between  $0.4975\text{--}0.6200 \mu\text{m}$ , where the continuum potentially is less affected by line blanketing, our results are  $+0.1\pm0.8\%$  higher (where the uncertainties are  $1\sigma$  dispersions about the mean values). The extent to which this remarkably good agreement is accidental cannot be known, but we regard it as evidence that the new continuum highpoints do not suffer unrecognized systematic errors beyond the  $\sim \pm 1\%$  level.

#### 2.4.3. Continuum Intensity Fluctuations

Finally, we considered the additional information available from visible and near-infrared continuum intensity fluctuations reported in several recent studies. Such “granular contrast” measurements play a key role in validating the amplitude of thermal fluctuations in *ab initio* convection simulations, and in estimating the  $\Delta T$ ’s that one might impose on a purely empirical model to capture the range of thermal inhomogeneities present at different levels of the solar photosphere.

For example, Leenaarts & Wedemeyer-Böhm (2005) utilized the Dutch Open Telescope to obtain high resolution movies simultaneously in the blue continuum ( $0.432 \mu\text{m}$ ) and the

wing of the Ca II H line ( $0.397\text{ }\mu\text{m}$ ). The latter forms in the mid- to high photosphere and displays a “reversed granulation” signature like the strong CO fundamental lines (Uitenbroek 2000a). In their  $I/\langle I \rangle$  histograms, the blue continuum shows a roughly 25 % fluctuation amplitude at half maximum occurrence (corresponding to an rms of about 20 % for a Gaussian distribution), while the H-line wing displays about a 10 % amplitude, with reversed contrast (corresponding to  $\Delta T_{\text{rms}} \sim 50\text{ K}$ ).

Puschmann et al. (2003) obtained a 50 minute time series of long slit spectrograms at the German Vacuum Tower Telescope on Tenerife, and examined the behavior of several  $0.65\text{ }\mu\text{m}$  Fe I lines with respect to the red continuum. The latter displayed rms fluctuations in the neighborhood of 4 %. The authors concluded that only relatively large structures ( $\gtrsim 2''$ ) of the deep convective pattern print through to the upper photosphere, and exhibit a reversed intensity contrast. They estimated the reversal height to be about 140 km ( $m \sim 1.5\text{ gr cm}^{-2}$  in the FAL C model).

Sánchez Cuberes et al. (2003) described center-limb observations at  $0.80\text{ }\mu\text{m}$  and  $1.55\text{ }\mu\text{m}$ —continuum opacity maximum and minimum, respectively—recorded at the Swedish Vacuum Solar Telescope (SVST) on La Palma. They reported rms granulation contrasts of 6 % at  $0.80\text{ }\mu\text{m}$ , and 3 % at  $1.55\text{ }\mu\text{m}$ , with decreasing contrasts at both wavelengths toward the limb. Frame selection ensured sharp images, although there was no explicit correction for atmospheric degradation. The authors estimated a convection penetration height of  $\sim 220\text{ km}$ , from the presence of distinct granulation signatures out to the extreme limb. An earlier study by Sánchez Cuberes et al. (2000) measured the center-limb behavior of continuum intensity fluctuations at  $0.67\text{ }\mu\text{m}$  with the SVST during a partial eclipse, exploiting the lunar limb to calibrate the image blur by telescope and atmosphere. They found a disk center rms granular contrast at  $0.67\text{ }\mu\text{m}$  of 10 %, which translates to about 13 % at  $0.5\text{ }\mu\text{m}$ , at the upper end of previously published values, but perhaps not unreasonable given the accurate corrections enabled by the circumstance of the partial eclipse and the excellent observing conditions.

These granular contrasts in the visible are entirely consistent with the predictions of the Asplund convection model at  $0.62\text{ }\mu\text{m}$ , namely  $\sim 15\text{ %}$  from the full-resolution simulation and  $\sim 10\text{ %}$  when smearing by telescope diffraction and seeing are taken into account (Asplund et al. 2000a).

### 3. Atmospheric Modeling

We carried out two general types of atmospheric modeling to constrain the photospheric thermal profile, at least from the special perspective of carbon monoxide. The first type involved simulations of the line-free continuum, in the visible and infrared, and its center-limb behavior. The second type involved synthesis of CO absorption lineshapes, and their center-limb behavior, to test thermal models (strong, saturated lines) and derive self-consistent abundances (weak, unsaturated transitions).

Within each class of simulation, we considered a range of single component models; as well as multicomponent variations to mimic the thermally heterogeneous solar plasma (so-called “1.5-D” approximation in which temperature inhomogeneities are simulated by combining spectra synthesized from a series of 1-D perturbed versions of the base stratification). We treated any specific model in hydrostatic equilibrium, although we did allow for “turbulent pressure” support as described by Vernazza, Avrett, & Loeser (1973, hereafter VAL73). We adopted an anisotropic radial-tangential model of the auxiliary turbulence parameter used in the Doppler width (and turbulent pressure) calculations, simplified by assuming a depth independent velocity separately for the radial and tangential lines of sight. We adopted  $\mu = 1$  microturbulent velocities from other work, as described below (§3.3.1), and adjusted a macroturbulent parameter to achieve a satisfactory fit to the fully resolved empirical CO profiles. We used the same macroturbulence for the limb sightlines, and adjusted the tangential microturbulent parameter to achieve a good match between synthesized and empirical limb lineshapes. The exact choice of these dynamical broadening parameters, within the broad limits set by previous studies, has only a very minor impact on deriving  $\epsilon_0$ , primarily because the selected abundance reference lines are weak and unsaturated.

We calculated the equation of state allowing for LTE formation of  $\text{H}_2$  (Auer, Heasley, & Milkey 1973, hereafter AHM73),  $\text{H}^-$  (VAL73),  $\text{H}_2^+$  (AHM73), LTE ionization of the metals, a simple non-LTE Balmer-continuum photoionization approximation for hydrogen ionization (Linsky 1968) as “calibrated” against the actual electron densities of the FALC reference model, and instantaneous chemical equilibrium for the important diatomic molecules composed of H, C, N, O, and Si (Kurucz 1985, with the exception of the dissociation energy of CO, as described later [§3.2]). Temperature dependent atomic partition functions were polynomial fits to the data in Table D2 of Gray (1976). We adopted the “standard solar composition” of GS98, to maintain consistency with the Asplund model (see Asplund et al. 2000b), particularly with regard to the electron donors which affect the crucial  $\text{H}^-$  concentration.

Each model was represented by the run of temperature,  $T$  (K), with the logarithm of the column mass density,  $\log m$  ( $\text{gr cm}^{-2}$ ), on a scale from  $-4.50$  to  $+0.86$  with a spacing

of 0.02 dex. The radiation transport was simulated using Auer’s (1976) Hermitian method implemented in a Feautrier-type ray solution, which has high accuracy especially with the finely spaced depth grids used here.

### 3.1. Background Opacities

We adopted the  $\text{H}^-$  b–f and f–f opacities recommended by John (1988). The absolute, and relative, accuracies of the underlying cross sections are quoted as better than a few percent.  $\text{H}^-$  b–f completely dominates the visible spectrum shortward of the photoionization edge at  $1.642 \mu\text{m}$ , while the f–f opacity dominates out in the CO  $\Delta v = 1, 2$  portion of the infrared (Vernazza, Avrett, & Loeser 1981, hereafter VAL81). Since our models are “calibrated” against visible absolute intensities and center-limb behavior, as described below (§3.3.1), it is important that the b–f and f–f opacities enjoy high relative accuracy, to ensure an effective transfer of the visible temperature calibration to the infrared.

We also included the metal opacities of Peach (1970) for Mg, Si, and Al; hydrogen b–f according to the Gaunt factors of Carbon & Gingerich (1969), assuming LTE populations for the  $n \geq 3$  levels that contribute to the visible and IR opacity; hydrogen f–f according to the Gaunt factors of AHM73; Thomson scattering by free electrons and Rayleigh scattering by neutral hydrogen; and  $\text{H}_2^+$  f–f from Kurucz (1970). These all are minor contributors at the wavelengths of interest for the present work.

We assumed LTE formation of the continuous opacity sources and the CO  $\Delta v = 1, 2$  bands. This is a good approximation for the collisionally controlled  $\text{H}^-$  populations, and the  $\text{H}^-$  f–f absorption process, in the deep photosphere where the visible and infrared continua form; as well as for the CO bands themselves (AW89). Small departures from LTE, and potentially large departures from instantaneous chemical equilibrium, can affect the CO lines at high altitudes (Uitenbroek 2000b; Asensio Ramos et al. 2003; Wedemeyer-Böhm et al. 2005), but these are less relevant for the present study.

### 3.2. Molecular Parameters

We adopted the CO formation parameters of Kurucz (1985), except for the dissociation energy of  $^{12}\text{C}^{16}\text{O}$  which we took from MN94,  $D_0 = 11.108 \pm 0.002 \text{ eV}$ . The dissociation energies for the isotopic variants of CO typically are 0.002 eV higher. The  $D_0$  in the Kurucz compilation was slightly lower (by 0.017 eV), but we prefer the more recent Morton & Noreau value. The small difference in any event is inconsequential, and we consider the dissociation

energy to be very well determined.

We adopted the excitation energies, oscillator strengths, and partition functions tabulated by G94 for  $^{12}\text{C}^{16}\text{O}$ , and the isotopomers  $^{13}\text{C}^{16}\text{O}$ ,  $^{12}\text{C}^{17}\text{O}$ , and  $^{12}\text{C}^{18}\text{O}$ ; based on experimentally determined electric dipole moment functions (EDMFs). The excitation energies are extremely well determined through direct spectral measurements, but the line strengths are less certain (especially at high  $vJ$ : see, e.g., Chackerian et al. 1994), and potentially are a major source of systematic error in an abundance analysis. We therefore also considered oscillator strengths derived from the dipole matrix elements of Hure & Roueff (1996, hereafter HR96), based on *ab initio* EDMFs; and the earlier pioneering study by Kirby-Docken & Liu (1978, hereafter KL78). Figure 8 compares these two oscillator strength scales to the adopted G94.

The HR96  $gf$ -values are systematically  $\sim 3\%$  higher than G94 for the  $\Delta v = 1$  bands; and up to 5 % lower for  $\Delta v = 2$  transitions, with a noticeable trend with lower level excitation energy amounting to 2 % per  $10^4 \text{ cm}^{-1}$  interval in  $E_{\text{lower}}$ . The earlier KL78 values are lower than G94 by up to 20 %, and show larger scatter than H96. We consider the differences between the independent G94 and HR96 scales to be a reasonable assessment of the accuracy of the CO line strengths.

That said, one potential area of concern is that the  $\Delta v = 1$  abundance diagnostic lines are mainly from high initial  $vJ$  states: the lower lying vibrational and rotational levels are heavily populated, and their usually saturated line transitions mostly are useless as abundance tracers. On the other hand, the  $\Delta v = 2$  transitions have oscillator strengths typically two orders of magnitude smaller than the fundamental lines from the same  $vJ$  initial state. Thus, the first overtone abundance lines tend to be from low  $vJ$  initial states corresponding to peak populations of the rovibrational levels. If there are any systematic errors in the oscillator strength scales that depend, say, on  $vJ$ , our comparisons of  $\Delta v = 1$  and  $\Delta v = 2$  abundances could be skewed, and thermal profiling based on the stronger saturated  $\Delta v = 1$  lines could be affected as well. We therefore took special care to select abundance diagnostic lines covering as wide a range of lower level excitation energies as feasible for both the  $\Delta v = 1$  and 2 band systems.

As for the isotopic transitions, their oscillator strengths are essentially identical to those of the parent lines, thus uncertainties in the  $gf$ -value scale effectively cancel in the abundance ratio, say  $^{16}\text{O}/^{18}\text{O}$ . In principle, then, it should be possible to derive isotopic ratios more accurately than  $\epsilon_0$  itself.

### 3.3. Thermal Profiling

The CO infrared absorption spectrum is highly temperature sensitive thanks to the diatomic molecular formation. CO is more robust than other diatoms owing to its high dissociation energy. This allows CO to persist over a wider range of temperatures than any other molecule, extending even down into the relatively warm photospheric layers where  $T \gtrsim 5000$  K. Thus CO can serve a thermal tracer over an appreciable, important range of the middle photosphere. Nevertheless, we must appeal to visible continuum intensities, and visible and infrared center-limb behavior, to constrain the thermal profile in the deepest molecule-free layers.

Despite some amount of standardization in opacities and equations of state—thanks to historical codes from major modeling groups, such as at Harvard and Uppsala, which have been adapted by others and modified over the years—even small differences in cross sections, electron donor abundances, or the level of sophistication in the equation of state is sufficient to render inaccurate one group’s calculations of, say, continuum intensities using another group’s thermal model. One can minimize this “model construction bias” by beginning with the other group’s  $T(\tau_{0.5\mu\text{m}})$  relation, if available, and decomposing it using ones own opacities, abundances, equation of state, and so forth; but even so, small difficult to recognize systematic differences might persist.

We worked around the bias by utilizing the absolute visible continuum intensities not simply to test the accuracy of different models (L78), but rather as a calibration which we force all model distributions to obey (A77). This ensures that the model temperatures in the deep photosphere, where the visible continuum forms, are accurately slaved to the calibrated empirical intensities, allowing us to compare different models on as fair a basis as possible. Then, the continuum center-limb behavior provides an independent test of the adjusted models, specifically their temperature gradients shallower than  $\tau_{0.5\mu\text{m}} \sim 1$ . A model scaled to match the visible absolute intensities, and which reproduces the continuum center-limb behavior from  $0.5\mu\text{m}$  out to the limit of the CO  $\Delta v = 1$  bands at  $\sim 6\mu\text{m}$ , should have the “correct” temperature distribution in the vicinity of the CO forming layers, which is a necessary condition to ensure accurate abundance determinations from the molecular absorption spectra.

#### 3.3.1. Photospheric Models: Matching Absolute Continuum Intensities

*and Center-limb Behavior*

Figure 9 compares three photospheric thermal profiles evaluated in the present study: FALC; the mean model of Asplund et al. (2004), but including their rms temperature perturbations; and a modified version of the Asplund model adjusted slightly in its deeper layers to better match the continuum center-limb behavior, and in its outer layers for CO center-limb behavior and the off-limb CO emissions (for historical reasons, we call this model “COmosphere” [see, e.g., A02]).

We caution that because the Asplund mean model was constructed by averaging the dynamic 3-D simulation over surfaces of constant radial  $0.5 \mu\text{m}$  continuum optical depth, it not necessarily is the same mean  $T(m)$  stratification that would be obtained by a similar averaging at a very different wavelength, say  $5 \mu\text{m}$ ; or for that matter if the averaging were done along slanted rays, as for limb viewing angles. To the extent that 3-D effects are important, the conclusions we draw below based on the 1-D Asplund mean model (or 1.5-D variants) might not be applicable to a proper treatment of the multidimensional radiation transport in the full 3-D time dependent structure. In a general sense, the 3-D effects should be less important for disk center spectral modeling (from which we derive abundances and isotopic ratios), but more significant for center-limb behavior (which we exploit as a discriminator among the various model stratifications). We have adopted the 1.5-D approach here to allow a more detailed treatment of the various model and parameter sensitivities of the CO and continuum formation than would be possible with a full 3-D model. This approach allows us to fairly incorporate results based on previous 1-D semiempirical models (which still might have future value for analyses of unresolved stars), and points toward additional tests that could be applied to validate the full 3-D simulations (which—although highly sophisticated in their present incarnations—after all still are only an approximate representation of the complexity of the real photosphere of the Sun).

Figures 10a and 10b display absolute continuum intensities and center-limb behavior predicted by the FALC and Asplund mean model, relative to the measured values described in §2.4. The mass scales of both models were adjusted slightly (typically a few percent) to force agreement with the absolute continuum intensities, the fundamental model calibration discussed earlier. Although the Asplund mean model accurately reproduces the center-limb behavior of  $5 \mu\text{m}$  continuum intensities, it does relatively poorly in the visible and near IR, compared with the FALC. We also depict the center-limb behavior in terms of brightness temperatures, to remove the Planck function bias inherent in intensity comparisons across large stretches of the spectrum (i.e., a  $\Delta I$  of 1% represents a much larger temperature difference in the mid-IR than in the blue). The comparison indicates that the mean temperature profile of the Asplund model has too steep a gradient in the visible continuum forming layers

( $\tau_{0.5\mu\text{m}} \sim 1$ ) compared with the reference model, which can be seen clearly in Fig. 9, as well. The too steep predicted center-limb curves in the visible imply that the deep photosphere temperature “calibration” will not be carried reliably out to the higher layers in which the CO infrared bands form.

Figure 10c depicts the same continuum comparison for the Asplund mean model, but now including multicomponent effects in the schematic 1.5-D way by combining intensities synthesized with a 5 component model. The central profile is the mean model  $T_{\text{mean}}(m)$ , the outer temperature profiles are  $T_{\text{mean}} \pm \sqrt{2} \times \Delta T_{\text{rms}}$  (as given by Asplund et al. 2004), and the inner profiles are  $T_{\text{mean}} \pm \frac{\sqrt{2}}{2} \times \Delta T_{\text{rms}}$ . The components were evenly weighted to approximate a Gaussian distribution. Predictions for the individual profiles are depicted as thin curves, while the weighted averages are represented by heavier dashed curves. Here, again, the underlying mean model was adjusted slightly in  $m$ , with the indicated  $\Delta T$  perturbations, to force the average intensity to match the reference continuum highpoints. (Accordingly, the scaling is slightly different for the mean model by itself [Fig. 10b], versus the 5 component version [Fig. 10c].) Note that while the range of intensity fluctuations for the individual components in the visible is substantial ( $\sim 20\%$ ), the center-limb behavior remains close to that of the single component model.

The 1.5-D approach, of course, neglects the geometrical interaction along the same highly slanted sightline of, say, the narrow dark subduction lanes and the more puffed up, bright upwelling cells of the 3-D time dependent simulation. This effect is very important for understanding the center-limb behavior of G-band bright points, for example, which are very fine scale partially evacuated magnetic structures found principally in the dark lanes of the granulation pattern (Carlsson et al. 2004). However, for the normal photospheric granulation pattern, which consists of much larger structures, the geometrical interactions should be less important. Furthermore, the empirical measurements of thermal fluctuations in the  $5\mu\text{m}$  continuum and weak CO lines—which at disk center bracket the altitude range where the visible continuum arises at the extreme limb—suggest that the 3-D model might exaggerate the thermal contrasts in those layers, leading to even less of a sightline interaction effect in the real Sun. (This conclusion rests, however, on the assumption that the empirical measurements of intensity fluctuations fully resolve the thermal inhomogeneities in the middle photosphere. If the true structures are very fine in spatial scale, blurring by the telescope and atmosphere will reduce the contrast. This is particularly important in the thermal IR where diffraction limits the resolution to barely subarcsecond.)

### 3.3.2. Adjusted Thermal Structures and Model Sensitivities

Although the scaled FALC temperature profile in the deep photosphere reproduces the continuum absolute intensities and center-limb behavior well, it has a warm chromospheric temperature inversion at intermediate altitudes ( $\sim 500$  km above  $\tau_{0.5\mu\text{m}} = 1$ ), which is incompatible with the center-limb behavior of strong CO  $\Delta v = 1$  lines and their off-limb emissions (e.g., A02). The Asplund mean model, as well, fails to reproduce the CO center-limb behavior [in part because their  $T(m)$  cuts off in the upper photosphere, and had to be extended isothermally beyond the outermost point in their tabulation].

We therefore crafted the COmosphere model by first adjusting the scaled Asplund stratification in the deeper layers to match the continuum center-limb curves, while continuing to force a fit to the absolute intensities. The resulting deep photospheric temperature profile is nearly identical to that of the FALC, and essentially indistinguishable in terms of continuum center-limb behavior in the visible and near IR. We further spliced in a high altitude  $T_{\min}$  (and temperature rise), such as illustrated in Figure 3 of A02 (“Cool0” model), and altered the mid-photospheric profile to match CO  $\Delta v = 1$  center-limb behavior (as illustrated below [§3.3.4]).

Finally, like the 5 component stripped down version of the Asplund model, we introduced equally weighted temperature perturbations around the mean COmosphere  $T(m)$  profile. In order to match the  $\sim 10\%$  rms granular contrast at  $0.60\mu\text{m}$ , we retained the Asplund et al.  $\Delta T_{\text{rms}}$  in the deep photosphere ( $m \gtrsim 3\text{ gr cm}^{-2}$ ), but imposed smaller  $\Delta T$ ’s in the higher layers based on the empirical behavior of strong and weak CO lines and the  $5\mu\text{m}$  continuum described in §2.3.2.

We further added a “hot” component identical to the FALC in the deep photosphere, but 200 K warmer above about  $m = 1\text{ gr cm}^{-2}$ . This component was intended to mimic the influence of supergranulation network elements, and was assigned a weight of 10% (such bright, warm patches are seen in large-area CO maps, but have small filling factors: AR96). Since the ATMOS spectra were accumulated over a substantial field of view at Sun center, it seemed prudent to incorporate at least some contribution from the warm network elements that must have been captured. As with the multicomponent version of the Asplund model, we found that the average continuum center-limb behavior of the 6 component COmosphere model was not appreciably different from that of the single component version by itself (not illustrated). Physical properties of the 6 component COmosphere model are summarized in Table 2 (“ $T_{\text{NW}}$ ” is the temperature profile of the hot network component).

### 3.3.3. Initial Abundance Tests

In this section, we describe our initial efforts to derive self-consistent C and O abundances from the reference models, as a prelude to several tests of the model sensitivities (varying such parameters as the microturbulent velocity, mid-photosphere temperature profile,  $T_{\min}$  value, and so forth). First, however, we depict in Figure 11 the center-limb behavior and contribution functions for representative CO  $\Delta v = 1$  transitions synthesized with the 1-D version of the COmosphere model and the G94 oscillator strengths. The observations in the lower set of panels are mainly from the McMath-Pierce FTS, although the ATMOS spectra are overlaid on the disk center ( $\mu = 1$ ) profiles (and are indistinguishable). The simulated profiles were based on  $\epsilon_O = 846$  ppm (with C/O=0.5 and energy dependent corrections to the oscillator strengths to be described later [§3.3.3]). The optimum model matches the variation of CO core depths with increasing line strength (right to left) very well at disk center, and the center-limb behavior of the same features much better than the FALC or Asplund models (shown later [§3.3.4]).

In the upper two panels of Fig. 11, normalized contribution functions are displayed for  $\mu = 1$  (upper) and  $\mu = 0.152$  (lower). The curves furthest to the right in each panel are the  $4.66 \mu\text{m}$  continuum “intensity contribution functions,” and the curves to the left are for the CO transitions, calculated as “line depression contribution functions” at the line center frequency, as described by Magain (1986). The distinction between intensity and line depression contribution functions is important for the weaker CO lines (e.g., 7–6 R68) because the CO molecular concentration (top panel: diamonds) peaks higher in the photosphere than the narrow deeper zone where the IR continuum arises, and the optically thin line depression thus forms in layers entirely separate from the background continuum. However, for the stronger CO lines, the distinction between the two types of contribution functions is less important, because the line opacity completely dominates the continuum, at least at line center.

Figure 12 displays oxygen abundances derived for single component versions of the COmosphere and Asplund models (upper two, and middle two panels, respectively), and the two more recent sets of  $gf$ -values: G94 and HR96. In practice, we calculated CO line profiles for a grid of discrete oxygen abundances (10 covering the range of expected individual  $\epsilon_O$ ’s with logarithmic spacing); fitted Gaussian profiles to the simulated intensities to determine theoretical equivalent widths  $W_\omega$  as a function of  $\epsilon_O$  for that particular transition; then used the empirical value of the equivalent width, obtained through an identically motivated Gaussian fit to the observed lineshape, to solve for the oxygen abundance according to a low order polynomial match to the theoretical  $W_\omega(\epsilon_O)$  relation.

The resulting  $\epsilon_O$ ’s for the  $\Delta v = 1, 2$  samples are depicted in the right hand panels as

a function of lower state excitation energy,  $E_{\text{lower}}$ . The lighter dots generally to the left are the first overtone lines; the darker dots generally to the right are the higher excitation fundamental transitions. The hatched areas indicate the means and  $\pm 1\sigma$  standard deviations of the two separate samples, while the green line is a linear least squares fit to the two samples combined (utilizing a “ $2\sigma$ ” filter to eliminate outliers).

The apparent slope of the derived abundances with excitation energy could indicate either that the adopted thermal profile is too hot in the CO layers (note that the cooler Asplund model displays a shallower slope for the  $\epsilon_{\text{O}}-E_{\text{lower}}$  relation), or that the oscillator strength scale is systematically skewed ( $E_{\text{lower}}$  generally is a proxy for  $vJ$ ). Since we have carefully “calibrated” the temperatures of the CO layers, we initially adopted the second viewpoint (although, we also will consider the first alternative later [§3.4.2].) We thus corrected the oscillator strength scale according to the apparent slope of the  $\epsilon_{\text{O}}-E_{\text{lower}}$  relation, taking the true abundance from the intercept of the fit, assuming that the lower energy line strengths are better determined than those of the high- $vJ$  transitions. (The G94 line strengths were derived from empirical EDMFs based on laboratory measurements of low excitation CO transitions.) If the empirical abundances are represented as,

$$(\epsilon_{\text{O}})_i = (\epsilon_{\text{O}})_0 \times (1 + \Delta \times E_i) , \quad (1)$$

then the corrected oscillator strengths would be,

$$(gf)_i^{\text{corr}} = (gf)_i^{\text{orig}} \times (1 + \Delta \times E_i)^2 , \quad (2)$$

since the equivalent width in the unsaturated regime depends linearly on  $gf$  but quadratically on  $\epsilon_{\text{O}}$ . The effect of correcting the  $gf$ -values is illustrated in the lower two panels [“(gf)\*”] for the alternative oscillator-strength scales with the optimum COmosphere model. To guard against a systematic deviation between the  $\Delta v = 1$  and 2 line strength scales (as seen for example in Fig. 8 with HR96 versus G94) masquerading as a trend of  $\epsilon_{\text{O}}$  with  $E_{\text{lower}}$ , we also fitted the  $\Delta v = 1$  and 2 samples separately, again employing a  $2\sigma$  filter. However, in these initial comparisons we relied mainly on the combined fit. In essence, we treated the  $\Delta v = 1$  and 2 samples as partially redundant realizations of the same phenomenon—a dependence of  $\epsilon_{\text{O}}$  on  $E_{\text{lower}}$ —and utilized the combined sample for a collectively more refined view:  $\Delta v = 1$  for the higher energies,  $\Delta v = 2$  for the lower.

Figure 13 is a montage of  $\Delta v = 1, 2$   $^{12}\text{C}^{16}\text{O}$  profiles and simulated lineshapes for representative members of the abundance sample (40 fundamental and 40 first overtone lines in total: 20 + 20 are illustrated in the figure) and the single component COmosphere model with the best-fit  $\epsilon_{\text{O}}$  (846 ppm) and the empirically corrected  $gf$ -values. The weaker lines (with central residual intensities  $\geq 85\%$ ) were locally normalized to the continuum level

according to bins (green points) on either side of line center, away from the absorption depression itself. The specific features were chosen from a much larger sample on the basis of weakness and freedom from obvious blends: other CO transitions are the most common spectral contaminant in the thermal IR. The 7–6 R68 transition provides a connection to the groundbased center-limb line set. Table 3 lists the measured equivalent widths and FWHMs for the abundance sample lines, derived from Gaussian fits to the ATMOS/ATLAS-3 spectra.

### 3.3.4. Model Sensitivities

The top panel of Figure 14 compares the effect of the different test temperature stratifications on the center-limb behavior of strong and weak CO  $\Delta v = 1$  lines from the recent McMath-Pierce FTS observations described earlier (§2.2; the  $\mu = 1$  traces include the ATMOS spectra for comparison; the limb trace is for  $\mu = 0.152$ ). The darkening of the CO line cores with increasing line strength (from right to left) at disk center, and the darkening of the individual line cores from disk center to the extreme limb, carry a redundant imprint of the thermal profile of the mid- and high photospheric layers.

Here, the spectral simulations were based on  $\epsilon_O$ ’s specific to each thermal model, as derived from the  $\Delta v = 1, 2$  abundance sample, and with the empirical corrections to the oscillator strength scales. One notices that although all three models fairly well reproduce the disk center line depths, the Asplund and FALC models both are too warm at high altitudes to match the center-limb behavior (i.e., yielding core intensities higher than observed), at least in the stronger  $\Delta v = 1$  lines. Furthermore, the Asplund continuum levels are slightly lower, on the brightness temperature scale, both at disk center and the extreme limb. This is a consequence of the too steep temperature gradient of that model. Multicomponent (1.5-D) versions of the Asplund model, to mimic the thermal heterogeneity of the convection pattern, fail to improve the center-limb comparison.

The remaining panels of Fig. 14 illustrate the sensitivity of the CO lines, and center-limb behavior, to changes in a number of key parameters that affect the line formation, including modifications of the thermal structure itself. The panel labeled “ $\gamma$ ” depicts lineshapes synthesized for three values of the pressure broadening coefficient appearing in the dimensionless Voigt  $a$  parameter (which controls the Voigt profile shape adopted for the CO absorptions; the radiation damping parameter  $\gamma_{\text{rad}}$  is completely negligible for these lines owing to their small Einstein  $A$  values):

$$a_V = \frac{\gamma (n_H/10^{16}) (T/5000)^{\frac{1}{2}}}{\Delta\omega_D}, \quad (3)$$

where  $n_H$  is the neutral hydrogen density in  $\text{cm}^{-3}$ ,  $T$  is the temperature in K, and  $\Delta\omega_D$  is the

Doppler width in  $\text{cm}^{-1}$  (including thermal and turbulent broadening; “macroturbulence” was implemented by Gaussian smoothing the simulated profiles after the fact). The  $\gamma$  coefficients used in the figure are 0,  $2 \times 10^{-4}$ , and  $4 \times 10^{-4} \text{ cm}^{-1}$ ; the middle one being our preferred value, after considering a large number of very strong  $\Delta v = 1$  absorptions from the ATMOS traces. The pressure broadening has a relatively minor effect: exclusively in the line wings, and mainly confined to the strong, saturated transitions, as can be seen from the diagram. It usually is ignored in CO lineshape synthesis, but we include it here for completeness.

The panel labeled “ $\xi$ ” illustrates the effect of changing the radial microturbulence parameter over the range 0.25, 0.75, and  $1.25 \text{ km s}^{-1}$ . Again, the middle value is the preferred one (consistent with the depth-dependent velocity distributions in the middle photosphere given by Asplund et al. [2004] and FALC, and nearly identical to that adopted by L78). Since we adjusted the macroturbulence for each specific value of the radial  $\xi$  to reproduce the widths of (the fully resolved) weak lines at disk center, the effect of varying  $\xi$  on the  $\mu = 1$  profiles of even the stronger lines is relatively subtle. However, changing  $\xi$  also affects the turbulent pressure contribution to the total pressure, and thus modifies the density stratification to some extent, requiring a small adjustment to the  $m$  scale to maintain the continuum intensity calibration. Still, the overall effect on the disk center spectrum is relatively minor.

The effect of changing the tangential  $\xi$  (over the corresponding range 1.5, 2.0, and  $2.5 \text{ km s}^{-1}$ ) is more pronounced. The best fit value,  $2 \text{ km s}^{-1}$ , is substantially larger than the radial component. The fact that 7–6 R68—whose extreme limb contribution function overlaps the disk center peaks of the stronger lines—exhibits enhanced broadening at the limb suggests that the underlying  $\xi$  distribution truly is anisotropic. Like the pressure broadening, the turbulent velocity plays mainly a minor role in the thermal profile and abundance analysis, but we optimize the match to minimize any (small) systematic influence.

The fourth panel down illustrates the effect of altering the oxygen abundance over the range  $\epsilon_{\text{O}}/1.5$ ,  $\epsilon_{\text{O}}$ ,  $\epsilon_{\text{O}} \times 1.5$ , for the optimum value (846 ppm) derived with the single component COmosphere model (and C/O=0.5). Changing the oxygen abundance has the greatest influence on weak 7–6 R68 at disk center, although the effect is suppressed at the limb. The other stronger lines are much less affected at either viewing angle. This is because only 7–6 R68 at disk center is unsaturated ( $\tau \sim 1$ ), and thus its equivalent width responds strongly to abundance (as something like  $\epsilon_{\text{O}}^2$ , given the imposed fixed C/O ratio). The stronger lines, on the other hand, are partially to fully saturated ( $\tau \gg 1$ ), particularly at the extreme limb. They arise in the middle and upper photosphere where the temperature profile is relatively flat compared with the continuum forming layers. The effect of altering the oxygen abundance is to move the depth (and thus temperature) where the line core becomes opaque (and radiates like a blackbody at the  $\tau \sim 1$  temperature for these LTE

lines). However, because the temperature gradient is shallow, the temperature at the new depth is not much different from the old one, and thus the influence on the line core intensity is reduced.

The next two panels illustrate the consequences of modifying the photospheric thermal structure of the COmosphere test model. The panel labeled “ $T_{\text{OUTER}}$ ” changes the mid-photospheric temperature gradient. The lower distribution closely matches that of the FAL C model (which was derived largely from the behavior of the Ca II 0.395  $\mu\text{m}$  H and K line wings, a powerful diagnostic for thermal structure in the solar photosphere and stellar atmospheres in general [cf., Ayres & Linsky 1976, hereafter AL76]), while the upper two models are 200 K and 400 K hotter, respectively, at  $m = 0.01 \text{ gr cm}^{-2}$ , joining smoothly to the lower  $T(m)$  at  $m = 1 \text{ gr cm}^{-2}$ . Again, the middle model is our preferred temperature distribution. The main influence is concentrated on the strong lines at disk center, and the two weaker lines at the limb; but the weak lines at disk center and the strong lines at the limb are mostly unaffected. The weak lines at disk center are minimally influenced because they form deeper where the  $T_{\text{OUTER}}$  models converge in temperature. As for the strong lines at disk center, they have double-peaked contribution functions (Fig. 11), responding both to the  $T_{\text{min}}$  region as well as the upper photosphere near  $m = 0.01$ . It is the second bump that causes the larger changes in the strong line cores at  $\mu = 1$  for variations in  $T_{\text{OUTER}}$ . Similarly, the formation height for the weaker lines at the extreme limb moves up from the  $m \sim 1$  level, where the differences between the perturbed models are small, to the  $m \sim 0.1$  level where the temperature differences are larger. Meanwhile, the stronger lines at the extreme limb form almost exclusively in the  $T_{\text{min}}$  region, whose temperature is the same for the different  $T_{\text{OUTER}}$  models, so the line cores are minimally affected.

The bottom row of panels depict the influence of changing  $T_{\text{min}}$  over the range 3400, 3600, 3800 K, with again the middle value preferred. Here, the main effect is on the cores of the strongest lines at the extreme limb, since, as was mentioned above, their contribution functions peak at  $T_{\text{min}}$  for the highly slanted sight lines. A smaller effect is seen in 6–5 R47 at the limb, because of the double-peaked nature of its contribution function, but the influence on even weaker 7–6 R68 is minimal. The stronger lines at disk center show a similar level of response as 6–5 R47 at the extreme limb, again because of twin peaks in their contribution functions.

The final COmosphere model balanced these several levels of sensitivity:  $T_{\text{min}}$  altitude based on CO off-limb emission extensions,  $T_{\text{min}}$  temperature based on cores of strong CO lines at the limb, mid-photospheric  $T(m)$  from core-depth variation with line strength at disk center, and deep photosphere thermal profile from continuum absolute intensities and center-limb behavior; all with a self-consistent  $\epsilon_{\text{O}}$  (and  $\Delta$ ) derived from the reference abun-

dance sample. The model is not perfect, because it does not fully reproduce the center-limb behavior of 6–5 R47 and 7–6 R68. However, models that do match that observational constraint (like the cooler  $T_{\text{OUTER}}$  case) tend to fail other criteria (in this case, the distribution of core depths with increasing line strength at disk center). Nevertheless, the fact that a single  $T(m)$  distribution does so well for a wide range of the criteria gives us encouragement that we can exploit it as a basis to determine auxiliary properties, like the oxygen abundance; estimating the influence of, say, thermal inhomogeneities by treating them as 1.5-D perturbations of the reference model.

### 3.4. Abundance Simulations

We conducted abundance simulations for a wide range of thermal models, to test the sensitivities in a similar way as illustrated in Fig. 14. The results are summarized in Figures 15a (single- and multicomponent models) and 15b (parameter variations for 1-D COmosphere model), and in Table 4. The optimum single component COmosphere model yields a reference oxygen abundance of 846 ppm (with a gradient in  $\epsilon_{\text{O}} - E_{\text{lower}}$  of  $\Delta = -5.5\%$  per  $10^4 \text{ cm}^{-1}$ ), considerably higher than the “low”  $\epsilon_{\text{O}}$ ’s cited in §1 derived with the full 3-D Asplund model from atomic oxygen and hydroxyl lines. The single component version of the Asplund model gives a lower 575 ppm, and better consistency between the fundamental and first overtone line sets (i.e., a shallower gradient of  $\Delta = -2.9$ ). The 5 component Asplund model, again forcing the continuum calibration on the weighted average intensity, yields an oxygen abundance about 14% lower than the single component model (496 ppm with a *positive*  $\Delta = +1.7$ ). The 0.06 dex drop in the oxygen abundance from the mean model to the 5 component version is entirely consistent with the assessment by Asplund et al. (2004) of multicomponent effects; and the CO derived oxygen abundance is similar to what those authors obtained from O I and OH using their full model.

However, the lower oxygen abundance from CO is a direct consequence of the too steep temperature gradient of the Asplund model, which leads to cooler temperatures in the CO forming layers, enhanced column densities of absorbers, and thus a lower inferred  $\epsilon_{\text{O}}$ . We do acknowledge that the  $\Delta v = 1/\Delta v = 2$  dichotomy (in principle temperature-sensitive because it pits generally low excitation first overtone lines against mainly higher excitation fundamental transitions) does seem to favor the cooler temperatures of the Asplund model in those layers. But, because even small systematic errors in the CO oscillator strength scale could mimic that result, we prefer the more accurately known continuum properties to constrain the temperatures. (With the proviso that a full 3-D rendering of the continuum center-limb behavior might obtain a better match to the observations than the 1.5-D version

of the Asplund model, thereby negating our fundamental test.)

Applying the milder IRIS derived thermal perturbations in the CO layers to the COmosphere profile, and adding in the hot network component (FALC + 200 K at high altitudes, covering 10% of the area), yields 850 ppm ( $\Delta = -5.3$ ), virtually identical to the single component version. The FALC model predicts 820 ppm ( $\Delta = -5.6$ ). Changing the upper photosphere temperature gradient in the single component setting (“TOUTER” models) has a  $\sim \pm 10\%$  influence, but is constrained by the empirical distribution of CO core depths with increasing line strength.

In one of the cases, we altered the  $H^-$  f-f cross section relative to b-f by  $\pm 10\%$ , then carried out the continuum calibration procedure and oxygen abundance synthesis. Here, the photospheric temperature structure remains essentially the same as before, but now the depth of formation of the background continuum at  $2.5\ \mu m$  and  $5\ \mu m$  changes. This apparently affects  $\epsilon_O$  by only  $\sim \pm 2\%$ . In another case, we altered both the b-f and f-f cross sections by the same  $\pm 10\%$ , then carried out the calibration/abundance procedure. Here, the temperature structure is modified (by the continuum calibration) but the relative depths of formation of the visible and IR continua remain the same. The apparent effect on  $\epsilon_O$  is somewhat larger,  $\sim \pm 5\%$ .

The first case tests possible systematic errors in the relative cross sections, and the second, the absolute cross sections (assuming that the relative behavior is well determined). In both cases, the  $\pm 10\%$  perturbations in the cross sections are much larger than the few percent accuracy cited in the original studies. We also altered the CO dissociation energy  $D_0$  by  $\pm 0.100\text{ eV}$  ( $\sim 1\%$ ) which affects the derived oxygen abundance by  $\pm 10\%$ . We found that the “high” oxygen abundance predicted by the COmosphere model could be lowered to 450 ppm if  $D_0$  were raised to (an implausibly large) 11.750 eV. Changing the radial and tangential microturbulence parameters together by  $\pm 0.5\text{ km s}^{-1}$  alters the derived oxygen abundance by an insignificant  $< \pm 1\%$ .

Our initial conclusion is that a solar oxygen abundance in the neighborhood of 850 ppm is more compatible with the observed CO  $\Delta v = 1, 2$  spectra, than the  $\sim 400\text{ ppm}$  lower values obtained from analyses of atomic oxygen lines in the visible, and hydroxyl bands in the infrared.

#### 3.4.1. *Uncertainties*

Random errors of measurement are essentially negligible owing to the high S/N of the ATMOS spectra. Systematic errors must dominate the error budget, then, but are more

difficult to quantify. One important source is setting the continuum level, which becomes progressively more important the weaker the absorption line. The ATMOS traces are superior in this regard to typical visible solar spectra, since line crowding is much less in the thermal IR and telluric absorption is negligible. Consequently, there usually is a high density of intervals where the intensity ostensibly is flat and an accurate continuum level can be drawn in an unbiased way using numerical filtering techniques (e.g., Bennett & Ayres 1988). We carefully selected the abundance sample lines by examining essentially every possible CO transition in the 1600–2400 cm<sup>−1</sup> region, choosing only those which were minimally disturbed by nearby blends whose wings might alter the surrounding continuum level. Furthermore, we established a specific local continuum level for the weakest transitions by averaging the intensities in two bands several FWHMs to either side of line center.

The typical  $1\sigma$  dispersion in derived abundances among the lines of the  $\Delta v = 1, 2$  samples and the COmosphere model is about  $\pm 6\%$ , before compensation for the  $\epsilon_O - E_{\text{lower}}$  effect, and  $\pm 2\%$  after. The latter might be viewed as a minimal estimate of systematic errors due to the continuum normalization, and any higher order distortions of the G94 oscillator strength scale beyond the linear correction. Since we have no idea how correlated these errors might be over the line set, we cannot divide by  $\sqrt{N}$  to characterize the accuracy in terms of the standard error of the mean. Thankfully, the size of the error is small in any event.

Our tests indicated that the influence of uncertainties in continuum opacity cross sections are likely to be small, about the same as the errors above. Multicomponent effects are larger, depending on the detailed amplitudes of the rms temperature fluctuations in the line formation zone. As mentioned previously, Asplund et al. estimated 3-D effects of the same order ( $\sim 0.08$  dex [20 %]).

In order to exploit CO as an oxygen abundance indicator, we had to make an assumption concerning the C/O ratio, which we fixed at 0.5, based on a variety of previous studies. The range of C/O ratios shown in Fig. 1 is about 0.45–0.60, or  $\sim \pm 20\%$  around the nominal value. Meyer (1985) quotes a “Local Galactic” ratio of 0.56, and a solar energetic particle result of 0.45, nicely bracketing our assumed value. The oxygen abundance scales roughly as  $r_{\text{C/O}}^{-1/2}$ , so the uncertainties in  $r_{\text{C/O}}$  translate to  $\lesssim \pm 10\%$ , perhaps as small as  $\pm 5\%$  (taking Meyer’s LG and SEP results as a gauge of the true range of uncertainty in the C/O ratio).

The CO oscillator strengths also are an important potential source of systematic error. Intercomparison of the two recent compilations suggest  $< \pm 5\%$  absolute (which translates to a smaller error in  $\epsilon_O$  since  $(W_\omega)_{\text{obs}} \sim gf \epsilon_O^2 r_{\text{C/O}}$ ). Uncertainties in the model thermal profile were meant to be highly constrained by the continuum calibration and the behavior of the strong lines of the CO spectrum, but any systematic errors here would have a magnified

effect owing to the temperature sensitivity of CO. We assigned a conservative error to this source,  $\pm 10\%$  based on the  $T_{\text{OUTER}}$  perturbed models, which would dominate all the other sources (if the others are uncorrelated, and can be combined in quadrature).

Given the uncertainties that are easily identified, and quantified, we conclude that the solar oxygen abundance derived from CO is significantly different—and larger—than that inferred in recent years from other oxygen bearing species.

### 3.4.2. An Alternative “Optimum” Thermal Profile

In the preceding sections, we followed a chain of reasoning dictated by our belief that the continuum temperature calibration should be given precedence over the potential temperature proxy connected with an apparent slope of the derived  $\epsilon_{\text{O}}$ ’s with  $E_{\text{lower}}$ . After all, such a slope could result from a systematic skew in the CO oscillator strength scales with  $vJ$ . However, it also is true that the two recent studies on the issue, G94 and HR96, which took somewhat different tacks (see Chackerian et al. 1994), arrived at basically the same conclusions. While variations in the  $gf$ -scales with  $E_{\text{lower}}$  of a few percent per  $10^4 \text{ cm}^{-1}$  might be plausible, the effect on  $\epsilon_{\text{O}}$  should be only about half that; nevertheless we were finding as much as 6 % per  $10^4 \text{ cm}^{-1}$  for the  $\epsilon_{\text{O}}$ ’s of our optimum COmosphere model. Furthermore, the optimum model was less successful in matching the  $5 \mu\text{m}$  continuum center-limb behavior than, say, the 1-D version of the Asplund model (although much better in the visible), and did not reproduce the 7–6 R68 center-limb behavior particularly well either.

In the spirit of experimentation, we considered an alternative class of COmosphere models with a small temperature dip in the middle photosphere. If the dip is narrow enough, it will have little effect on the visible absolute intensities and center-limb behavior, and the disk center IR continuum; or on the stronger CO line cores, which form higher up. If the dip is deep enough, it can steepen the IR continuum center-limb behavior, flatten the  $\epsilon_{\text{O}}-E_{\text{lower}}$  relation, and improve the center-limb behavior of the key 7–6 R68 line.

With this in mind, we developed what we call the “Double Dip” model (the first, outer “dip” refers to the  $T_{\text{min}}$  region). We experimented with a variety of realizations of the model, changing the location  $m$  of the inner dip, its width  $\Delta m$  and depth  $\Delta T$  to optimize the match with the constraints discussed earlier. A 250 K temperature depression, at  $m \sim 0.35 \text{ gr cm}^{-2}$  with a width of a few tenths in  $m$ , and additionally lowering  $T_{\text{min}}$  by 100 K (to 3500 K), was found to maximize the agreement with those constraints.

Figure 16 depicts continuum center-limb curves synthesized with a 6 component rendering of the Double Dip model, demonstrating the improved agreement for the thermal IR

wavelengths, while maintaining a good match to the visible behavior. (Including the 10% network component caused us to further lower the  $T_{\min}$  of the mean profile by an additional 100 K [to 3400 K].) Figure 17a illustrates abundance solutions for 1- and 6 component versions of the model. Here we find that the fundamental displays an essentially flat slope, but the first overtone still is slightly tilted and displaced upward. (The apparent separation between the fundamental and first overtone abundances would have worsened with the HR96 *gf*-values.) Fig. 17b illustrates the CO center-limb behavior calculated with the 1- and 6 component Double Dip models, using oxygen abundances derived exclusively from the  $\Delta v = 1$  sample. Again, there is improved agreement with the observed center-limb behavior of 7–6 R68, while maintaining the core intensities of the stronger CO lines at disk center. We consider the 6 component Double Dip model to be the most self-consistent representation of the solar photosphere, of all the models we tested, at least in the empirical sense of matching CO and continuum behavior both at disk center and the extreme limb. Physical properties of the 6 component version of the Double Dip model are summarized in Table 5 (excluding  $\Delta T_{\text{rms}}$  and  $T_{\text{NW}}$ , which would be the same as in Table 2).

The 1-component version of the Double Dip model indicated  $\epsilon_{\text{O}} = 599$  ppm for  $\Delta v = 1$ , alone, with a gradient of  $\Delta = -0.1$ ; and 654 ppm for  $\Delta v = 1$  and 2 combined (with  $\Delta = -3.4$ ). The 6 component model, thanks partly to the hot “network” component, yielded a slightly higher 641 ppm ( $\Delta = -1.1$ ) for  $\Delta v = 1$  alone; and 685 ppm ( $\Delta = -3.6$ ) for  $\Delta v = 1$  and 2 combined. These  $\epsilon_{\text{O}}$ ’s are very similar to that recommended by GS98, prior to the more recent work of Asplund and collaborators.

We advance the Double Dip model because it reproduces most of the imposed observational constraints within the context of a 1.5-D thermal model (including allowance for the empirical mild thermal fluctuations indicated by the IRIS time series). However, while the primary thermal dip (“ $T_{\min}$ ”) above the photosphere can be understood within the context of strong CO radiative cooling (Ayres 1981) or dynamical effects connected with traveling acoustic waves (Carlsson & Stein 1995), the presence of a secondary depression in the average thermal profile of the middle photosphere would be unexpected. One can imagine that these not-so-shallow layers still would be dominated by radiative heating and cooling in the continuum, and even experience some convective overshooting (although empirically we see little evidence of that, at least in CO). It is worth noting, however, that the secondary dip does occur in the zone where the  $^{13}\text{C}^{16}\text{O}$   $\Delta v = 1$  bands arise, as well as the  $^{12}\text{C}^{16}\text{O}$  first overtone, which potentially could provide a small amount of localized radiative cooling, perhaps enough to create a modest temperature depression. Alternatively, the inner dip might simply mark the altitude above which nonradiative heating imposes a few hundred degree temperature “hump,” before the strong CO cooling can reverse the temperature profile in higher layers.

Even though we must be skeptical concerning the reality of the Double Dip structure, we retain it in the ensuing discussion as an example of the range of thermal profiles allowed by the empirical constraints, and leave it for future work to explore its reality.

### 3.4.3. *The Solar Oxygen Abundance from CO*

A summary of the preceding sections is as follows. An optimum smooth thermal profile—COmosphere—which includes mild thermal perturbations and a minority hot “network” component, satisfies most of the imposed observational constraints and yields an oxygen abundance of around 850 ppm. However, the inferred dependence of derived  $\epsilon_O$  on  $E_{\text{lower}}$  for the individual  $\Delta v = 1, 2$  transitions could be viewed as too extreme to be a systematic error in the  $gf$ -value scales (although that should be checked experimentally), and suggests that the temperatures in the CO formation zone are too warm. A stripped down version of the Asplund 3-D convection simulation, rendered as a 5 component 1.5-D model centered on the reported mean thermal structure with flanking smooth perturbations to capture the cited rms temperature fluctuations, yields an oxygen abundance of around 500 ppm (now with a positive  $\Delta \sim +2$ ), in agreement with the original work of Asplund et al.; but rather poorly matches the pivotal continuum center-limb test, and the center-limb behavior of strong CO  $\Delta v = 1$  lines. All models, or CO parameter modifications, crafted to reproduce the low O abundance of 460 ppm, fail either the continuum or CO tests, or violate cited laboratory or theoretical uncertainties. A compromise—but perhaps physically challenged—Double Dip model, including mild thermal fluctuations and a minority network component, matches the observational constraints better than any of the smooth thermal profiles, and yields an oxygen abundance of around 650 ppm. We believe that the truth lies somewhere between COmosphere and Double Dip, probably closer to the latter. We thus propose that the solar CO rovibrational spectrum is most consistent with an oxygen abundance in the neighborhood of 700 ppm, but acknowledge that model dependent (and other) systematic errors could be large, perhaps as much as  $\pm 100$  ppm. (The corresponding carbon abundance would be 350 ppm.)

## 3.5. **The Isotopes of Carbon and Oxygen**

Isotopic ratios of the abundant light elements provide insight into the history of galactic chemical evolution (Langer & Penzias 1993), and photochemical and other fractionation processes in primitive solar system material (Krot et al. 2005). Theoretical predictions indicated that solar isotopic abundances would be only a few tenths of a percent larger

than terrestrial standard values (Wiens, Burnett, & Huss 1997), providing the motivation for NASA’s recent *Genesis* Discovery mission to achieve extremely high accuracy through direct capture of the light ions and their isotopes from the solar wind (Burnett et al. 2003).

The best recent spectroscopic study of the main isotopes of carbon and oxygen in the Sun was that of Harris, Lambert, & Goldman (1987), based on CO fundamental lines observed with an FTS instrument in a high altitude balloon flight. They concluded that the venerable Holweger–Müller (1974, hereafter HM74) photospheric model was most consistent with visible continuum center-limb behavior and properties of the CO fundamental spectrum. They obtained  $^{12}\text{C}/^{13}\text{C} = 84 \pm 5$  and  $^{16}\text{O}/^{18}\text{O} = 440 \pm 50$ , as well as  $\epsilon_{\text{C}} = 513 \pm 120$  ppm. The  $^{12}\text{C}^{17}\text{O}$  spectrum was too weak in their scans to measure. The mid-photospheric temperature profile of HM74 is very similar to the FALC (and the COmosphere class of models), since the FALC was derived to fit the photospheric damping wings of the Ca II resonance lines, which the HM74 model does very well (A77).

Figure 18, similar to Fig. 15, illustrates abundance ratio analyses applied to samples of weak lines from the  $\Delta v = 1$  bands of  $^{13}\text{C}^{16}\text{O}$ ,  $^{12}\text{C}^{17}\text{O}$ , and  $^{12}\text{C}^{18}\text{O}$ . ( $\Delta v = 2$  transitions of  $^{13}\text{C}^{16}\text{O}$  are found in the ATMOS spectra, but are extremely weak and therefore add little to the already extensive sample of stronger  $\Delta v = 1$  lines.) The isotopic ratios were derived by a procedure similar to the oxygen abundances described previously, although the observed equivalent widths were determined by a more constrained Gaussian modeling utilizing the predicted line position and a fixed FWHM (4.05 km s<sup>-1</sup>, based on unconstrained fitting of the highest S/N lines of the  $^{13}\text{C}^{16}\text{O}$  abundance sample). The measured values are listed in Table 6. In the line synthesis, the (model dependent) empirical corrections to the oscillator strength scales, derived from the  $^{12}\text{C}^{16}\text{O}$  sample, were applied to the isotopic transitions. Results from representative models are listed in Table 7. Two sets of ratios are presented: one based on  $\epsilon_{\text{O}}$  derived from the full sample of  $\Delta v = 1, 2$  transitions; the second based on  $\epsilon_{\text{O}}$  exclusively from  $\Delta v = 1$ .

One sees, in general, that the isotopic ratios are much less sensitive to even rather drastic changes in the model thermal structures than the absolute abundances. Furthermore, the large samples, especially for  $^{13}\text{C}$  and  $^{18}\text{O}$ , imply small statistical uncertainties, particularly if we are allowed to consider the standard error of the mean (assuming that the dispersion of values arises from uncorrelated errors). Figure 19 illustrates representative isotopic profiles synthesized with the single component COmosphere model.

The isotopic abundance ratios derived from CO should be more secure than  $\epsilon_{\text{O}}$ , itself, since we obtained consistent results nearly independently of the thermal model. For the final values, we considered the 6 component versions of both COmosphere and Double Dip. These empirically capture our best estimates of the mid-photospheric temperature profile and

thermal fluctuations about it, including the presence of a small percentage of hot network elements. The Double Dip model, in particular, has the flattest distribution of  $\Delta v = 1$   $\epsilon_O - E_{\text{lower}}$  of all the models that fit the continuum calibration and the CO center-limb data. Although we have argued that the Double Dip model might not be as physically plausible as some of the others, this criticism probably is less germane in a differential comparison, such as performed here for the isotopic abundance ratios. Flatness of the  $\epsilon_O - E_{\text{lower}}$  relation is important because we are comparing generally low excitation isotopomers to generally higher excitation parent molecules, thus any temperature dependent biases can skew the derived isotopic ratios. In this regard, the Double Dip model does display an apparent separation between the  $\Delta v = 1$  and 2 abundances, particularly conspicuous in the single component version. We therefore elected to consider only the  $\epsilon_O - E_{\text{lower}}$  relation for  $\Delta v = 1$  to derive the isotopic abundances, whereas for the other classes of models—COmosphere in particular—we considered the  $\Delta v = 1, 2$  results together; imagining that the fundamental and overtone bands were suffering the same systematic error in their  $gf$ -values, and exploiting the  $\Delta v = 2$  transitions to provide additional information on the abundance-excitation gradient, and abundance intercept, where the  $\Delta v = 1$  coverage is sparse.

We point out that the 1-D mean version of the Asplund model yields isotopic ratios in good agreement with those from COmosphere and Double Dip, but the 5 component variant predicts larger ratios (actually in quite good agreement with terrestrial values, unlike those from the other models: see below). The increase (corresponding to smaller isotopic abundances) undoubtedly arises from the same general effect that lowers the  $\epsilon_O$  abundance itself going from the single component thermal profile to the large temperature contrasts of the multicomponent model, accentuated by the fact that the isotopic transitions, as mentioned above, are mostly low excitation whereas the abundance sensitive  $\Delta v = 1$  lines are mainly high excitation. However, we have dismissed the large temperature excursions of the Asplund model in the CO formation zone owing to the empirical lack of significant temperature fluctuations in either the cores of weak CO lines like 7–6 R68 or in the deeper seated 5  $\mu\text{m}$  continuum.

Our recommended values of the isotopic ratios, taken as an average of COmosphere\*6 ( $\epsilon_O[\Delta v = 1, 2]$ ) and Double Dip\*6 ( $\epsilon_O[\Delta v = 1]$ ) are:  $^{12}\text{C}/^{13}\text{C} = 80 \pm 1$ ,  $^{16}\text{O}/^{17}\text{O} = 1700 \pm 220$ , and  $^{16}\text{O}/^{18}\text{O} = 440 \pm 6$ , where the cited uncertainties are standard errors of the mean. Ironically, these values possibly will be more accurate than those obtained *in situ* from the solar wind by NASA’s ill-fated *Genesis* mission, depending on how successfully extraterrestrial material can be recovered from the damaged return capsule (McNamara et al. 2005).

The specific values of the isotopic ratios deserve comment. In the solar system context, isotopic abundances conventionally are expressed as differences with respect to reference

terrestrial values in parts per thousand (per mil: ‰) according to, for example,  $\delta^{13}\text{C} \equiv [\epsilon(^{13}\text{C})_{\odot}/\epsilon(^{13}\text{C})_{\text{standard}}] - 1] \times 10^3$ . In previous solar studies, the uncertainties associated with the isotopic ratios were large enough that the observed solar values generally were taken to be consistent with the terrestrial ratios (based on the Vienna Standard Mean Ocean Water [V-SMOW] mixture for the oxygen isotopes and Vienna PeeDee Belemnite [V-PDB] for carbon: Gonfiantini, Stichler, & Rozanski 1995;  $^{12}\text{C}/^{13}\text{C} = 89.2 \pm 0.2$  [ibid., Table 3],  $^{16}\text{O}/^{17}\text{O} = 2632 \pm 5$  [ibid., Table 1], and  $^{16}\text{O}/^{18}\text{O} = 498.7 \pm 0.1$  [ibid., Table 1]). Lunar and Martian isotopic ratios are very close to Earth’s; while those inferred for asteroids from meteoritic analyses cover a wider range, but still deviate from terrestrial by less than 20 ‰ (Burnett et al. 2003). Some extraterrestrial materials show large isotopic deficiencies, reaching  $-60\text{ ‰}$  for the oxygen isotopes in calcium-aluminum inclusions of chondritic meteorites in extreme cases (Wiens et al. 2004).

Theoretical predictions of solar isotopic ratios—thought to be essentially identical to those of the original solar nebula—based on fractionation processes in the gas-dust chemistry were only a few ‰ larger than the terrestrial values, necessitating the very high precision measurements intended for *Genesis*, as mentioned above. Now, with the much smaller uncertainties of the present work, we see that the solar ratios deviate from the terrestrial values by much larger factors than anticipated by the previous theoretical models:  $\delta^{13}\text{C} \sim +115 \pm 14\text{ ‰}$ ,  $\delta^{17}\text{O} \sim +550 \pm 200\text{ ‰}$ , and  $\delta^{18}\text{O} \sim +133 \pm 16\text{ ‰}$ . It seems that isotopic fractionation theories for primitive solar system material incorporated into the inner planets are in need of some revision.

The carbon isotope  $^{13}\text{C}$  is a secondary product of nuclear processing, through the CNO cycle, requiring a seed abundance of  $^{12}\text{C}$  from previous generations of primary production (helium burning); thus  $^{12}\text{C}/^{13}\text{C}$  is expected generally to decrease as the Galaxy ages, and display a distinct gradient with Galactocentric distance (Wilson & Rood 1994, hereafter WR94). The solar  $^{12}\text{C}/^{13}\text{C}$  ratio, however, now is closer to, although still larger than, those seen in nearby interstellar clouds ( $62 \pm 4$ : Langer & Penzias 1993;  $77 \pm 7$ : WR94;  $59 \pm 2$ : Lucas & Liszt 1998) and star-forming regions like Orion ( $40\text{--}70$ : Savage et al. [2002]). This might modify the notion that substantial enrichment of  $^{13}\text{C}$  has occurred in the Galaxy over the past 4.6 Gyr since the formation of the solar system (Savage et al. 2002).

#### 4. Discussion

Through a multifaceted analysis of CO infrared rovibrational bands, we have investigated the thermal structure of the solar photosphere, and as a byproduct derived abundances of C, O, and their main isotopes. The  $\epsilon_{\text{O}}$ , in particular, is similar to values recommended

a decade ago, compatible with helioseismological constraints, but is significantly larger than reported in recent studies of OH and O I exploiting sophisticated simulations of solar surface convection. We now can understand at least the molecular side of the dichotomy straightforwardly: as was demonstrated in §3.3.1, the temperature gradient of the mean Asplund model is too steep in the visible continuum forming layers. Consequently, the model is somewhat too cool in the higher layers where the infrared OH lines arise. This leads to the inference of a smaller oxygen abundance from the hydroxyl spectrum (and from CO, as well).

On the other hand, the behavior of the O I  $0.630\text{ }\mu\text{m}$  forbidden line—main oxygen diagnostic in the previous work—cannot be explained similarly. The transition arises from the ground state of a majority species, and thus should be relatively immune to thermal effects (see L78). Perhaps the  $0.630\text{ }\mu\text{m}$   $gf$ -value is not as securely established as believed, or the Ni I blend is less significant than thought. One certainly should be wary, in any case, when an important abundance is tied so strongly to essentially a singular spectral feature.

At the same time, one should ask what is the proper role of *ab initio* models such as that of Asplund and colleagues, versus semiempirical thermal stratifications such as derived by E. H. Avrett and collaborators? Clearly, an *ab initio* model is intended to provide direct insight into the fundamental physical processes that govern, say, the structure and dynamics of the solar photosphere. The Asplund model meets this requirement by accurately reproducing the details of velocity induced lineshape distortions (encoded in the so-called C-shaped line bisectors), and general characteristics of the time dependent brightness pattern of granular convection cells. Yet, the model is not a perfect representation of the solar atmosphere because it does not predict other key properties, such as the chromospheric temperature rise (or, the temperature *fall* of the COmosphere), or magnetic-related phenomena such as G-band bright points and Ca II network elements. This, of course, is not the point of the Asplund model, and it should not be faulted for failing tests outside of its intended purview. Nevertheless, because the model is in some respects not a flawless representation of the solar atmosphere, it should be used with caution in roles outside of its defined domain. Deriving solar abundances would be a good example of an area where it would be prudent to exercise such caution.

Semiempirical models, on the other hand, provide little in the way of direct physical insight, in and of themselves; but can be used to calculate ancillary quantities (such as chromospheric radiative losses) which are of interpretive value (VAL81). A semiempirical model, nevertheless, to the extent that it successfully captures mean thermal properties of the atmosphere, could be considered more satisfactory for abundance work. Deficiencies of 1-D models relative to, say, a fully time dependent spatially resolved convection simulation probably are not as important as accurately mimicking the mean thermal profile, as far

as most abundance studies are concerned; and the influence of thermal heterogeneity can be investigated to some extent by imposing 1.5-D thermal perturbations around the basis model, as in the present work. Again, the Asplund et al. study, itself, demonstrated that the thermal inhomogeneities of the deep photosphere have a relatively minor influence on the oxygen abundance, at least as derived from the O I spectrum.

Nevertheless, it would be foolish for us to claim a definitive solution to the oxygen crisis. Deriving  $\epsilon_O$  from CO clearly is highly model dependent, and there are enough inconsistencies for the optimum COmosphere model—with regard to the center-limb behavior of weak CO lines like 7–6 R68, and the small but significant discrepancies between abundances derived from  $\Delta v = 1$  versus  $\Delta v = 2$  lines—that we view our contrary result mainly as an indication that a low solar oxygen abundance is not fully consistent with all the available diagnostics, and certainly merits further consideration. One important issue is the C/O ratio. Increasing it above the assumed 0.5 would allow a decrease of the inferred oxygen abundance, although to achieve the low proposed  $\epsilon_O$  would require C/O  $\gtrsim 1$ . Elevating the Sun to the status of a “carbon star” certainly would be more controversial than the low O problem itself.

With regard to the apparent variations of the theoretical rovibrational oscillator strengths with lower state excitation energy, which we have treated as a systematic error and corrected: the viability of our proposal could be pursued in refined calculations of the dipole matrix elements, and new laboratory measurements of high temperature CO. However, it also is possible that the consistent behavior of the predicted CO equivalent widths with excitation energy for the Asplund class of models, which—coincidentally or not—yields a low O abundance of  $\sim 500$  ppm, is not accidental, but rather is conveying a fundamental message concerning our ability to constrain the thermal properties of the middle photosphere empirically. The Double Dip model is one answer to that possibility, but its physical reality remains to be tested by independent observations, such as of the Ca II wings (AL76), or other potential mid-photosphere thermal tracers.

Finally, while atmospheric thermal profiling and abundance studies might seem less fashionable than searches for exosolar planets or the elusive dark matter (or dark energy, for that matter), the fundamental importance of such basic quantities across diverse areas of astrophysics should not be questioned.

This work was supported by grant AST-9987414 from the National Science Foundation and NAG5-13058 from the National Aeronautics and Space Administration. We thank T. Woods for providing an electronic version of the Thuillier et al. ATLAS-3 solar irradiance reference spectrum; R. L. Kurucz for providing an advance copy of his high resolution solar irradiance atlas; and R. L. Kurucz and J. L. Linsky for helpful comments. More detailed

parameters for the thermal models described in this study are available from the first author by request.

## REFERENCES

Abrams, M. C., Goldman, A., Gunson, M. R., Rinsland, C. P., & Zander, R. 1999, *Appl. Opt.*, 35, 2747

Allende Prieto, C., Lambert, D. L., & Asplund, M. 2002, *ApJ*, 573, L137

Antia, H. M., & Basu, S. 2005, *ApJ*, 620, L129

Asensio Ramos, A., Trujillo Bueno, J., Carlsson, M., & Cernicharo, J. 2003, *ApJ*, 588, L61

Asplund, M., Grevesse, N., Sauval, A. J., Allende Prieto, C., & Kiselman, D. 2004, *A&A*, 417, 751

Asplund, M., Ludwig, H.-G., Nordlund, Å., & Stein, R. F. 2000a, *A&A*, 359, 669

Asplund, M., Nordlund, Å., Trampedach, R., Allende Prieto, C., & Stein, R. F. 2000b, *A&A*, 359, 729

Auer, L. 1976, *JQSRT*, 16, 931

Auer, L. H., Heasley, J. N., & Milkey, R. W. 1972, *Kitt Peak National Observatory Contribution*, No. 555 (AHM73)

Ayres, T. R. 1977, *ApJ*, 213, 296 (A77)

Ayres, T. R. 1978a, *Sol. Phys.*, 57, 19

Ayres, T. R. 1978b, *ApJ*, 225, 665

Ayres, T. R. 1981, *ApJ*, 244, 1064

Ayres, T. R. 2000, *Sol. Phys.*, 193, 273

Ayres, T. R. 2002, *ApJ*, 575, 1104 (A02)

Ayres, T. R., & Brault, J. W. 1990, *ApJ*, 363, 705 (AB90)

Ayres, T. R., & Linsky, J. L. 1976, *ApJ*, 205, 874 (AL76)

Ayres, T. R., & Rabin, D. 1996, *ApJ*, 460, 1042 (AR96)

Ayres, T. R., & Testerman, L. 1981, *ApJ*, 245, 1124 (AT81)

Ayres, T. R., & Wiedemann, G. R. 1989, *ApJ*, 338, 1033 (AW89)

Bahcall, J. N., Basu, S., & Pinsonneault, M. H. 2003, in *Dynamic Sun*, ed. B. N. Dwivedi (Cambridge (UK): Cambridge University Press), 8

Bahcall, J. N., Basu, S., Pinsonneault, M., & Serenelli, A. M. 2005, *ApJ*, 618, 1049

Bahcall, J. N., Krastev, P. I., & Smirnov, A. Y. 1999, *Phys. Rev. D*, 60, 093001

Bahcall, J. N., & Serenelli, A. M. 2005, *ApJ*, 626, 530

Bennett, J. O., & Ayres, T. R. 1988, *PASP*, 100, 1129

Brault, J. W. 1978, *Pubblicazioni della Universita degli Studi di Firenze*, 106, 33

Burnett, D. S., et al. 2003, *Space Science Reviews*, 105, 509

Carbon, D. F., & Gingerich, O. 1969, *Proceedings of the 3rd Harvard-Smithsonian Conference on Stellar Atmospheres*, ed. O. Gingerich (Cambridge, Mass.: MIT), 377

Carlsson, M., & Stein, R. F. 1995, *ApJ*, 440, L29

Carlsson, M., Stein, R. F., Nordlund, Å., & Scharmer, G. B. 2004, *ApJ*, 610, L137

Chackerian, C., Goorvitch, D., Hure, J. M., & Roueff, E. 1994, *JMoSp*, 165, 583

Drake, J. J., & Testa, P. 2005, *Nature*, 436, 525

Farmer, C. B. 1994, *IAU Symp. 154: Infrared Solar Physics*, ed. D. M. Rabin, J. T. Jefferies, & C. Lindsey (Dordrecht: Kluwer Academic Publishers), 511

Fontenla, J. M., Avrett, E. H., & Loeser, R. 1993, *ApJ*, 406, 319 (FAL93)

Gonfiantini, R., Stichler, W., & Rozanski, K. 1995, *IAEA-TECDOC-825* (Vienna: International Atomic Energy Agency), 13

Goorvitch, D. 1994, *ApJS*, 95, 535 (G94)

Gray, D. F. 1976, *The Observation and Analysis of Stellar Photospheres*, (New York: Wiley-Interscience)

Grevesse, N., & Anders, E. 1991, in *Solar Interior and Atmosphere*, ed. A. N. Cox, W. C. Livingston, & M. S. Matthews (Tucson: University of Arizona Press), 1227 (GA91)

Grevesse, N., & Sauval, A. J. 1998, *Space Science Reviews*, 85, 161 (GS98)

Harris, M. J., Lambert, D. L., & Goldman, A. 1987, *MNRAS*, 224, 237

Holweger, H., & Müller, E. A. 1974, *Sol. Phys.*, 39, 19 (HM74)

Hure, J. M., & Roueff, E. 1996, *A&AS*, 117, 561 (HR96)

John, T. L. 1988, *A&A*, 193, 189

Kirby-Docken, K., & Liu, B. 1978, *ApJS*, 36, 359 (KL78)

Kopp, G., et al. 2005, in preparation

Krot, A. N., et al. 2005, *ApJ*, 622, 1333

Kurucz, R. L. 1970, *SAO Special Report*, 309

Kurucz, R. L. 1985, *CfA Preprint Ser.* 2162

Lambert, D. L. 1978, *MNRAS*, 182, 249 (L78)

Langer, W. D., & Penzias, A. A. 1993, *ApJ*, 408, 539

Leenaarts, J., & Wedemeyer-Böhm, S. 2005, *A&A*, 431, 687

Lenz, D. D., & Ayres, T. R. 1992, *PASP*, 104, 1104

Linsky, J. L. 1968, Ph.D. Thesis, Harvard University

Lucas, R., & Liszt, H. 1998, *A&A*, 337, 246

Magain, P. 1986, *A&A*, 163, 135

McNamara, K. M., Westphal, A. J., Butterworth, A. L., & Burnett, D. S. 2005, 36th Annual Lunar and Planetary Science Conference, 36, 2406

Meyer, J.-P. 1985, *ApJS*, 57, 173

Morton, D. C., & Noreau, L. 1994, *ApJS*, 95, 301 (MN94)

Neckel, H., & Labs, D. 1984, *Sol. Phys.*, 90, 205 (NL84)

Neckel, H., & Labs, D. 1994, *Sol. Phys.*, 153, 91 (NL94)

Noyes, R. W., & Hall, D. N. B. 1972a, *BAAS*, 4, 389

Noyes, R. W., & Hall, D. N. B. 1972b, *ApJ*, 176, L89

Peach, G. 1970, *Mem. RAS*, 73, 1

Pierce, A. K., & Slaughter, C. D. 1977, *Sol. Phys.*, 51, 25

Pierce, A. K., Slaughter, C. D., & Weinberger, D. 1977, *Sol. Phys.*, 52, 179

Puschmann, K., Vázquez, M., Bonet, J. A., Ruiz Cobo, B., & Hanslmeier, A. 2003, *A&A*, 408, 363

Rabin, D. 1994, IAU Symp. 154: Infrared Solar Physics, ed. D. M. Rabin, J. T. Jefferies, & C. Lindsey (Dordrecht: Kluwer Academic Publishers), 449

Sánchez Cuberes, M., Bonet, J. A., Vázquez, M., & Wittmann, A. D. 2000, *ApJ*, 538, 940

Sánchez Cuberes, M., Vázquez, M., Bonet, J. A., & Sobotka, M. 2003, *A&A*, 397, 1075

Savage, C., Apponi, A. J., Ziurys, L. M., & Wyckoff, S. 2002, *ApJ*, 578, 211

Solanki, S. K., Livingston, W., & Ayres, T. 1994, *Science*, 263, 64

Spickler, P. T., Benner, D. C., & Russell, J. M. 1996, *Sol. Phys.*, 165, 23 (SBR96)

Thuillier, G., Floyd, L., Woods, T. N., Cebula, R., Hilsenrath, E., Hersé, M., & Labs, D. 2004, *Advances in Space Research*, 34, 256 (T04)

Thuillier, G., Hersé, M., Labs, D., Foujols, T., Peetermans, W., Gillotay, D., Simon, P. C., & Mandel, H. 2003, *Sol. Phys.*, 214, 1

Timmes, F. X., Woosley, S. E., & Weaver, T. A. 1995, *ApJS*, 98, 617

Tsuji, T. 1977, *PASJ*, 29, 497

Vernazza, J. E., Avrett, E. H., & Loeser, R. 1973, *ApJ*, 184, 605 (VAL73)

Vernazza, J. E., Avrett, E. H., & Loeser, R. 1976, *ApJS*, 30, 1

Vernazza, J. E., Avrett, E. H., & Loeser, R. 1981, *ApJS*, 45, 635 (VAL81)

Uitenbroek, H. 2000a, *ApJ*, 531, 571

Uitenbroek, H. 2000b, *ApJ*, 536, 481

Uitenbroek, H., Noyes, R. W., & Rabin, D. 1994, *ApJ*, 432, L67 (UNR94)

Warren, H. P. 2005, ApJS, 157, 147

Wedemeyer-Böhm, S., Kamp, I., Bruls, J., & Freytag, B. 2005, arXiv:astro-ph/0503496

Wiens, R. C., Burnett, D. S., & Huss, G. R. 1997, Lunar and Planetary Institute Conference Abstracts, 28, 1553

Wiens, R. C., Burnett, D. S., McKeegan, K. D., Thiemens, M. H., Franchi, I. A., Bochsler, P., & Mao, P. 2004, Lunar and Planetary Institute Conference Abstracts, 35, 1296

Willson, R. C. 2005, AGU Spring Meeting Abstracts, 2

Wilson, T. L., & Rood, R. 1994, ARA&A, 32, 191 (WR94)

Table 1. Absolute Continuum Intensities

$\lambda$ ( $\mu\text{m}$ )	$\mathcal{F}_\lambda/\pi I_\lambda$	$I_\lambda$ ( $10^6 \text{ ergs cm}^{-2} \text{ s}^{-1} \text{ sr}^{-1} \text{ \AA}^{-1}$ )
0.400	0.728	4.501
0.420	0.743	4.710
0.440	0.756	4.687
0.460	0.767	4.536
0.480	0.777	4.330
0.500	0.785	4.110
0.520	0.793	3.903
0.540	0.800	3.718
0.560	0.806	3.555
0.580	0.812	3.406
0.600	0.818	3.263
0.620	0.824	3.118
0.640	0.829	2.967
0.660	0.834	2.817
0.680	0.839	2.682
0.700	0.843	2.597

Note. — The  $1\sigma$  standard deviation on the polynomial fit to the calibrated highpoints was  $\pm 0.9\%$ . This represents an estimate of the limiting precision due to uncorrelated systematic (and random) errors. The absolute accuracy of the intensity scale, as normalized to the TSI, is thought to be better than 0.1%.

Table 2. The COmosphere Model

$\log m$ (gr cm $^{-2}$ )	$\log \tau_{0.5}$	$z$ (km)	$T$ (K)	$\Delta T_{\text{rms}}$ (K)	$T_{\text{NW}}$ (K)
−4.00	−5.07	−1280	6625	100	6853
−3.80	−4.88	−1204	6475	100	6702
−3.60	−4.75	−1130	6332	100	6557
−3.40	−4.64	−1058	6107	100	6426
−3.20	−4.60	−995	4857	100	6299
−3.00	−4.59	−946	3844	100	6179
−2.80	−4.58	−903	3543	99	6058
−2.60	−4.55	−862	3500	96	5926
−2.40	−4.51	−821	3610	92	5760
−2.20	−4.43	−778	4019	86	5516
−2.00	−4.32	−728	4399	80	5228
−1.80	−4.17	−677	4450	72	4949
−1.60	−3.95	−626	4473	64	4744
−1.40	−3.68	−575	4497	55	4613
−1.20	−3.36	−523	4520	47	4592
−1.00	−3.03	−471	4548	40	4627
−0.90	−2.86	−444	4580	37	4662
−0.80	−2.69	−418	4621	34	4705
−0.70	−2.51	−391	4660	32	4744
−0.60	−2.34	−364	4700	29	4785
−0.50	−2.16	−337	4744	28	4831
−0.40	−1.99	−310	4791	26	4879
−0.30	−1.81	−282	4838	25	4926
−0.20	−1.64	−255	4887	24	4975
−0.10	−1.46	−226	4935	24	5021

Table 2—Continued

$\log m$ (gr cm $^{-2}$ )	$\log \tau_{0.5}$	$z$ (km)	$T$ (K)	$\Delta T_{\text{rms}}$ (K)	$T_{\text{NW}}$ (K)
+0.00	-1.28	-198	4977	24	5077
+0.05	-1.19	-184	5002	24	5111
+0.10	-1.10	-169	5050	24	5150
+0.15	-1.02	-155	5112	24	5199
+0.20	-0.93	-140	5180	24	5258
+0.25	-0.84	-125	5260	24	5327
+0.30	-0.75	-110	5350	23	5402
+0.35	-0.65	-95	5454	24	5490
+0.40	-0.56	-79	5572	26	5591
+0.45	-0.46	-63	5705	37	5702
+0.50	-0.35	-46	5841	55	5859
+0.55	-0.24	-30	6006	108	6070
+0.60	-0.10	-12	6224	215	6319
+0.65	+0.06	+6	6566	387	6650
+0.70	+0.29	+25	7185	634	7146
+0.75	+0.62	+47	7970	790	7798
+0.80	+1.00	+71	8606	772	8530
+0.85	+1.33	+96	8955	646	9279

Table 3.  $^{12}\text{C}^{16}\text{O}$  FWHMs and Equivalent Widths for  $\Delta v = 1, 2$  Bands

Transition	$\omega_0$ (cm $^{-1}$ )	$E_{\text{lower}}$ (cm $^{-1}$ )	FWHM (km s $^{-1}$ )	$W_\omega$ (10 $^{-3}$ cm $^{-1}$ )
1–0 P 96	1635.859	17376	4.35±0.03	2.060±0.014
1–0 P 90	1674.640	15337	4.51±0.01	3.203±0.009
1–0 R106	2322.725	21025	4.19±0.02	2.353±0.013
1–0 R109	2320.247	22180	4.20±0.02	1.815±0.007
2–1 R 0	2120.566	2143	4.73±0.01	6.905±0.010
2–1 R112	2286.814	25283	4.29±0.02	1.440±0.008
2–1 R118	2279.315	27701	3.96±0.06	0.723±0.012
3–2 P 88	1640.640	18670	4.53±0.02	3.062±0.014
3–2 R108	2260.499	25640	4.23±0.02	1.735±0.008
4–3 P 80	1666.616	18212	4.64±0.01	3.800±0.012
4–3 P 2	2056.515	6361	4.76±0.01	6.468±0.015
4–3 R118	2218.067	31415	4.19±0.06	0.444±0.007
5–4 P 75	1672.976	18775	4.65±0.01	3.748±0.010
5–4 P 3	2026.533	8436	4.69±0.02	5.979±0.027
5–4 R 0	2041.423	8414	4.30±0.01	3.120±0.011
5–4 R105	2202.920	28281	4.10±0.02	1.150±0.006
5–4 R110	2198.043	30129	4.18±0.04	0.718±0.007
6–5 P 72	1666.903	19928	4.56±0.01	3.314±0.009
6–5 R107	2171.091	30847	4.10±0.09	0.637±0.015
7–6 P 5	1966.891	12518	4.51±0.01	4.310±0.007
7–6 P 4	1970.664	12500	4.40±0.01	3.788±0.011
7–6 P 1	1981.778	12467	4.12±0.03	1.346±0.011
7–6 R 68	2143.690	20857	4.60±0.01	5.237±0.010
7–6 R101	2146.363	30543	3.94±0.07	0.653±0.012
8–7 P 71	1625.476	23491	4.40±0.03	1.828±0.011

Table 3—Continued

Transition	$\omega_0$ (cm $^{-1}$ )	$E_{\text{lower}}$ (cm $^{-1}$ )	FWHM (km s $^{-1}$ )	$W_\omega$ (10 $^{-3}$ cm $^{-1}$ )
8–7 P 66	1653.678	22289	4.41±0.02	2.321±0.010
8–7 P 15	1901.762	14880	4.78±0.01	5.302±0.011
8–7 P 8	1929.586	14578	4.48±0.01	3.991±0.013
8–7 R 5	1980.214	14503	4.39±0.01	3.600±0.013
8–7 R 6	1983.566	14524	4.44±0.01	3.992±0.013
8–7 R 61	2108.392	21169	4.59±0.01	4.971±0.007
9–8 P 22	1847.119	17308	4.59±0.01	4.192±0.010
9–8 R 9	1967.073	16568	4.40±0.02	3.451±0.015
9–8 R 23	2008.100	17390	4.72±0.01	5.382±0.011
9–8 R 66	2085.165	24171	4.37±0.01	3.005±0.009
9–8 R 75	2091.185	26370	4.19±0.03	1.933±0.016
10–9 P 66	1606.423	26027	4.25±0.05	1.035±0.012
10–9 P 30	1787.007	19978	4.50±0.01	3.085±0.008
10–9 P 3	1896.769	18363	4.11±0.04	0.834±0.008
10–9 R 38	2016.404	20944	4.45±0.02	3.909±0.014
2–0 P 41	4046.692	3292	4.14±0.02	3.006±0.012
2–0 P 25	4143.315	1247	4.46±0.01	4.323±0.007
2–0 P 9	4222.954	172	4.10±0.03	2.297±0.020
2–0 P 1	4256.217	3	4.00±0.13	0.306±0.010
2–0 R 2	4271.177	11	3.99±0.16	0.845±0.036
2–0 R 20	4324.410	806	4.27±0.01	5.224±0.014
2–0 R 81	4323.688	12501	4.52±0.06	0.919±0.013
3–1 P 60	3859.911	9033	4.09±0.03	1.959±0.015
3–1 P 38	4014.514	4953	4.23±0.01	4.821±0.009
3–1 P 19	4122.974	2866	4.33±0.01	6.858±0.010

Table 3—Continued

Transition	$\omega_0$ (cm $^{-1}$ )	$E_{\text{lower}}$ (cm $^{-1}$ )	FWHM (km s $^{-1}$ )	$W_\omega$ (10 $^{-3}$ cm $^{-1}$ )
3–1 P 2	4199.478	2154	4.32±0.05	1.048±0.012
3–1 R 20	4270.782	2942	4.27±0.01	7.278±0.016
3–1 R 59	4302.391	8810	4.17±0.02	4.609±0.020
3–1 R 65	4296.835	10203	4.28±0.01	3.857±0.009
3–1 R 80	4270.324	14232	3.87±0.05	1.322±0.016
3–1 R 93	4232.443	18332	4.78±0.08	0.619±0.011
4–2 P 76	3678.606	15097	4.70±0.08	0.828±0.015
4–2 P 58	3824.488	10647	4.17±0.03	2.313±0.015
4–2 P 13	4099.925	4603	4.20±0.01	4.397±0.012
4–2 P 1	4150.632	4263	3.66±0.11	0.403±0.013
4–2 R 36	4243.636	6763	4.36±0.00	8.403±0.007
4–2 R 61	4245.925	11311	4.26±0.02	4.578±0.021
4–2 R 63	4244.002	11771	4.27±0.01	4.154±0.014
4–2 R 72	4231.403	14012	4.20±0.02	2.584±0.010
4–2 R 83	4207.105	17124	4.15±0.05	1.274±0.017
4–2 R 95	4169.200	20969	4.12±0.12	0.495±0.016
5–3 P 73	3654.208	16274	4.23±0.06	0.844±0.013
5–3 P 1	4098.043	6354	4.19±0.12	0.413±0.012
5–3 R 3	4116.042	6372	4.30±0.03	1.664±0.011
5–3 R 5	4122.749	6406	4.17±0.03	2.318±0.018
5–3 R 6	4125.995	6428	4.19±0.01	2.741±0.009
5–3 R 68	4182.763	14990	4.25±0.01	2.920±0.010
5–3 R 74	4172.463	16541	4.30±0.04	2.092±0.018
6–4 R 3	4063.418	8436	4.05±0.06	1.193±0.019
6–4 R 4	4066.772	8451	4.31±0.04	1.595±0.015

Table 3—Continued

Transition	$\omega_0$ (cm $^{-1}$ )	$E_{\text{lower}}$ (cm $^{-1}$ )	FWHM (km s $^{-1}$ )	$W_\omega$ (10 $^{-3}$ cm $^{-1}$ )
6–4 R 7	4076.408	8518	4.32±0.02	2.639±0.011
6–4 R 75	4115.314	18775	4.23±0.03	1.605±0.012
7–5 R 20	4057.639	11221	4.25±0.01	4.052±0.013
7–5 R 76	4058.158	20982	4.19±0.08	1.116±0.024
8–6 R 70	4015.183	21346	4.19±0.03	1.221±0.008

Note. — Line center frequencies,  $\omega_0$ , and lower level energies,  $E_{\text{lower}}$ , are from Goorvitch (1994). Uncertainties on the Gaussian fit parameters (full width at half maximum absorption, FWHM, and the equivalent width,  $W_\omega$ ) are  $\pm 1\sigma$ , based on Lenz & Ayres (1992); the photometric noise was estimated by the dispersion of intensities about the empirically fitted Gaussian lineshape.

Table 4. Model- and Parameter-Dependent Oxygen Abundances

Model (1)	Components (2)	Cont	CO	CO	$(\epsilon_O)_0 \pm \sigma$ ( $\Delta$ )			$\langle \epsilon_O \rangle \pm \sigma$	
		c-l (3)	$\mu = 1$ (4)	c-l (5)	$\Delta v = 1, 2$ (6)	$\Delta v = 1$ (7)	$\Delta v = 2$ (8)	$\Delta v = 1$ (9)	$\Delta v = 2$ (10)
FAL C	1	4	3	0	820 $\pm$ 16 (-5.6)	809 $\pm$ 15 (-4.9)	824 $\pm$ 14 (-6.2)	731 $\pm$ 37	780 $\pm$ 44
Asplund	1	1	5	0	575 $\pm$ 13 (-2.9)	566 $\pm$ 14 (-2.3)	579 $\pm$ 11 (-3.1)	540 $\pm$ 18	565 $\pm$ 24
Asplund/HR96 <i>gf</i>	1	1	5	0	585 $\pm$ 16 (-4.2)	558 $\pm$ 14 (-2.4)	594 $\pm$ 10 (-4.0)	531 $\pm$ 18	575 $\pm$ 26
Asplund*5	5 $\Delta T$	1	5	0	496 $\pm$ 12 (+1.7)	530 $\pm$ 9 (-1.1)	490 $\pm$ 11 (+1.5)	520 $\pm$ 18	499 $\pm$ 19
COmosphere	1	4	5	4	846 $\pm$ 18 (-5.5)	871 $\pm$ 14 (-6.4)	848 $\pm$ 15 (-6.6)	762 $\pm$ 43	798 $\pm$ 47
COmosphere/HR96 <i>gf</i>	1	4	5	4	864 $\pm$ 14 (-6.8)	858 $\pm$ 14 (-6.4)	870 $\pm$ 15 (-7.5)	749 $\pm$ 42	812 $\pm$ 52
COmosphere*6	5 $\Delta T + 1$ NW	4	5	4	851 $\pm$ 20 (-5.1)	901 $\pm$ 13 (-6.9)	853 $\pm$ 13 (-6.8)	777 $\pm$ 47	803 $\pm$ 48
COmosphere $D_0 - 0.10$	1	4	5	4	939 $\pm$ 19 (-5.4)	966 $\pm$ 15 (-6.2)	939 $\pm$ 15 (-6.5)	846 $\pm$ 47	887 $\pm$ 51
COmosphere $D_0 + 0.10$	1	4	5	4	764 $\pm$ 16 (-5.5)	787 $\pm$ 13 (-6.5)	764 $\pm$ 12 (-6.7)	686 $\pm$ 39	720 $\pm$ 43
COmosphere $D_0 + 0.64$	1	4	5	4	451 $\pm$ 10 (-5.9)	465 $\pm$ 8 (-6.8)	453 $\pm$ 8 (-7.4)	403 $\pm$ 26	423 $\pm$ 28
COmosphere $H^- f - f \div 1.1$	1	4	5	4	831 $\pm$ 15 (-6.1)	837 $\pm$ 15 (-6.2)	833 $\pm$ 15 (-6.7)	734 $\pm$ 40	784 $\pm$ 46
COmosphere $H^- f - f \times 1.1$	1	4	5	4	860 $\pm$ 21 (-4.7)	913 $\pm$ 13 (-6.7)	862 $\pm$ 13 (-6.5)	791 $\pm$ 47	813 $\pm$ 47
COmosphere $H^- \div 1.1$	1	4	5	4	802 $\pm$ 17 (-5.5)	825 $\pm$ 13 (-6.3)	804 $\pm$ 14 (-6.6)	722 $\pm$ 40	757 $\pm$ 44
COmosphere $H^- \times 1.1$	1	4	5	4	893 $\pm$ 19 (-5.5)	920 $\pm$ 14 (-6.4)	892 $\pm$ 14 (-6.6)	804 $\pm$ 45	842 $\pm$ 49
COmosphere $\xi - 0.5$	1	4	5	4	848 $\pm$ 20 (-5.1)	903 $\pm$ 13 (-7.1)	848 $\pm$ 13 (-6.7)	777 $\pm$ 51	799 $\pm$ 47
COmosphere $\xi + 0.5$	1	4	5	4	837 $\pm$ 19 (-5.7)	816 $\pm$ 19 (-4.7)	845 $\pm$ 15 (-6.4)	741 $\pm$ 35	797 $\pm$ 46
COmosphere $T_{\min} - 200$	1	4	4	2	840 $\pm$ 16 (-5.1)	858 $\pm$ 12 (-5.8)	840 $\pm$ 13 (-6.2)	759 $\pm$ 39	795 $\pm$ 45
COmosphere $T_{\min} + 200$	1	4	4	2	852 $\pm$ 18 (-5.6)	878 $\pm$ 14 (-6.5)	855 $\pm$ 15 (-7.0)	766 $\pm$ 47	802 $\pm$ 49
COmosphere $T_{\text{outer}} - 200$	1	4	3	4	742 $\pm$ 19 (-4.1)	709 $\pm$ 17 (-2.4)	751 $\pm$ 12 (-4.1)	676 $\pm$ 23	727 $\pm$ 33
COmosphere $T_{\text{outer}} + 200$	1	4	3	4	928 $\pm$ 31 (-6.0)	1036 $\pm$ 20 (-9.4)	928 $\pm$ 16 (-8.3)	845 $\pm$ 70	860 $\pm$ 59
COmosphere-200	1	1	3	4	472 $\pm$ 14 (-0.7)	451 $\pm$ 13 (+1.1)	479 $\pm$ 9 (-0.4)	460 $\pm$ 15	479 $\pm$ 17

Table 4—Continued

Model	Components	Cont	CO		$(\epsilon_O)_0 \pm \sigma$				$\langle \epsilon_O \rangle \pm \sigma$	
		c-l	$\mu = 1$	c-l	$\Delta v = 1, 2$	$\Delta v = 1$	$\Delta v = 2$	$\Delta v = 1$	$\Delta v = 2$	
(1)	(2)	(3)	(4)	(5)	(6)	(7)	(8)	(9)	(10)	
Double Dip	1	5	5	5	654 $\pm$ 26 (−3.4)	599 $\pm$ 22 (−0.1)	663 $\pm$ 12 (−2.1)	598 $\pm$ 22	653 $\pm$ 26	
Double Dip*6	5 $\Delta T + 1$ NW	5	5	5	685 $\pm$ 24 (−3.6)	641 $\pm$ 21 (−1.1)	693 $\pm$ 13 (−2.5)	627 $\pm$ 21	680 $\pm$ 27	

Note. — Columns 3 (continuum center-limb behavior), 4 (CO  $\Delta v = 1$  core depths at disk center), and 5 (CO  $\Delta v = 1$  center-limb behavior) grade the success of the model in reproducing the particular observational constraint, on a scale of 0 (poor) to 5 (very good). In columns 6–8 the cited uncertainties are standard deviations about the linear fit to the  $\epsilon_O$ – $E_{\text{lower}}$  relation, with mild filtering to discard outliers. In columns 9 and 10, the uncertainties are the  $1\sigma$  dispersions in each 40-member abundance sample, with no filtering and not accounting for a possible correlation between  $\epsilon_O$  and  $E_{\text{lower}}$ .

Table 5. The Double Dip Model

$\log m$ (gr cm $^{-2}$ )	$\log \tau_{0.5}$	$z$ (km)	$T$ (K)
-4.00	-5.14	-1264	6527
-3.80	-4.94	-1189	6377
-3.60	-4.81	-1116	6233
-3.40	-4.71	-1046	6015
-3.20	-4.67	-983	4776
-3.00	-4.66	-935	3750
-2.80	-4.64	-894	3445
-2.60	-4.61	-854	3400
-2.40	-4.56	-814	3531
-2.20	-4.47	-771	3967
-2.00	-4.36	-722	4385
-1.80	-4.19	-671	4450
-1.60	-3.97	-620	4473
-1.40	-3.68	-568	4496
-1.20	-3.37	-517	4520
-1.00	-3.03	-464	4546
-0.90	-2.86	-438	4571
-0.80	-2.69	-412	4584
-0.70	-2.51	-386	4560
-0.60	-2.33	-360	4514
-0.50	-2.15	-334	4499
-0.40	-1.98	-308	4557
-0.30	-1.80	-281	4678
-0.20	-1.63	-254	4810
-0.10	-1.45	-226	4909

Table 5—Continued

$\log m$ (gr cm $^{-2}$ )	$\log \tau_{0.5}$	$z$ (km)	$T$ (K)
0.00	-1.28	-198	4984
+0.05	-1.19	-184	5024
+0.10	-1.10	-169	5074
+0.15	-1.01	-155	5135
+0.20	-0.92	-140	5203
+0.25	-0.83	-125	5282
+0.30	-0.74	-110	5372
+0.35	-0.65	-94	5477
+0.40	-0.56	-78	5595
+0.45	-0.46	-62	5728
+0.50	-0.35	-46	5864
+0.55	-0.23	-29	6029
+0.60	-0.10	-11	6242
+0.65	+0.06	+7	6580
+0.70	+0.29	+26	7186
+0.75	+0.62	+48	7973
+0.80	+1.00	+72	8633
+0.85	+1.33	+97	8991

Table 6. CO Isotopomer Equivalent Widths

Transition	Isotopomer	$\omega_0$ (cm $^{-1}$ )	$E_{\text{lower}}$ (cm $^{-1}$ )	FWHM (km s $^{-1}$ )	$W_\omega$ (10 $^{-3}$ cm $^{-1}$ )
1-0 P65	$^{13}\text{C}^{16}\text{O}$	1795.191	7782	4.05	0.435 $\pm$ 0.011
1-0 P62		1811.598	7094	4.05	0.540 $\pm$ 0.013
1-0 P10		2057.857	202	4.05	1.165 $\pm$ 0.004
1-0 R14		2147.205	385	4.05	1.809 $\pm$ 0.011
1-0 R42		2221.409	3301	4.05	2.057 $\pm$ 0.012
1-0 R64		2258.716	7549	4.05	0.979 $\pm$ 0.011
1-0 R76		2270.724	10565	4.05	0.518 $\pm$ 0.016
1-0 R81		2273.917	11962	4.05	0.365 $\pm$ 0.012
2-1 P52		1841.059	7074	4.05	0.960 $\pm$ 0.009
2-1 P30		1947.828	3785	4.05	1.669 $\pm$ 0.014
2-1 P12		2024.913	2380	4.05	1.212 $\pm$ 0.016
2-1 R13		2118.261	2427	4.05	1.632 $\pm$ 0.014
2-1 R18		2133.604	2718	4.05	2.047 $\pm$ 0.010
2-1 R82		2246.386	14236	4.05	0.314 $\pm$ 0.007
2-1 R83		2246.817	14526	4.05	0.331 $\pm$ 0.007
3-2 P67		1737.948	12275	4.05	0.346 $\pm$ 0.013
3-2 R 5		2066.470	4220	4.05	0.604 $\pm$ 0.011
3-2 R21		2116.416	4999	4.05	1.653 $\pm$ 0.010
3-2 R36		2154.960	6561	4.05	1.710 $\pm$ 0.011
3-2 R37		2157.233	6693	4.05	1.764 $\pm$ 0.009
3-2 R81		2217.967	15911	4.05	0.278 $\pm$ 0.013
4-3 P17		1955.148	6759	4.05	0.815 $\pm$ 0.009
4-3 P 7		1994.585	6312	4.05	0.429 $\pm$ 0.010
4-3 P 6		1998.356	6287	4.05	0.384 $\pm$ 0.011
4-3 R36		2128.561	8585	4.05	1.226 $\pm$ 0.007

Table 6—Continued

Transition	Isotopomer	$\omega_0$ (cm $^{-1}$ )	$E_{\text{lower}}$ (cm $^{-1}$ )	FWHM (km s $^{-1}$ )	$W_\omega$ (10 $^{-3}$ cm $^{-1}$ )
4–3 R37		2130.802	8716	4.05	1.244±0.006
4–3 R43		2143.447	9576	4.05	1.105±0.016
5–4 P57		1745.031	14031	4.05	0.272±0.012
6–5 P45		1781.720	13839	4.05	0.301±0.010
6–5 P38		1814.887	12818	4.05	0.325±0.016
6–5 P31		1846.698	11964	4.05	0.372±0.011
6–5 R11		2009.683	10459	4.05	0.339±0.008
6–5 R27		2054.702	11552	4.05	0.530±0.007
6–5 R35		2073.746	12431	4.05	0.517±0.009
7–6 R20	$^{13}\text{C}^{16}\text{O}$	2010.445	12927	4.05	0.292±0.007
1–0 P13	$^{12}\text{C}^{17}\text{O}$	2064.996	340	4.05	0.111±0.012
1–0 R22		2192.917	946	4.05	0.174±0.010
1–0 R33		2222.770	2095	4.05	0.090±0.017
2–1 P34		1946.217	4318	4.05	0.089±0.008
2–1 R37		2205.393	4715	4.05	0.078±0.010
3–2 R39		2182.856	7063	4.05	0.081±0.012
3–2 R45	$^{12}\text{C}^{17}\text{O}$	2195.376	7991	4.05	0.102±0.006
1–0 P57	$^{12}\text{C}^{18}\text{O}$	1835.568	5992	4.05	0.191±0.008
1–0 P43		1907.045	3444	4.05	0.282±0.009
1–0 P35		1945.548	2298	4.05	0.330±0.008
1–0 P27		1982.267	1381	4.05	0.372±0.007
1–0 P18		2021.359	625	4.05	0.303±0.013
1–0 P11		2050.081	241	4.05	0.222±0.009
1–0 R11		2133.490	241	4.05	0.299±0.006

Table 6—Continued

Transition	Isotopomer	$\omega_0$ (cm $^{-1}$ )	$E_{\text{lower}}$ (cm $^{-1}$ )	FWHM (km s $^{-1}$ )	$W_\omega$ (10 $^{-3}$ cm $^{-1}$ )
1–0 R26		2178.262	1282	4.05	0.500±0.010
1–0 R48		2229.106	4275	4.05	0.345±0.010
1–0 R49		2230.979	4452	4.05	0.345±0.009
1–0 R50		2232.813	4632	4.05	0.322±0.015
1–0 R63		2253.037	7292	4.05	0.196±0.008
2–1 P43		1883.226	5505	4.05	0.244±0.014
2–1 P31		1939.926	3886	4.05	0.348±0.010
2–1 P25		1966.756	3269	4.05	0.341±0.009
2–1 P17		2000.888	2646	4.05	0.322±0.007
3–2 R 7		2069.339	4259	4.05	0.126±0.006
3–2 R18		2103.755	4773	4.05	0.279±0.009
3–2 R29		2133.930	5719	4.05	0.317±0.010
3–2 R37		2153.111	6676	4.05	0.356±0.008
4–3 P42		1840.585	9401	4.05	0.140±0.008
4–3 P23		1926.712	7182	4.05	0.184±0.009
4–3 R10		2053.683	6396	4.05	0.131±0.008
4–3 R26		2100.159	7449	4.05	0.212±0.010
5–4 P31		1867.672	9963	4.05	0.132±0.009
5–4 R16	$^{12}\text{C}^{18}\text{O}$	2046.578	8697	4.05	0.099±0.006

Note. — Line center frequencies,  $\omega_0$ , and lower level energies,  $E_{\text{lower}}$ , are from Goorvitch (1994). Uncertainties on the Gaussian fit parameters (for the equivalent width  $W_\omega$ , only;  $\omega$  and FWHM were fixed) are  $\pm 1\sigma$ , based on Lenz & Ayres (1992), with empirical estimates of the photometric noise.

Table 7. Model-Dependent Carbon and Oxygen Isotopic Ratios

Model	$R \pm \sigma$ (s.e.) [ $\epsilon_O(\Delta v = 1, 2)$ ]			$R \pm \sigma$ (s.e.) [ $\epsilon_O(\Delta v = 1)$ ]		
	$^{12}\text{C}/^{13}\text{C}$	$^{16}\text{O}/^{17}\text{O}$	$^{16}\text{O}/^{18}\text{O}$	$^{12}\text{C}/^{13}\text{C}$	$^{16}\text{O}/^{17}\text{O}$	$^{16}\text{O}/^{18}\text{O}$
FAL C	$81.4 \pm 3.9$ (0.7)	$1806 \pm 620$ (234)	$451 \pm 32$ (7)	$80.7 \pm 3.8$ (0.6)	$1775 \pm 609$ (230)	$440 \pm 28$ (6)
Asplund	$81.8 \pm 3.9$ (0.7)	$1810 \pm 621$ (235)	$453 \pm 31$ (7)	$80.7 \pm 3.8$ (0.6)	$1771 \pm 606$ (229)	$443 \pm 31$ (7)
Asplund*5	$89.0 \pm 4.2$ (0.7)	$2022 \pm 684$ (258)	$506 \pm 35$ (7)	$94.7 \pm 3.3$ (0.6)	$2182 \pm 728$ (275)	$546 \pm 36$ (7)
COmosphere	$80.8 \pm 3.8$ (0.7)	$1790 \pm 613$ (232)	$448 \pm 31$ (6)	$83.9 \pm 3.7$ (0.6)	$1898 \pm 649$ (245)	$467 \pm 32$ (7)
COmosphere*6	[ $80.4 \pm 3.6$ (0.6)]	[ $1726 \pm 592$ (224)]	[ $441 \pm 28$ (6)]	$86.3 \pm 3.4$ (0.6)	$1923 \pm 651$ (246)	$482 \pm 33$ (7)
COmosphere-200	$83.3 \pm 3.3$ (0.6)	$1777 \pm 605$ (229)	$458 \pm 31$ (6)	$78.8 \pm 4.0$ (0.7)	$1680 \pm 569$ (215)	$429 \pm 27$ (6)
Double Dip	$85.4 \pm 3.0$ (0.5)	$1901 \pm 645$ (244)	$473 \pm 30$ (6)	$77.0 \pm 4.3$ (0.7)	$1667 \pm 568$ (215)	$421 \pm 29$ (6)
Double Dip*6	$85.5 \pm 2.9$ (0.5)	$1868 \pm 626$ (236)	$475 \pm 30$ (6)	[ $78.9 \pm 4.2$ (0.7)]	[ $1682 \pm 566$ (214)]	[ $436 \pm 29$ (6)]

 1  
5  
6

Note. — Favored isotopic ratios are enclosed in square brackets. Values in parentheses are standard errors of the mean.

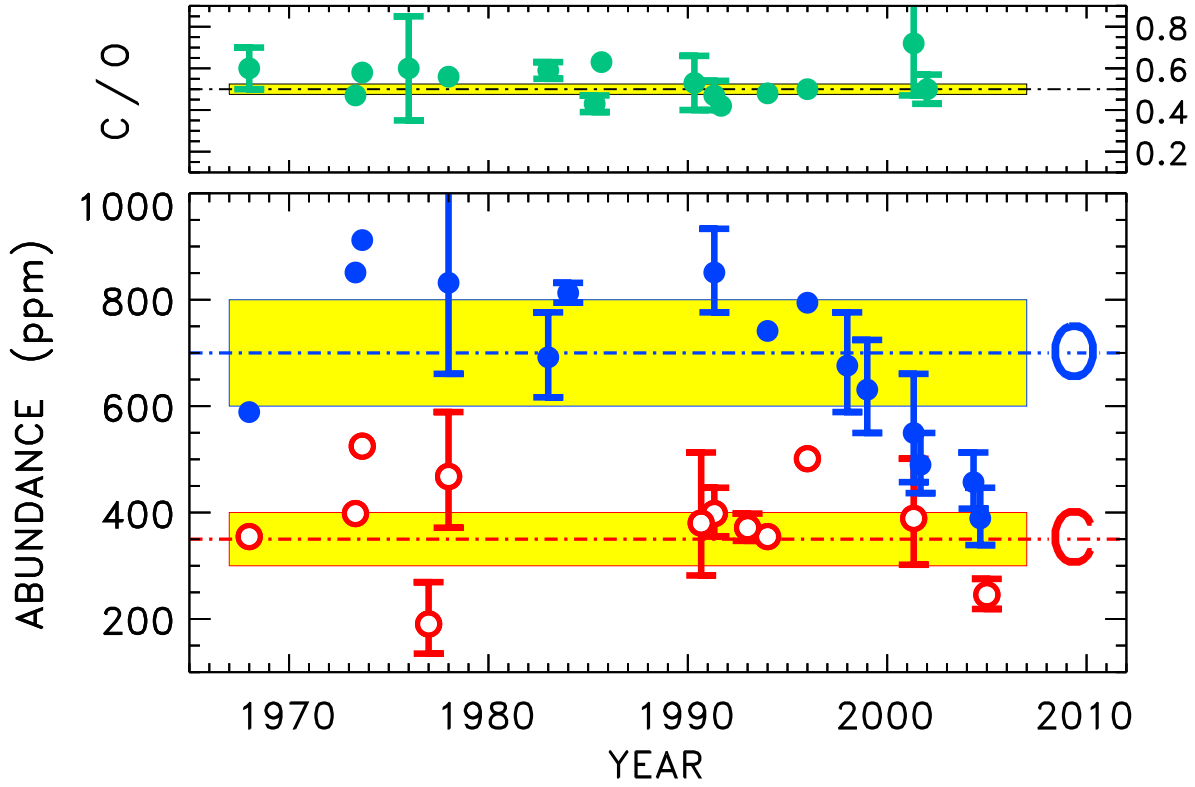


Fig. 1.— Solar abundances of oxygen (solid blue dots, lower panel) and carbon (red circles), and C/O ratio (green dots, upper panel), over time. Within past few years, reported solar  $\epsilon_{\text{O}}$  has fallen precipitously to historical level of the carbon abundance. Although recent measurements of solar carbon are fewer, it too has kept pace with drop in solar oxygen, maintaining a ratio of about 0.5. At recent rate of decline, Sun will run out of oxygen in around 2015. (Shaded bands indicate values recommended in present work.)

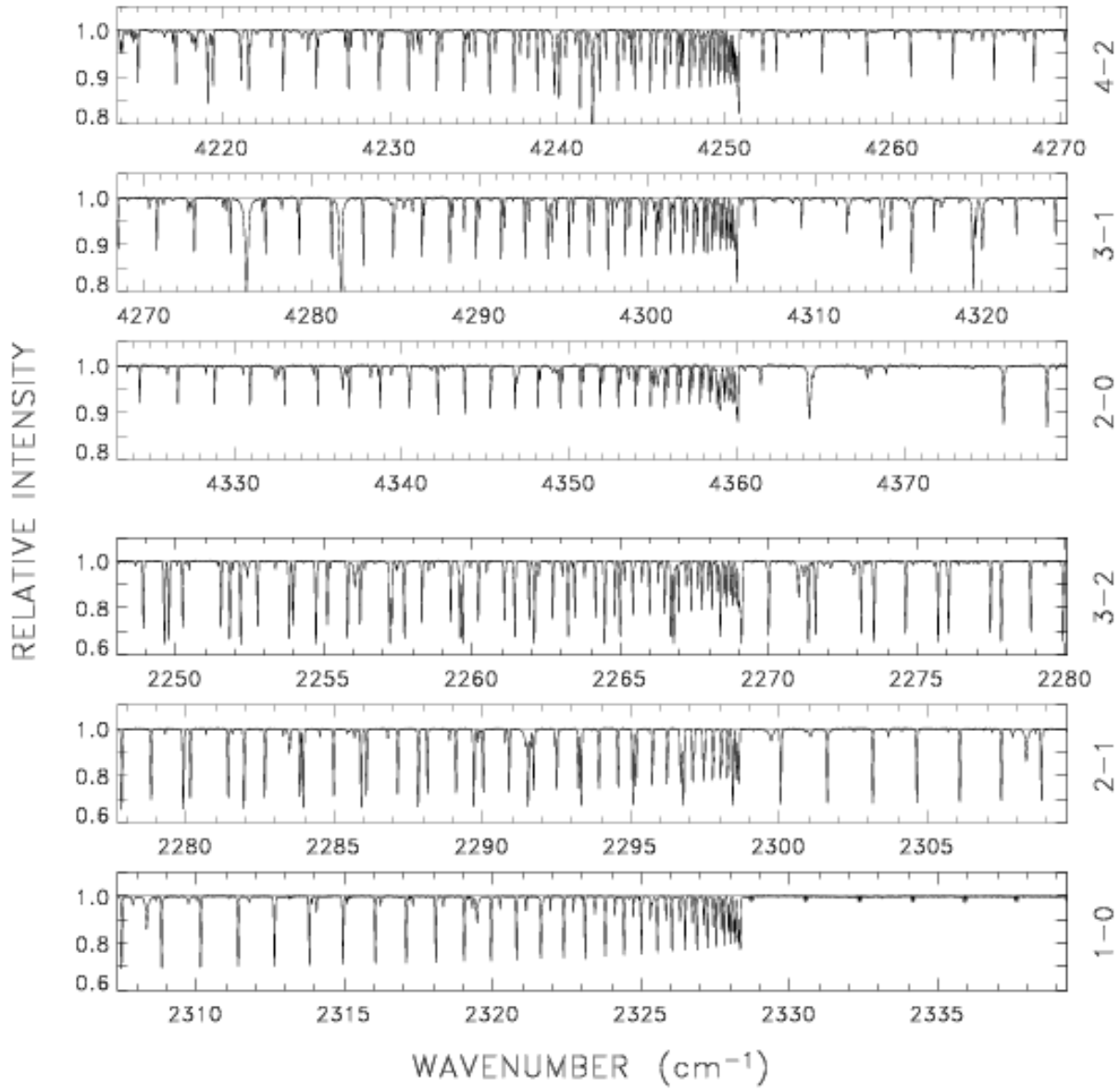


Fig. 2.— Representative intervals from ATMOS/ATLAS-3 solar infrared spectrum. Upper three panels depict heads of first overtone ( $\Delta v = 2$ ) 2–0, 3–1, and 4–2 bands; lower three panels depict heads of fundamental ( $\Delta v = 1$ ) 1–0, 2–1, and 3–2 bands. Most absorption features in these tracings are solar CO. (However, faint evenly spaced dips longward of 1–0 bandhead are due to residual water vapor in the instrument shroud, which was unable to fully outgas owing to a protective window.)

Fig. 3.— Representative transitions from 1–0 R-branch ( $\Delta v = +1$ ,  $\Delta J = +1$ ) of CO fundamental from the ATMOS spectra (dots). Simulated line profiles (red curves) were synthesized with an “optimum” thermal profile, to be described later. Note graduated relative intensity ordinates: values are scaled linearly between major tick marks. First interval above, and below, unit level is first  $\pm 1\%$ , emphasizing continuum and (photometric) scatter of points around it. Full range extends to 40% below unit line to show details of stronger features. Red ticks indicate line center ( $\omega_0$ , noted below each panel), and major ticks on abscissa are  $0.02 \text{ cm}^{-1}$  apart. Thick blue vertical ticks indicate  $^{12}\text{C}^{16}\text{O}$  blends; orange for blends with CO isotopomers, which—aside from a few moderate-strength  $^{13}\text{C}^{16}\text{O}$  transitions—usually are quite weak. Lowest excitation 1–0 lines ( $J \leq 10$ ) are strongly saturated in Earth’s atmosphere, and must be observed from space.

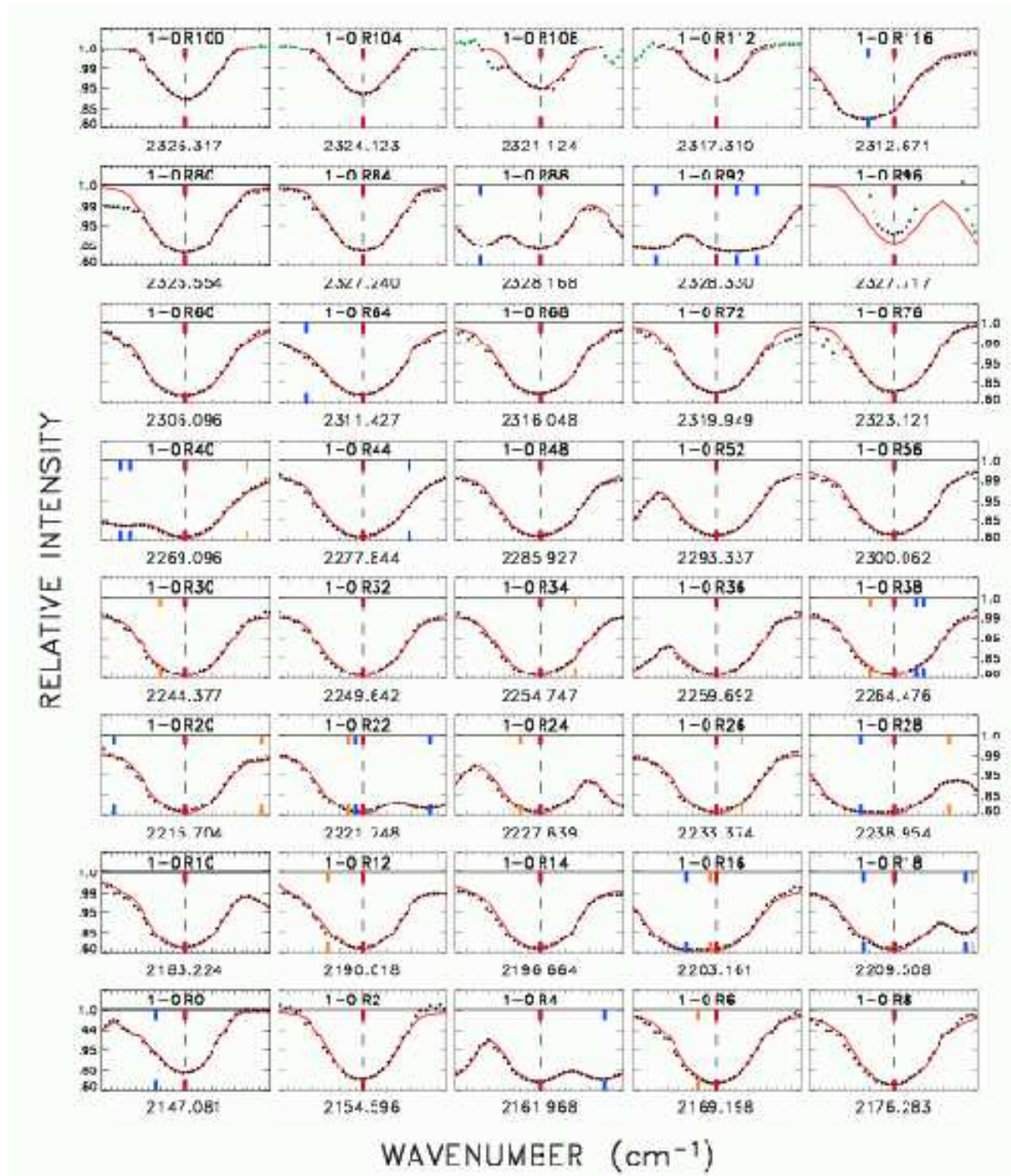


Fig. 3

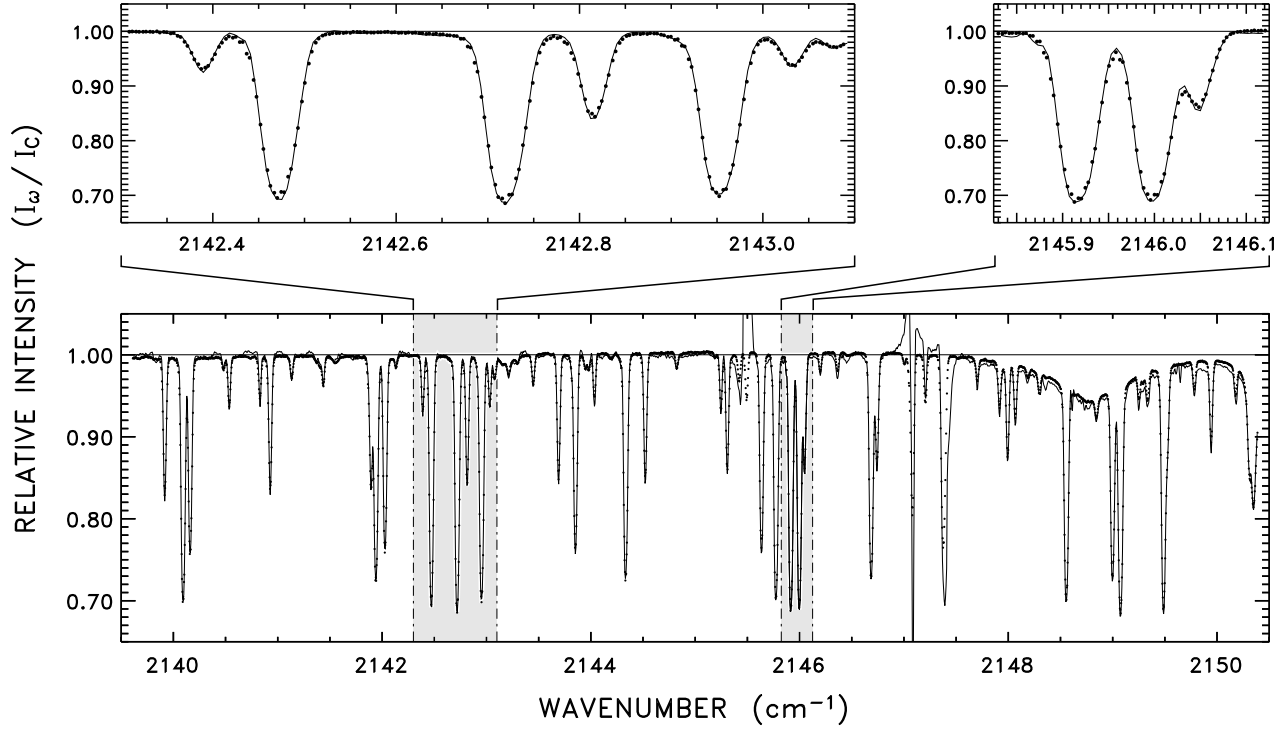


Fig. 4.— Comparison of disk center McMath-Pierce FTS scan (solid curve, corrected for terrestrial absorptions) and ATMOS/ATLAS-3 traces (dots) for  $2145 \text{ cm}^{-1}$  ( $4.66 \mu\text{m}$ ) region favored for groundbased observations of solar CO, owing to low contamination by telluric absorptions. Broad shallow dip at  $2149 \text{ cm}^{-1}$  is H I  $\text{Pf}\beta$ , but otherwise all other narrow absorptions are solar CO. In a few places (e.g.,  $2147 \text{ cm}^{-1}$ ), the groundbased FTS scan was affected by a large telluric absorption correction and is unreliable. ATMOS spectrum was obtained above Earth’s atmosphere and is largely free of such contamination. Upper panels are expanded views of two regions. Careful examination finds that Shuttle-borne FTS scans are very slightly lower in resolution than groundbased counterparts, although ATMOS resolution still is extremely high ( $R \sim 2 \times 10^5$ ), fully resolving the narrow CO absorptions.

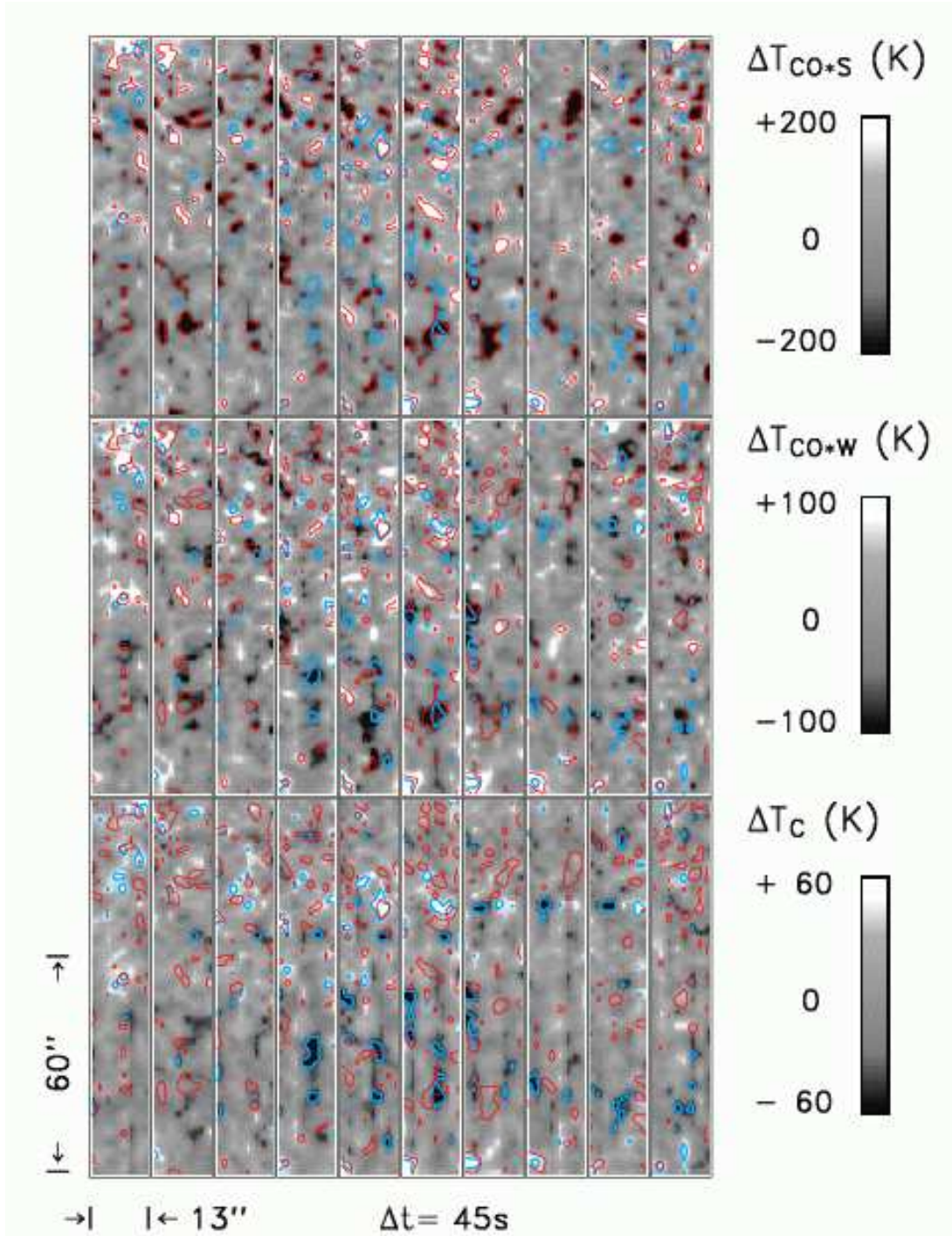


Fig. 5.— Time sequences of thermal maps recorded at disk center: sum of three strong CO lines (upper), sum of two weak CO lines (middle), and  $2145\text{ cm}^{-1}$  ( $4.66\text{ }\mu\text{m}$ ) continuum (lower). Cadence was 45 s per  $13''\times 97''$  field of view. Color bars on right indicate range of temperature fluctuations displayed in specific row. Contours outline patches of highest and lowest temperature fluctuations for the strong CO lines (red) and continuum (blue), and are repeated in each panel.

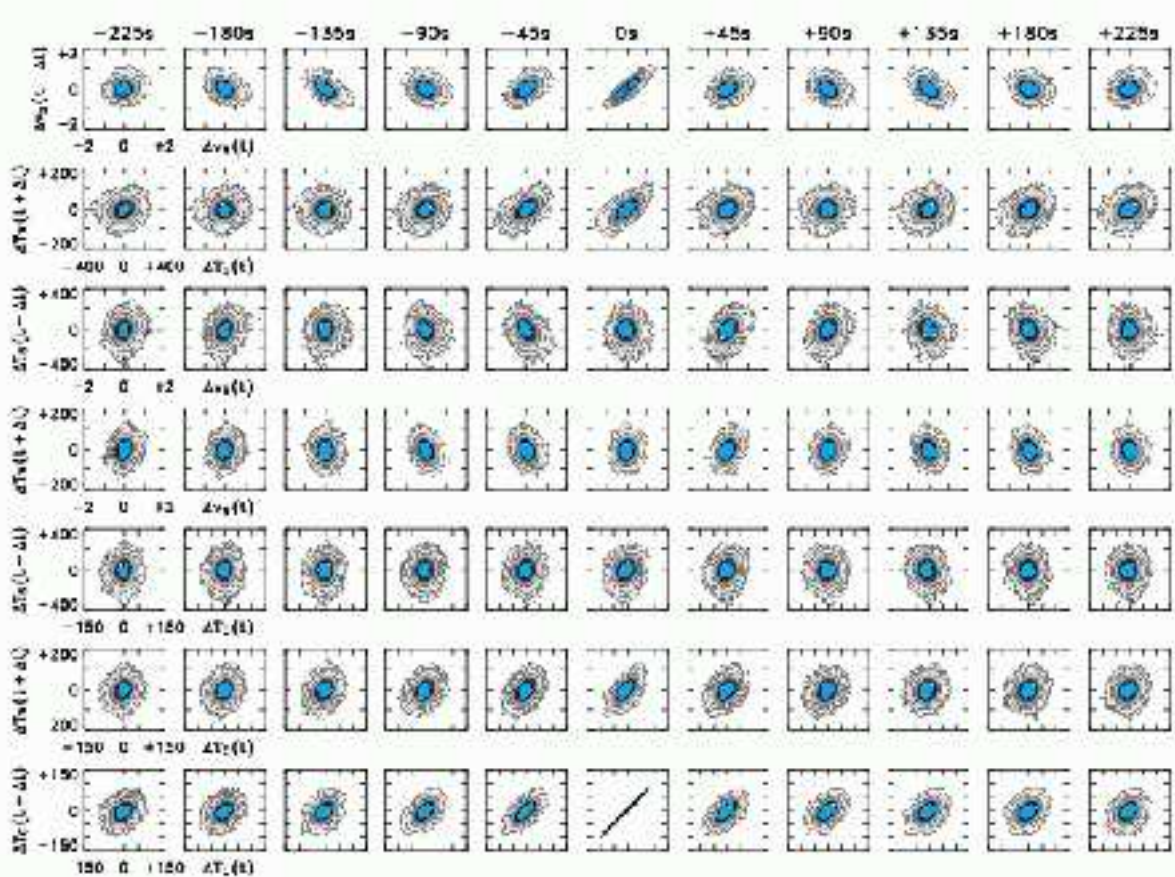


Fig. 6.— Cross-correlation diagrams comparing CO and  $2145\text{ cm}^{-1}$  continuum parameters for range of temporal lags. Subscript “S” indicates sum of three strong CO lines; “W” is for sum of two weaker features. Correlations are broadly consistent with domination of temperature and velocity fields by photospheric  $p$ -modes. Temperature fluctuation rms values are: 22 K (continuum); 42 K (weak CO line set), 83 K (strong CO line set). Doppler rms fluctuations are  $270\text{ m s}^{-1}$  (weak CO) and  $314\text{ m s}^{-1}$  (strong CO).

Fig. 7.— Schematic illustration of steps to derive calibrated disk center continuum intensities. Upper panel depicts conversion factor between disk average and disk center intensity (former is surface flux density  $\mathcal{F}_\lambda$  divided by  $\pi$ ). Smaller green dots in lower portion of panel are deviations of individual measurements from polynomial fit: horizontal dot-dashed lines are  $\pm 1\%$ . In middle panel, lighter curve (orange: left hand scale) is high dispersion residual flux spectrum smoothed to resolution of Thuillier et al. (2004) irradiances, while darker curve is Thuillier tracing adjusted from irradiance to surface flux (red: right hand scale). Larger dots are ratio of Thuillier to smoothed residual flux spectrum in places where smoothed trace exceeds 98% of running maximum. Curve through these points is a polynomial fit, utilizing a  $2\sigma$  filter to eliminate outliers (dark points), representing 100% continuum flux level. Bottom panel shows result of dividing continuum flux level by  $\mathcal{F}_\lambda/I_\lambda$  ( $\pi$  times upper panel) to obtain absolute specific intensities (thin solid curve), then multiplying by original residual flux spectrum (last step is purely for illustration).

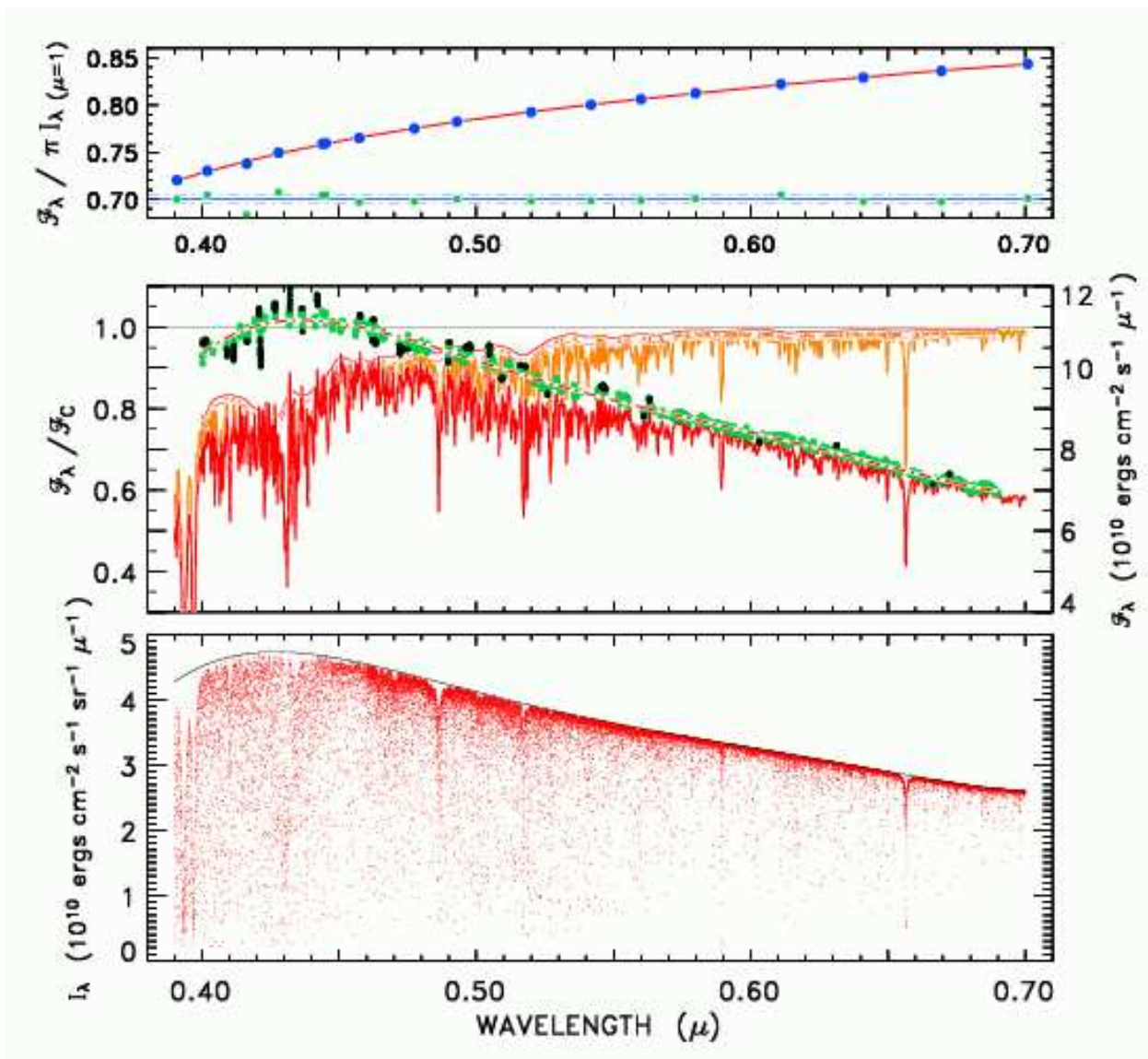


Fig. 7

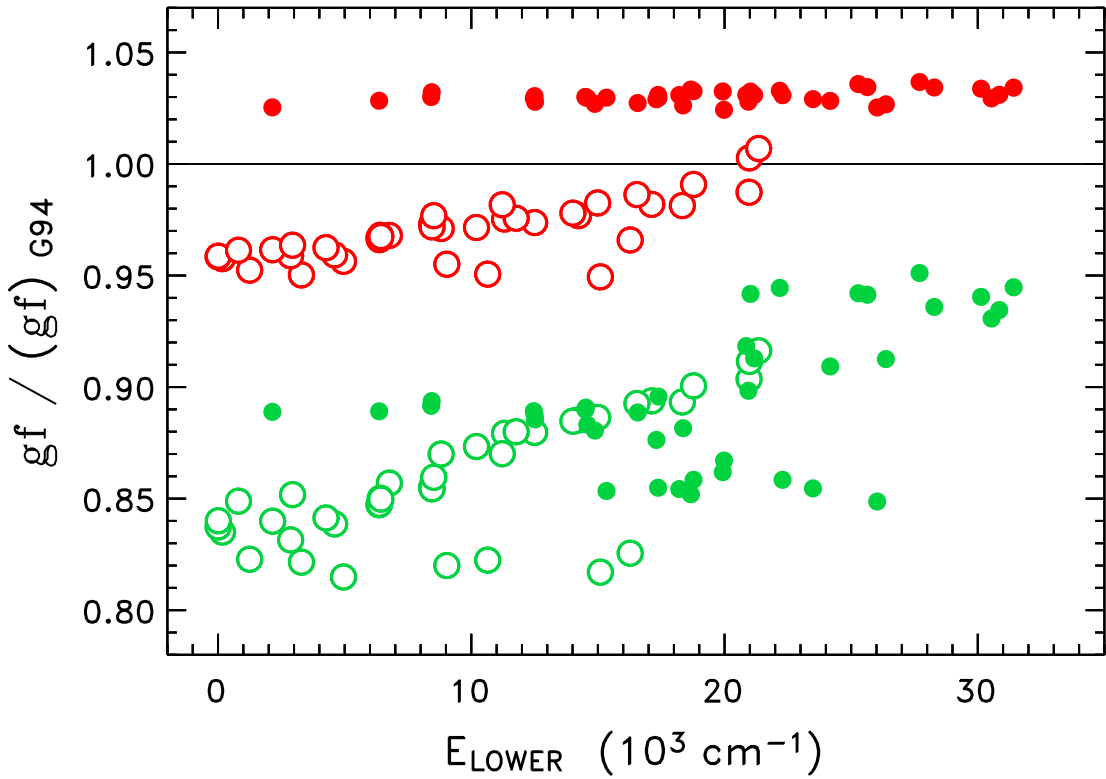


Fig. 8.— Comparison of CO  $\Delta V = 1, 2$  oscillator strengths versus lower state excitation energy. Goorvitch (1994) was used as reference, and relative behavior of Hure & Roueff (1996)  $gf$ -values are depicted as darker (red) dots ( $\Delta v = 1$ ) and open circles ( $\Delta v = 2$ ) in upper part of diagram. Specific points refer to CO abundance sample described in text: 40 lines from fundamental, 40 from first overtone. Lower, lighter (green) points are from earlier CO line strength compilation by Kirby-Docken & Liu (1978), again displayed relative to Goorvitch scale.

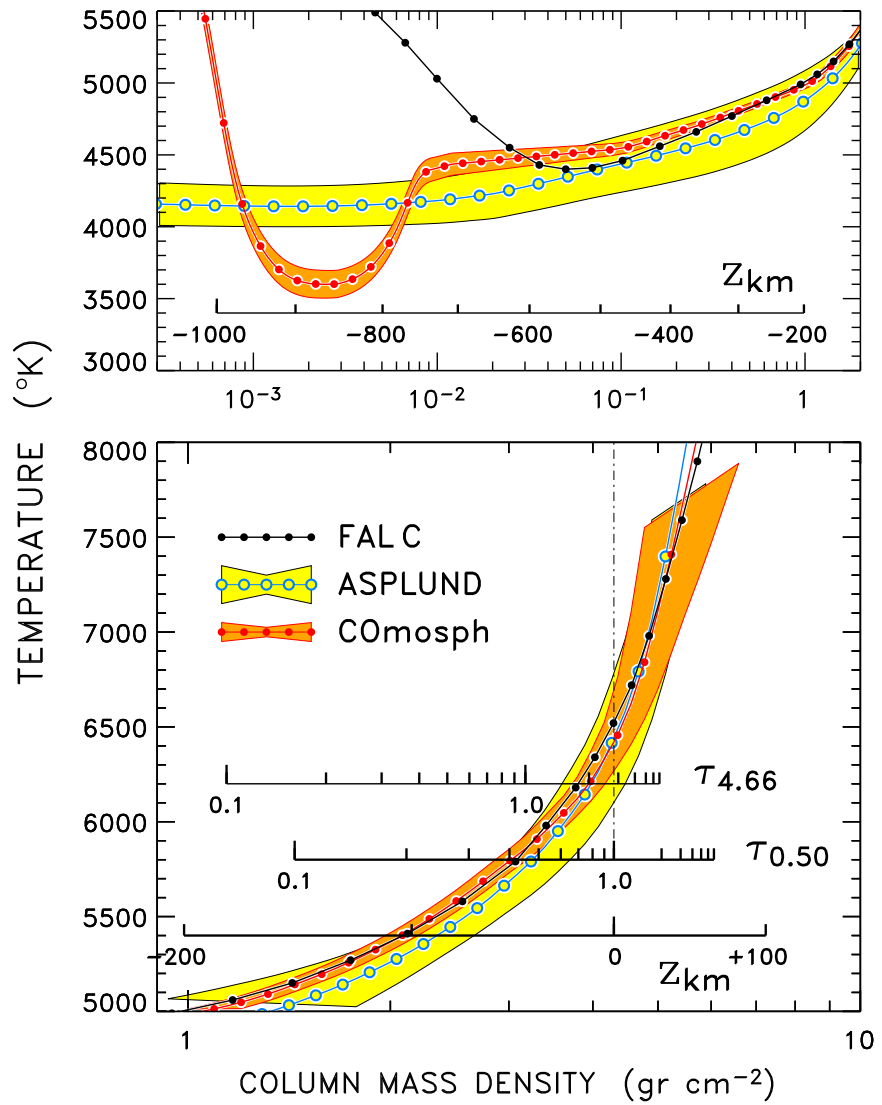


Fig. 9.— Photospheric thermal profiles considered in present study. Black dots refer to FALC semi-empirical model of Fontenla, Avrett, & Loeser (1993); larger, lighter (blue) dots to mean temperature distribution of Asplund et al. (2004) 3-D convection model; and medium (red) dots to our optimum “COmosphe.” Shading on latter two profiles indicate rms thermal excursions to capture heterogeneous nature of solar atmosphere at different levels. Asplund range is as reported by those authors for their *ab initio* model, and deeper part well matches continuum granulation contrasts measured at high spatial resolution in visible. Smaller COmosphe rms range at mid- and high altitudes was based on empirical measurements of thermal fluctuations observed in CO  $\Delta v = 1$  lines and 2145  $\text{cm}^{-1}$  (4.66  $\mu\text{m}$ ) continuum. COmosphe model was specifically adjusted to match visible continuum center-limb behavior, and empirical properties of CO  $\Delta v = 1$  spectrum. Optical depth and physical depth scales are for that model.

Fig. 10.— (a) Continuum properties of FALC model. Larger left hand panel depicts  $T(m)$  profile and contribution functions for continuum intensities at representative wavelengths (from right to left, 0.4–5  $\mu\text{m}$ ). Inset panel illustrates (enforced) fit to continuum highpoints: ordinate scale is in  $10^{10}$   $\text{ergs cm}^{-2} \text{s}^{-1} \text{ster}^{-1} \mu\text{m}^{-1}$ , and shaded bands indicate  $\pm 10\%$  (inner) and  $\pm 20\%$  (outer). Upper right hand panel compares observed (dots) and predicted relative intensity center-limb curves for representative wavelengths, from top to bottom (in  $\mu\text{m}$ ): 5.3, 2.5, 0.8, 0.5, 0.4. Lower right hand panel also depicts continuum center-limb behavior, but now expressed in brightness temperatures (to suppress Planck function bias) and calculated for larger sample of wavelengths: generally, thermal IR wavelengths are at top (in red), near red wavelengths toward bottom (orange), and visible in middle (green/blue). FALC reproduces empirical center-limb behavior very well in visible, although less well in thermal IR.

(b) Asplund mean temperature model. While somewhat hotter in deep photosphere than FALC, Asplund  $T(m)$  profile is noticeably cooler above  $m = 3 \text{ gr cm}^{-2}$ , which has a negative impact on center-limb behavior in visible, although thermal IR curves are well matched. However, the too steep predicted center-limb curves in visible indicate that the deep-photosphere temperature “calibration” will not be carried reliably out to higher layers where CO rovibrational bands form.

(c) 5 component (“1.5-D”) version of Asplund model, to investigate influence of thermally heterogeneous photosphere on continuum intensities and center-limb behavior. Thin curves depict predictions for individual thermal profiles, while heavier dot-dashed curves show averaged intensities. Here, rms intensity excursions in visible continuum are comparable to observed  $\sim 13\%$  at 0.5  $\mu\text{m}$ .

(d) 6 component version of “optimum” COmosphere model.

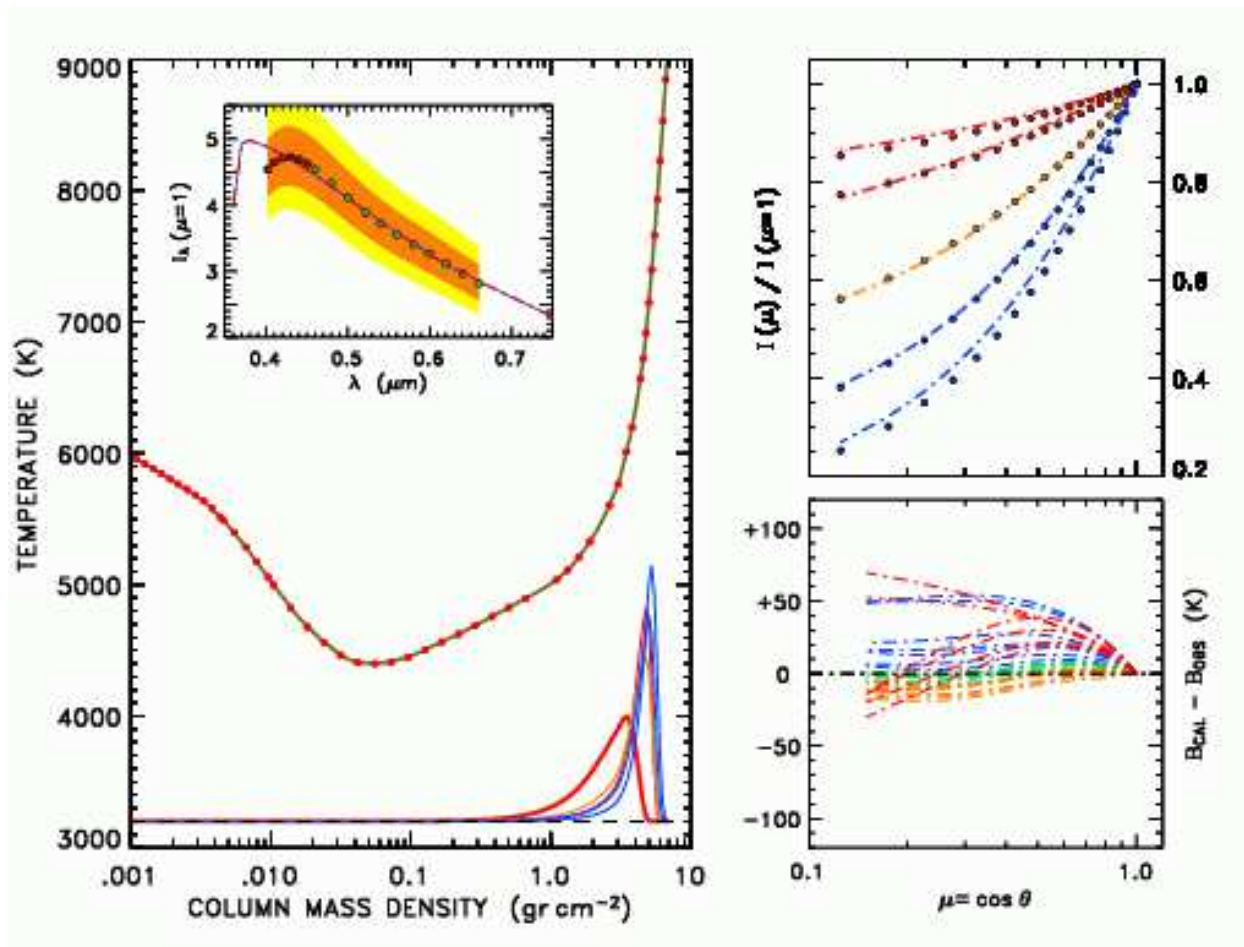


Fig. 10a

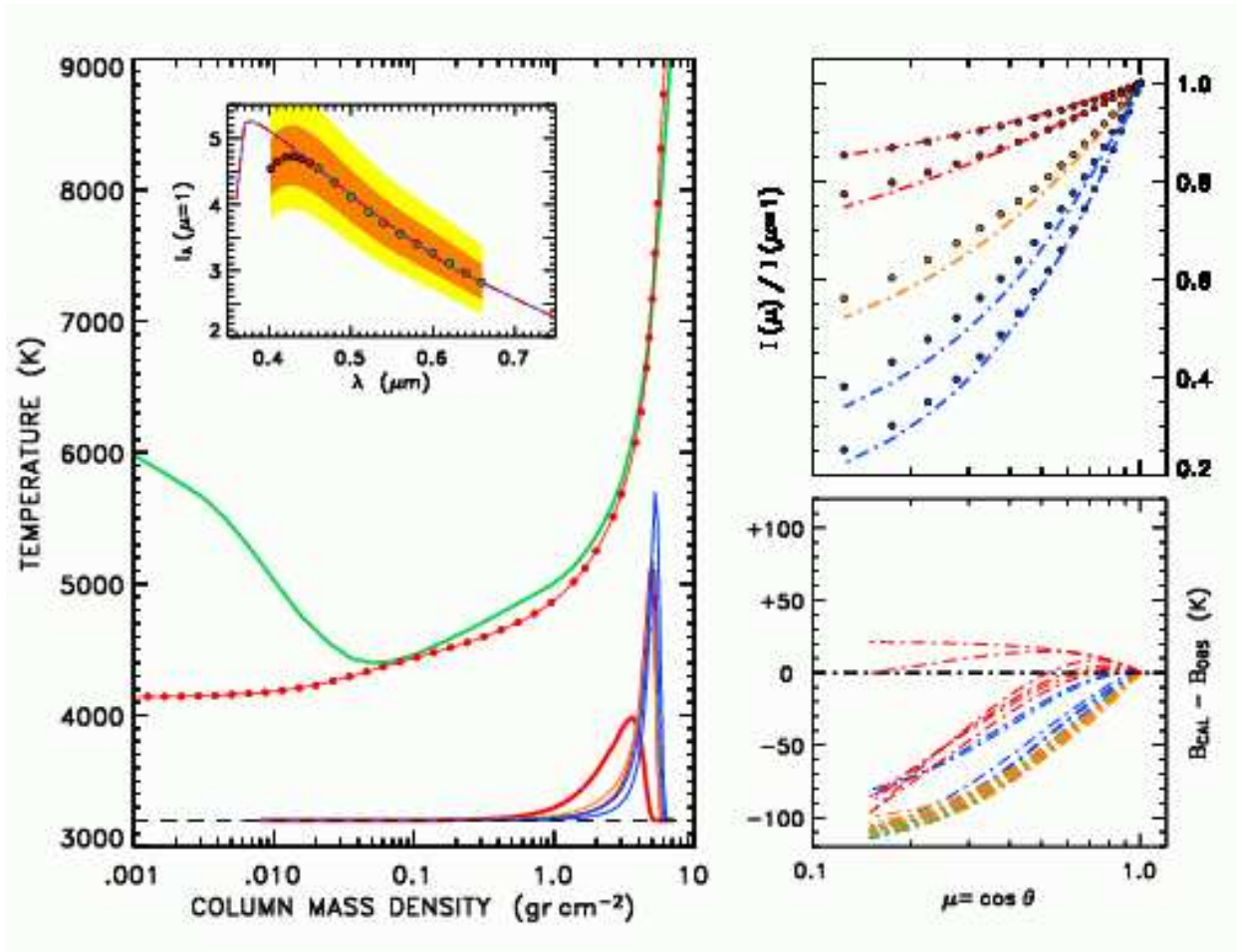


Fig. 10b

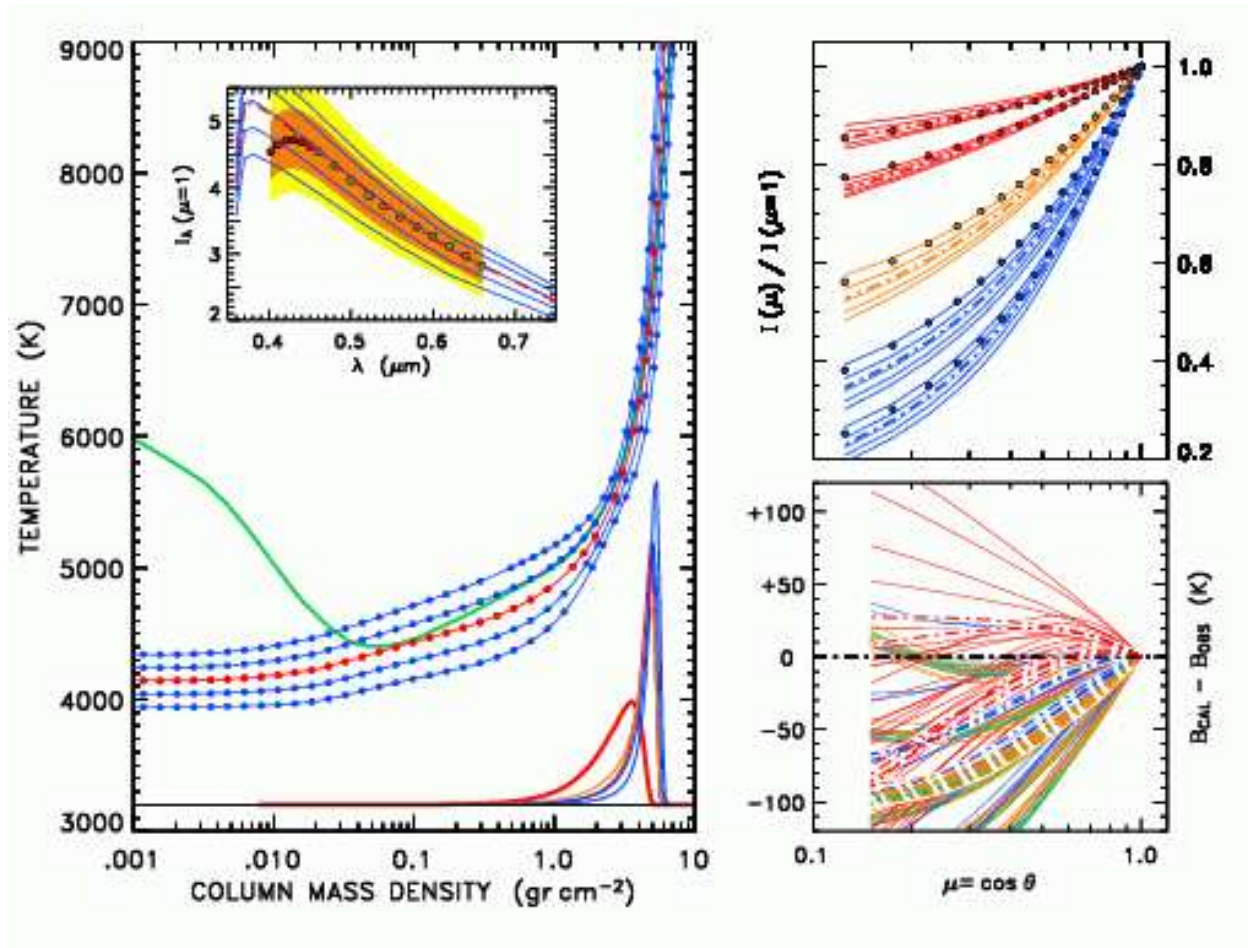


Fig. 10c

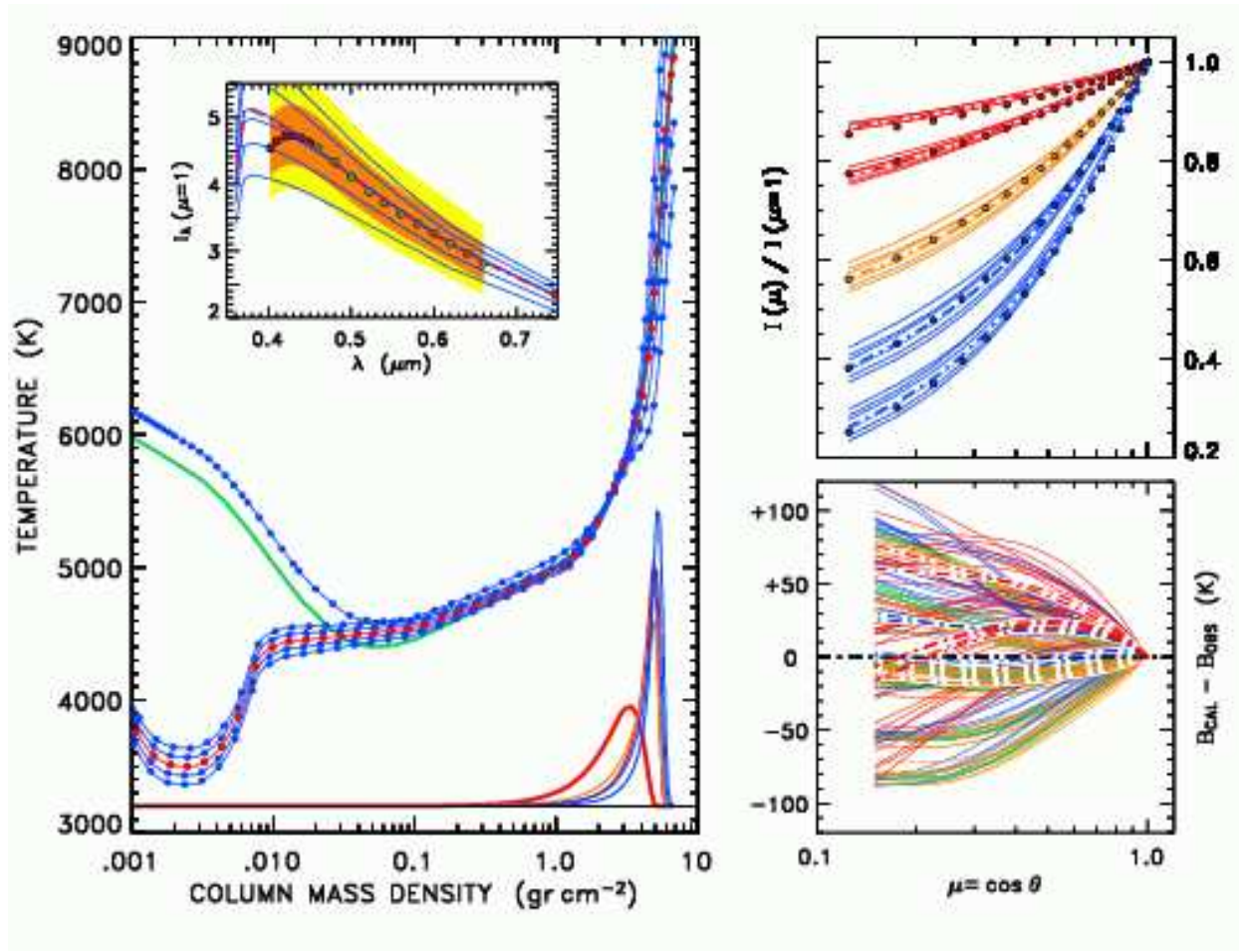


Fig. 10d

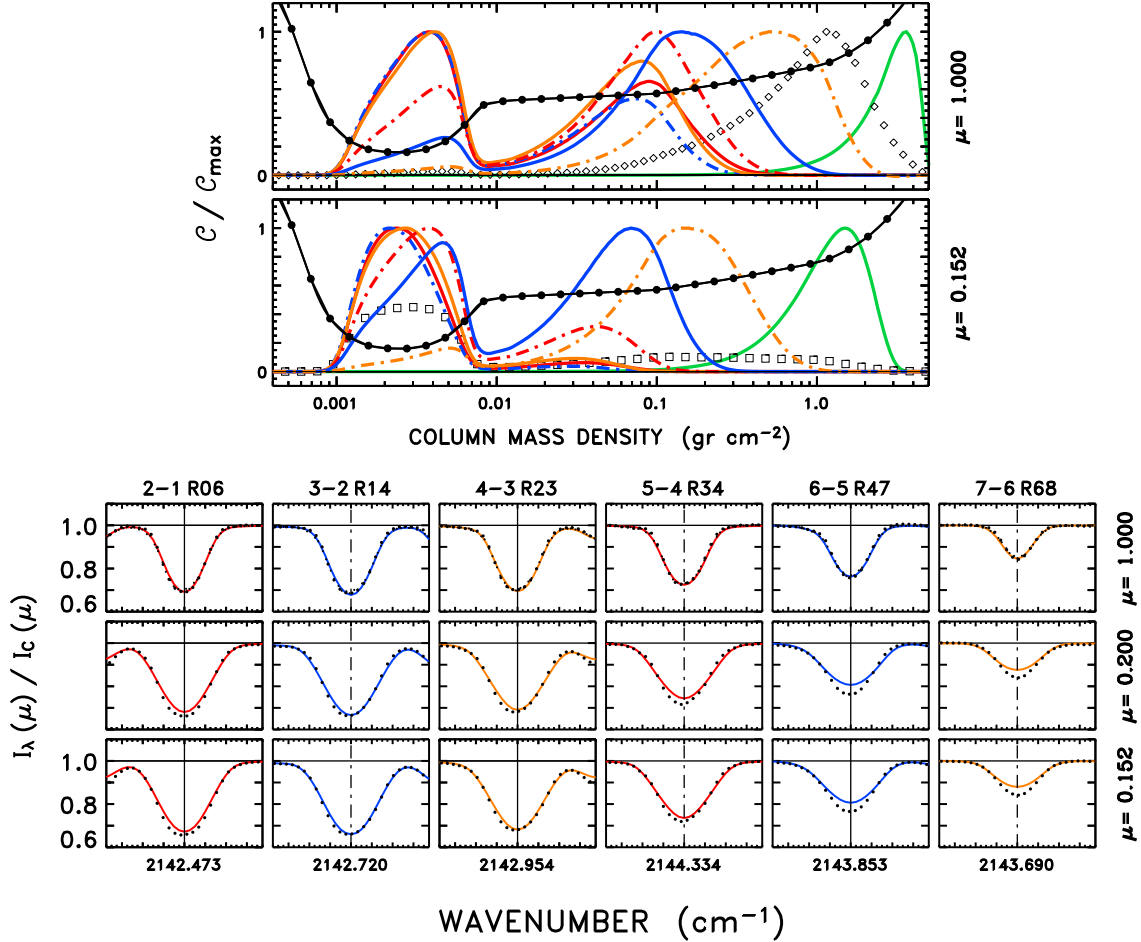


Fig. 11.— Center-limb behavior and contribution functions for representative CO  $\Delta v = 1$  lines synthesized with 1-D version of COmosphere model and derived  $\epsilon_O$ . Major ticks on relative wavenumber scales (abscissa) are  $0.020 \text{ cm}^{-1}$  ( $2.8 \text{ km s}^{-1}$ ). In upper two panels, normalized contribution functions are displayed for  $\mu = 1$  (upper) and  $\mu = 0.152$  (lower). Green curves furthest to right in each panel are intensity contribution functions for  $2145 \text{ cm}^{-1}$  ( $4.66 \mu\text{m}$ ) continuum, while curves to left are line depression contribution functions for CO transitions (note double peaks). CO curves are color coded, and solid or dot-dashed, to correspond with spectral panels (vertical line at  $\omega_0$  indicates linestyle). In uppermost panel, small diamonds depict relative concentration of CO:  $n_{\text{CO}}/(n_{\text{CO}})_{\text{max}}$ . In second panel, small squares depict fraction of oxygen bound in CO:  $n_{\text{CO}}/(\epsilon_O n_{\text{H}})$ . In  $T_{\text{min}}$  region, ratio is nearly 0.5 reflecting that virtually all available carbon (C/O = 0.5) has been captured into CO.

Fig. 12.— Oxygen abundances determined from single component versions of COmosphere and Asplund models (upper two, and middle two panels, respectively), and two sets of  $gf$ -values: Goorvitch (1994) and Hure & Roueff (1996). Panels to left are “cartoons” of particular models used in the simulations; FALC temperature distribution is provided (as a thin curve) in each panel for comparison. Long ticks at right and left sides of panel indicate the radial-tangential (blue and red, respectively) velocity model used in the simulation (usually  $[0.75, 2.00]$  km s $^{-1}$ ); horizontal line marks velocity zero (and  $T = 3500$  K level); major ordinate ticks are spaced 1 km s $^{-1}$  for  $\xi$  and 500 K for  $T(m)$ . Resulting  $\epsilon_O$ ’s for  $\Delta v = 1, 2$  samples are depicted in right hand panels as a function of lower state excitation energy. Lighter (red) dots generally to left are first overtone lines, while black dots generally to right are fundamental transitions. Hatched areas indicate means and  $\pm 1$  standard deviations for the two separate samples, while green line is linear least squares fit to the two samples combined (with mild filtering to eliminate outliers). Effect of correcting  $gf$ -values—according to apparent slope of  $\epsilon_O$ – $E_{\text{ex}}$  relation, taking true abundance from intercept of fit—is illustrated in lower two panels [“(gf)\*”] for the alternative oscillator-strength scales with optimum COmosphere model.

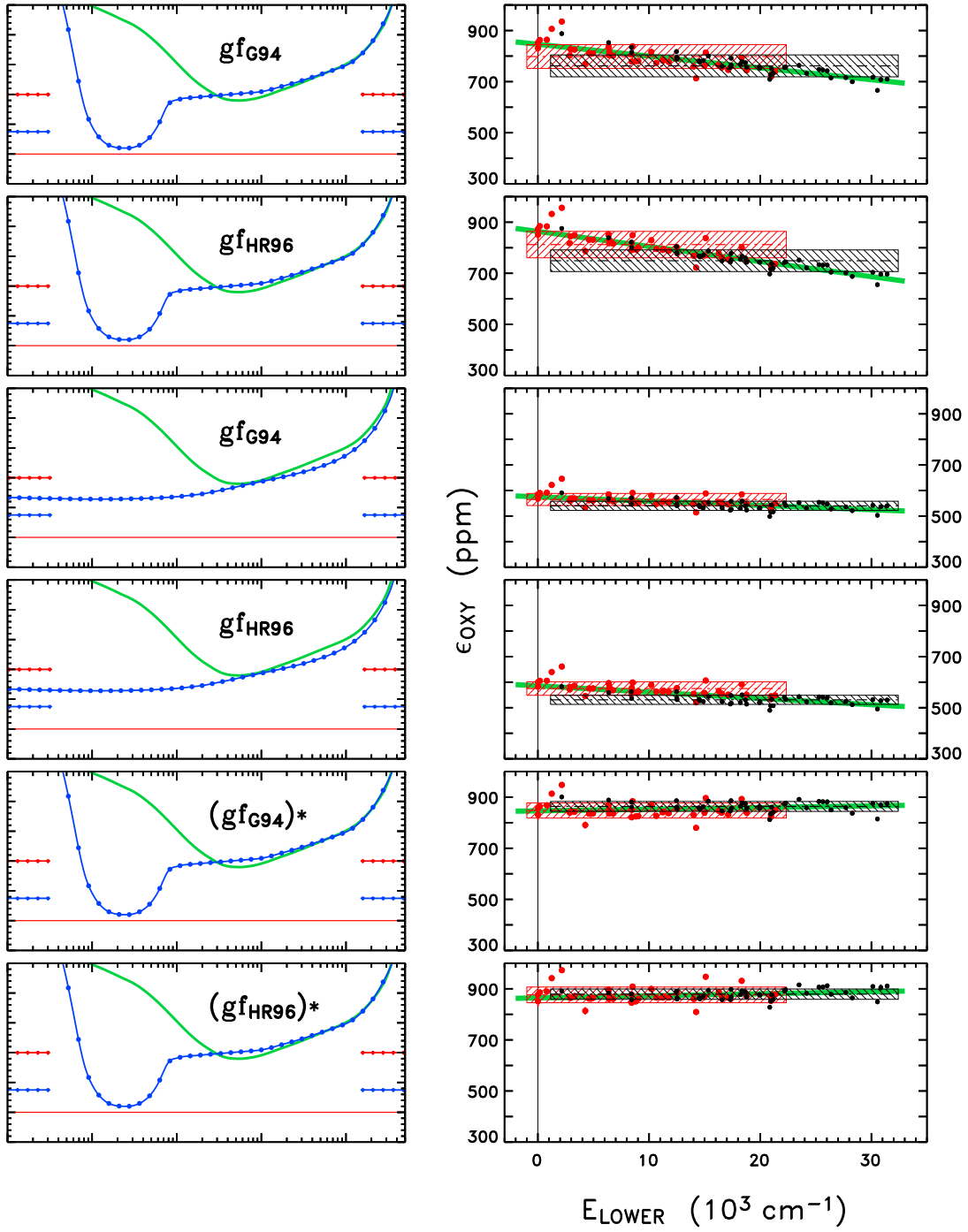


Fig. 12

Fig. 13.— Montage of  $^{12}\text{C}^{16}\text{O}$   $\Delta v = 1, 2$  rovibrational profiles, for representative members of abundance sample, and synthesized lineshapes for single component COmosphere model with best-fit  $\epsilon_{\text{O}} = 846$  ppm (and empirical corrections to  $gf$ -values). Like Fig. 3, major ticks on abscissa are  $0.02 \text{ cm}^{-1}$  apart, and relative intensity scales are graduated. First interval around unit level is first  $\pm 1\%$ , emphasizing continuum and (photometric) scatter around it. Full range extends to 20% below continuum level to show details of deeper features (although still weak in comparison to strongest  $\Delta v = 1$  absorptions of Fig. 3). Shallower lines (with central residual intensities  $\geq 85\%$ ) were locally normalized to continuum level according to bins (green points) on either side of line center, away from absorption depression itself. For stronger features, original “long range” continuum fit was retained. The 7–6 R68 transition connects to center-limb line set.

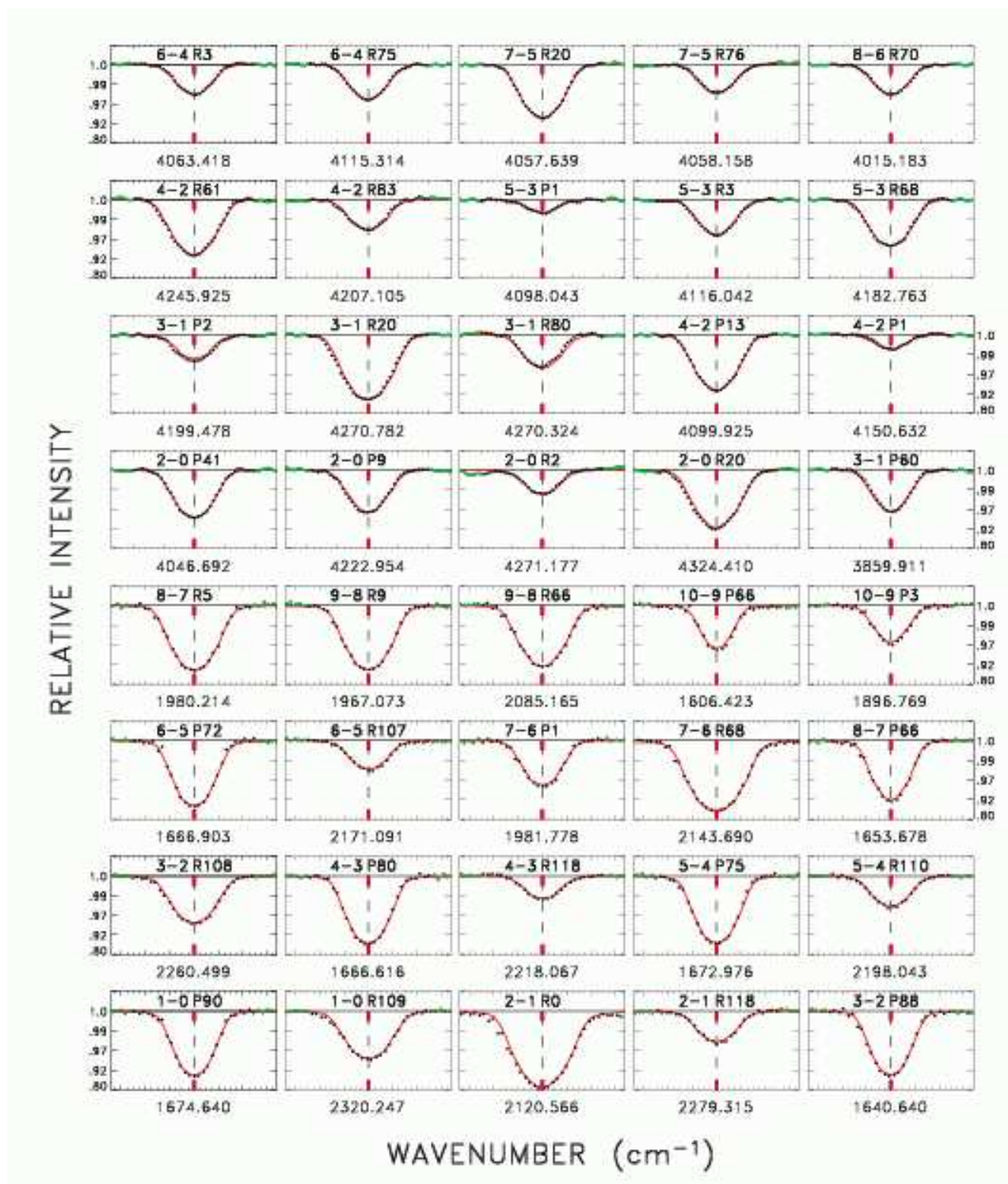


Fig. 13

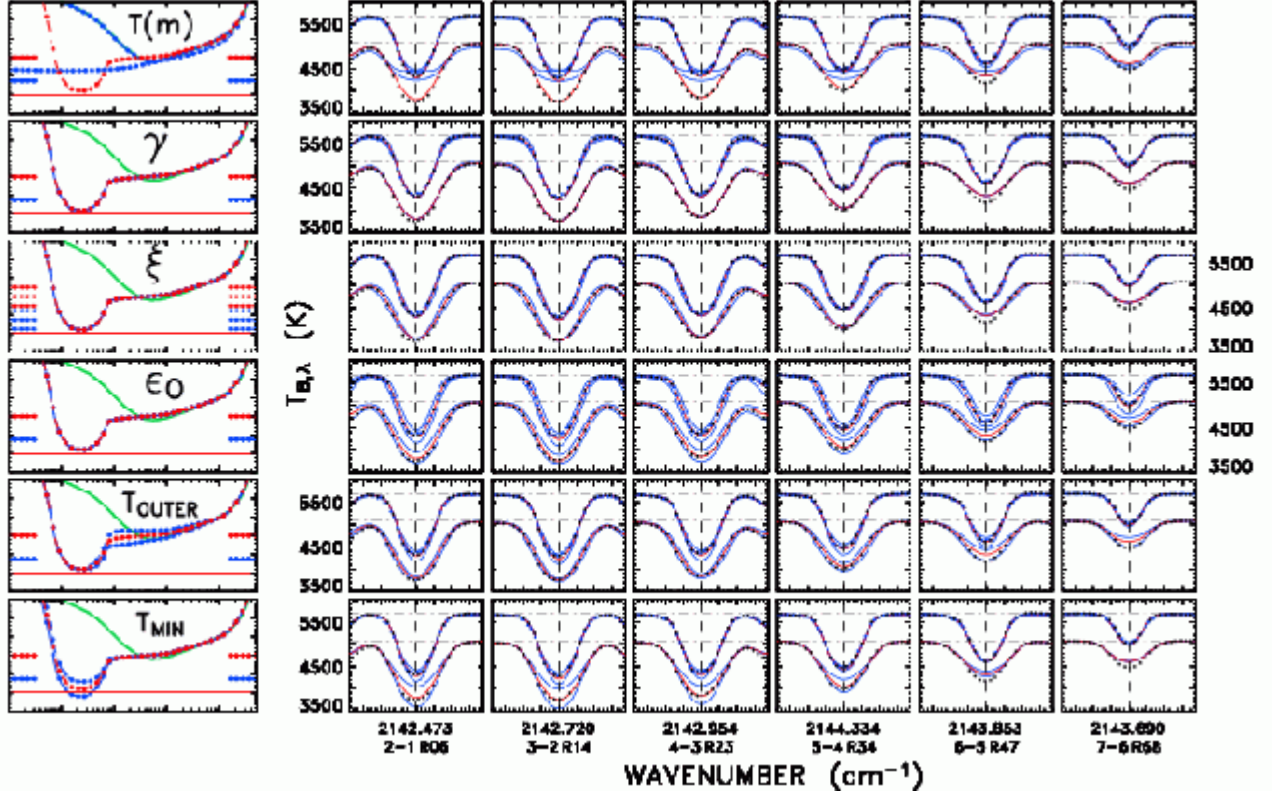


Fig. 14.— Sensitivity of representative  $\Delta v = 1$  transitions at  $\mu = 1$ , and their center-limb behavior, to changes in models and various key parameters (see text). As in Fig. 12, model temperature structures are illustrated schematically in left hand panels. Observations are same as in Fig. 11, although only disk center (upper, in each panel) and extreme limb ( $\mu = 0.152$ : lower) are shown here. Absolute continuum levels were set according to  $I_{C,\lambda}(\mu)$  calculated with optimum COmosphere model, and profiles now are displayed on brightness temperature scale. Major ticks on abscissa are  $0.02 \text{ cm}^{-1}$ . General decrease in core brightness temperature with increasing line strength (from right to left), and darkening of individual lines toward extreme limb, carry redundant information concerning the thermal profile of the outer photosphere.

Fig. 15.— (a) Oxygen abundances determined for representative single- and multicomponent models. As in Fig. 12, model temperature profiles are illustrated schematically in left hand panels, and resulting  $\epsilon_O$ 's for  $\Delta v = 1, 2$  samples in right hand panels as function of  $E_{\text{lower}}$ . In general, multicomponent versions of the base models have relatively little effect on derived oxygen abundance. Main influence is average mid-photospheric temperature where CO concentration peaks. Asplund mean model is cooler in this region than optimum COmosphere, and consequently predicts a lower oxygen abundance. Curiously, agreement between  $\Delta v = 1$  and 2 abundances is improved: this contrast is temperature sensitive in principle because one is comparing generally low excitation  $\Delta v = 2$  lines to mainly high excitation  $\Delta v = 1$  transitions, although one also must be wary of systematic errors in line absorption strengths which potentially could mimic a temperature effect, as seen in Fig. 8 for Hure & Roueff (1996)  $\Delta v = 2$   $gf$ -values. However, continuum center-limb test indicates Asplund model is too cool in middle photosphere. Dropping entire COmosphere temperature stratification systematically by 200 K (lowest panel) reproduces low O abundance ( $\sim 450$  ppm) obtained by Asplund et al. (2004), and removes excitation gradient between fundamental and first overtone samples, but low- $T$  model completely fails continuum center-limb test, like Asplund model itself.

(b) For additional model or parameter perturbations described in text. Here we see, for example, that changing  $T_{\text{min}}$  temperature or microturbulent velocity  $\xi$  has a negligible effect on  $\epsilon_O$ , whereas altering thermal profile of outer photosphere ( $T_{\text{OUTER}}$ ) or scaling total H<sup>−</sup> cross-section (b-f and f-f together) have more noticeable influences. However, none of the changes, for base COmosphere model, removes discrepancy between  $\Delta v = 1$  and  $\Delta v = 2$  abundances, although cooler  $T_{\text{OUTER}}$  profile is improvement in that direction. Nevertheless, that model performs more poorly in simulating run of  $\Delta v = 1$  core brightness temperatures with increasing line strength at  $\mu = 1$  (Fig. 14), although it does reproduce center-limb behavior of weaker 6–5 R47 and 7–6 R68 (which base model does less well).

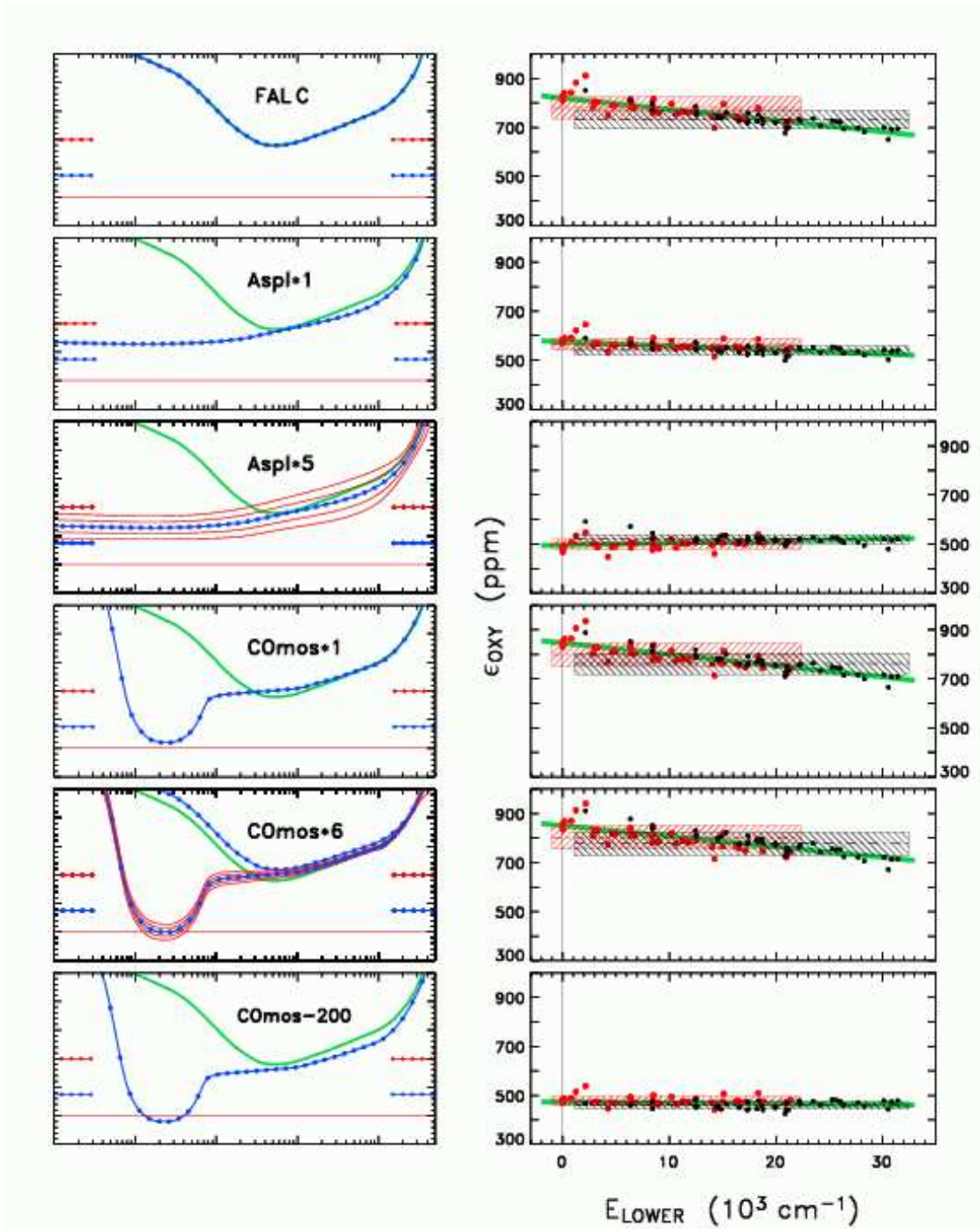


Fig. 15a

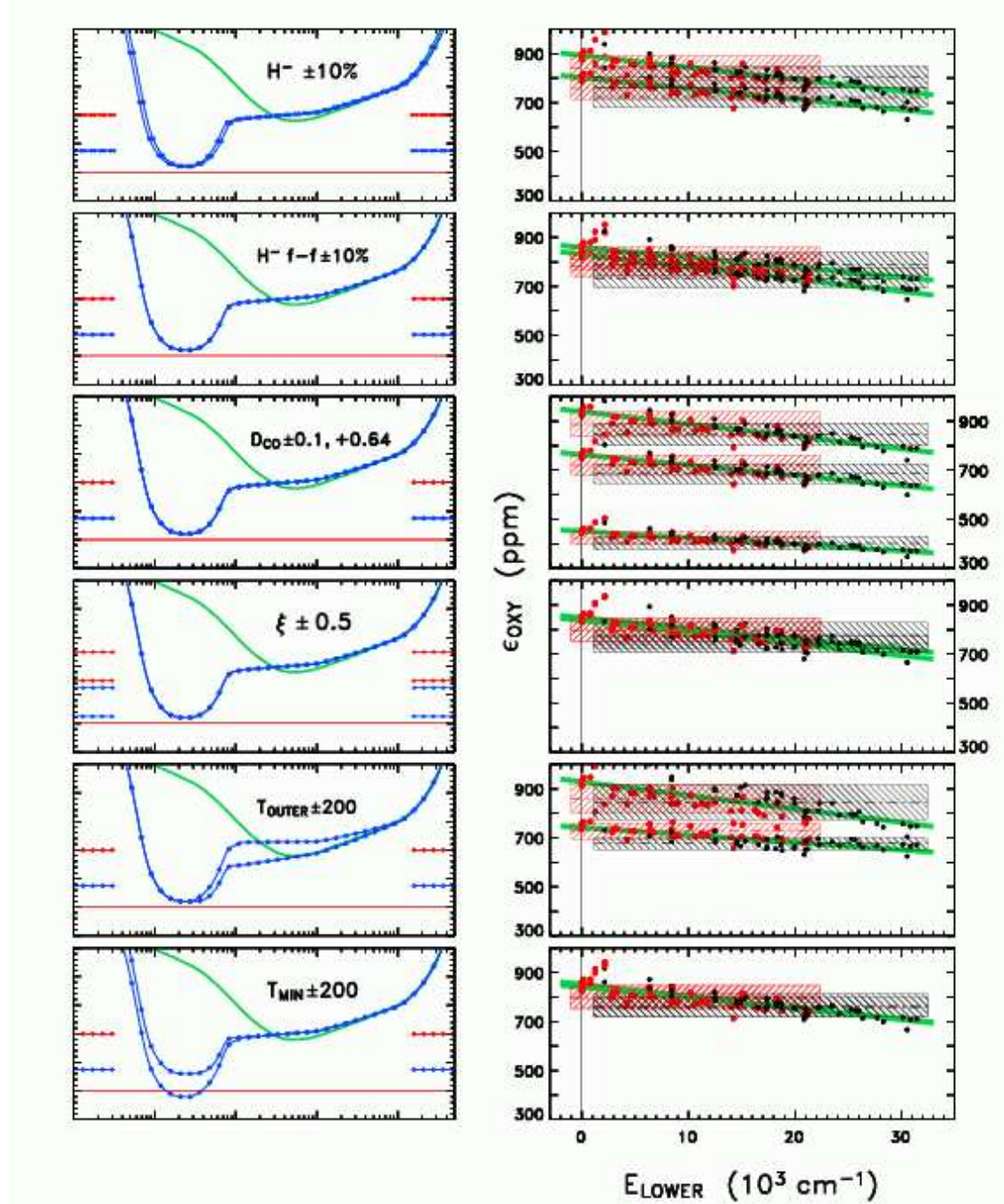


Fig. 15b

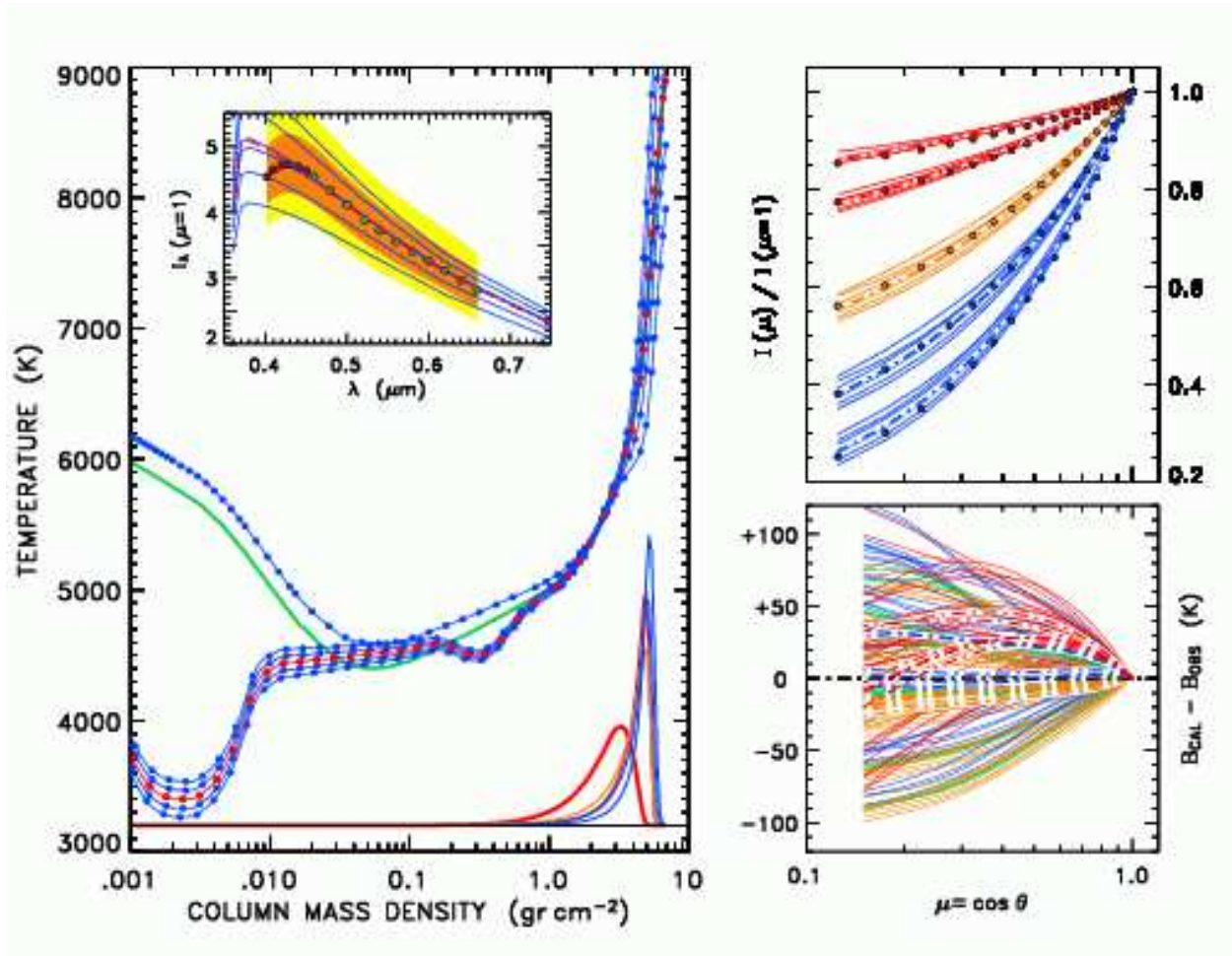


Fig. 16.— Continuum behavior for 6 component version of proposed Double Dip model: small temperature depression in middle photosphere improves thermal IR continuum center-limb behavior without degrading good match of base COmosphere model in visible and near IR.

Fig. 17.— (a) Abundances for single component and 6 component realizations of Double Dip model.  $\Delta v = 1$  abundance distributions for both versions of Double Dip is flatter with respect to  $E_{\text{lower}}$  than original COmosphere model, although now clear separation between  $\Delta v = 1$  and 2 systems is seen.

(b) Center-limb behavior for single component and 6 component realizations of Double Dip model.

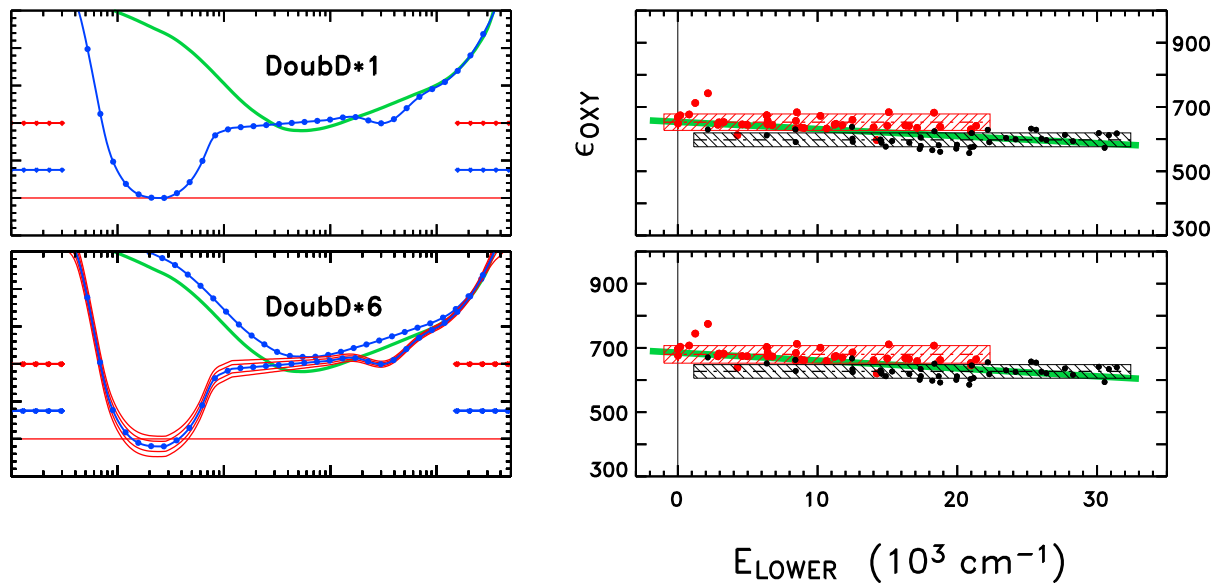


Fig. 17a

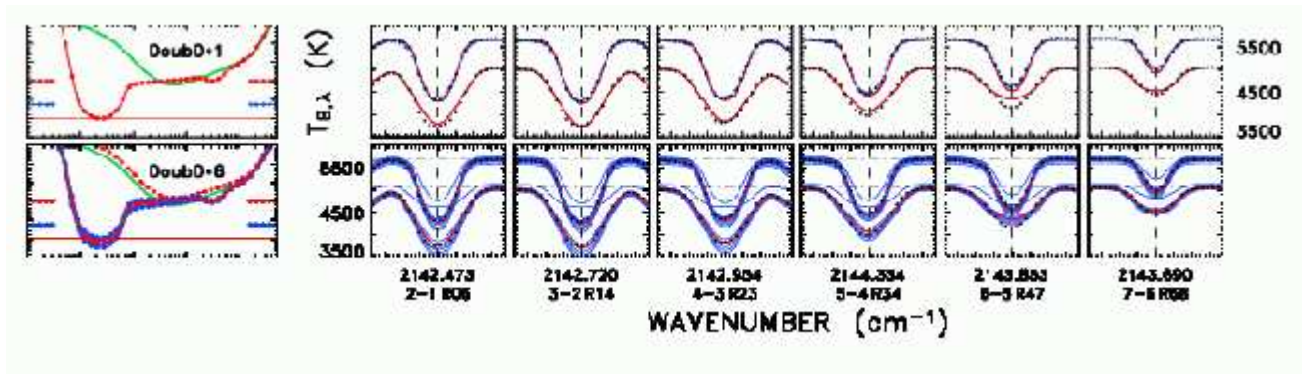


Fig. 17b

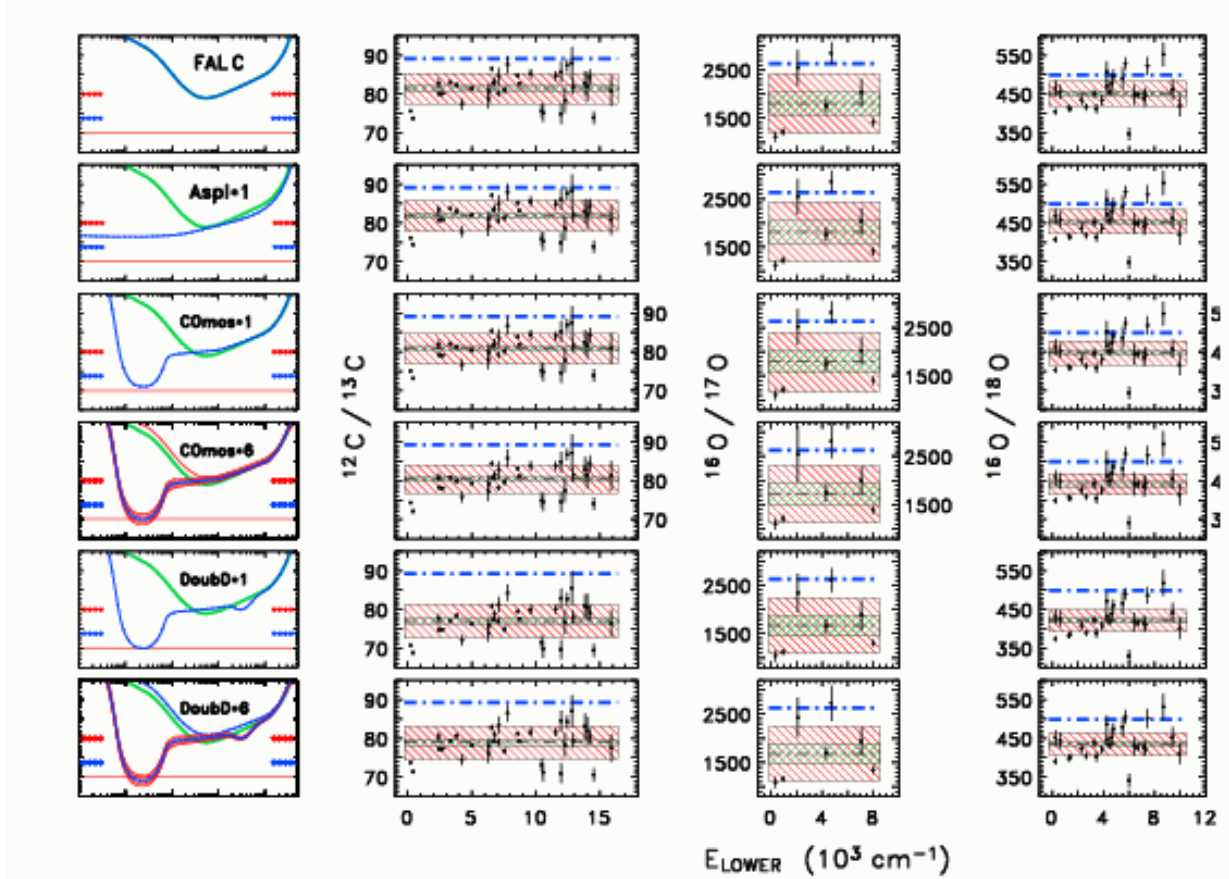


Fig. 18.— Isotopic abundance ratios for several atmospheric models. (Model dependent)  $gf$ -value corrections inferred from  $^{12}\text{C}^{16}\text{O}$  sample were applied to isotopomer oscillator strengths. Derived isotopic ratios are minimally dependent on thermal structure of model, and thus can be determined to better accuracy than absolute abundances. Outer (red) hatched bands indicate  $\pm 1$  standard deviation for each sample, after applying  $2\sigma$  filter to eliminate outliers; inner (green) hatched bands indicate  $\pm 1$  standard error of mean. Dot-dashed (blue) lines are terrestrial reference values.

Fig. 19.— Similar to Fig. 13, but now a montage of observed and synthesized lineshapes of representative  $^{13}\text{C}^{16}\text{O}$ ,  $^{12}\text{C}^{17}\text{O}$ , and  $^{12}\text{C}^{18}\text{O}$ ; based on single component COmosphere model, best-fit  $\epsilon_{\text{O}} = 846$  ppm (with  $\Delta = -5.5$  correction to  $gf$ -values), and  $^{12}\text{C}/^{13}\text{C} = 81$ ,  $^{16}\text{O}/^{17}\text{O} = 1751$ , and  $^{16}\text{O}/^{18}\text{O} = 438$ . Isotopomers are coded, in brackets following transition designations, e.g., “36” =  $^{13}\text{C}^{16}\text{O}$ . Again, relative intensity scales are graduated: this time, initial interval is  $\pm 0.3\%$  around unit level, and full range extends to only 6 % below it. Although the isotopic lines, in general, are very weak, high S/N of ATMOS spectra allows them to be detected at high level of confidence. (Note, also, three  $\Delta v = 2$   $^{13}\text{C}^{16}\text{O}$  transitions appended to  $\Delta v = 1$  sample.)

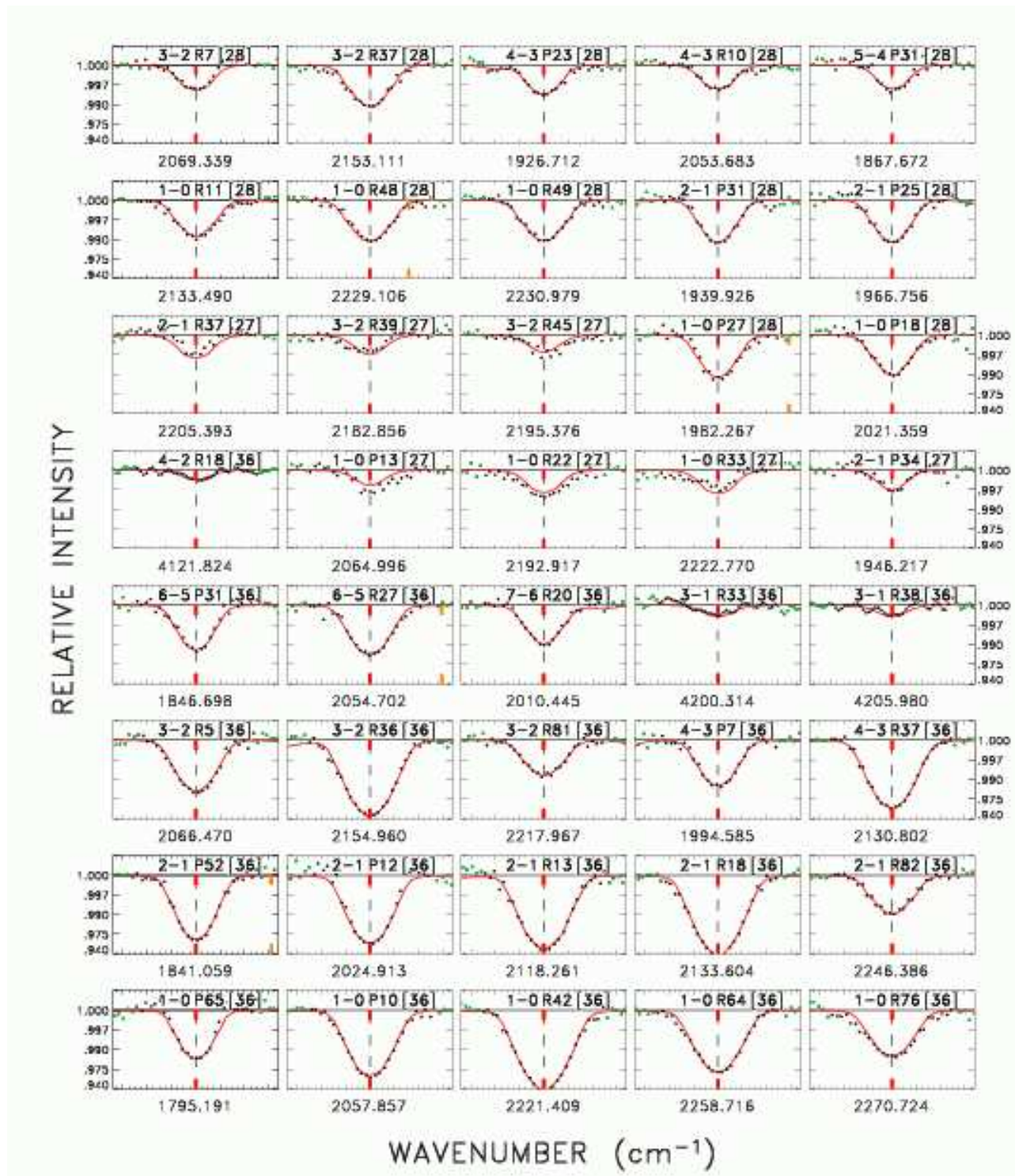


Fig. 19